Unraveling Material Behavior with Electron and X-ray Spectroscopies: From Transient Electronic Responses to Electronic Topological Transitions

Thesis by

Wonseok Lee

In Partial Fulfillment of the Requirements for

the degree of

Doctor of Philosophy in Chemistry

CALIFORNIA INSTITUTE OF TECHNOLOGY

Pasadena, California

2026

Defended May 19, 2026

Wonseok Lee
ORCID: 0000-0003-1077-0511

ACKNOWLEDGEMENTS

My Ph.D. journey would not be possible without the support, guidance, and encouragement of my mentors, lab members, collaborators, friends, and family. This section is dedicated to all those who have contributed to and accompanied me along this path.

First and foremost, I would like to express my sincere gratitude to my Ph.D. advisor, Professor Scott Cushing. Beginning my Ph.D. virtually posed unique challenges, and I feel fortunate to have joined your group during such a difficult time. I am especially grateful for your confidence in my potential and for entrusting me with multiple research projects. Under your mentorship, I have grown into a more independent and thoughtful scientist. I also appreciate your support for my well-being and your guidance as I navigate my next career path.

This work would also not have been possible without the support of Dr. Tom Gage. I am deeply thankful for the opportunity to access the resources at CNM and to collaborate on several projects and publications.

I would also like to thank my committee members, Professors Geoff Blake, Bill Goddard, and Lu Wei, for their insightful questions, thoughtful feedback, and guidance during my thesis progress meetings and examinations. Your input has been invaluable to my development and has strengthened this work.

I am also grateful to my past mentors for laying the foundation that prepared me for this journey. I thank Dr. Chul Hee Cho for giving me the freedom to explore my research interests during my high school thesis. I also thank Professors Sang Woo Han and Seunghoon Lee for the opportunity to contribute to the gold nanoparticle trimer project and for their mentorship. In addition, I would like to thank Professors Hyotcherl Ihee and Kiyoung Park for their advice throughout my undergraduate studies.

I would also like to thank my lab members for their support and for fostering a positive and stimulating research environment. This includes all the past and present members of the

Cushing Lab, whom I have not listed individually to avoid inadvertently overlooking anyone. I am especially grateful to Dr. Isabel Klein for being my initial mentor at the start of my Ph.D., when I began virtually in Korea, and for our work on the transition metal oxide project. I also thank Dr. Alex Krotz for laying the foundation of our computational code. I am very grateful to Professor Ye-Jin Kim for continuing to provide valuable feedback and for always being someone I could turn to for advice, even after leaving the group. To my cohort—Hamilton Evans and Drs. Nathan Harper, Emily Hwang, and Levi Palmer—thank you for your camaraderie and support throughout this journey. I am especially grateful to Levi, with whom I worked most closely; it was a pleasure working with you, and I truly appreciated your support in many ways. I wish you all the best on your next journey at Stanford. I also thank Natan Spear and Amy Lin for their encouragement and for motivating me to work harder. Although they are still new to the group, Claude Zheng and Kevin Alexander have already made tremendous contributions, and I leave the UEM lab in their capable hands with great confidence. Lastly, I thank Elisha Okawa for her essential administrative support.

I was also fortunate to participate in research projects outside the group, which broadened my scientific perspective. I especially thank Dr. Jasmine Hinton, Daniel Schacher, Professors Craig Schwartz, Keith Lawler, and Ashkan Salamat for the cadmium electronic topological transition project; Drs. Ettore Paltanin, Emiliano Principi, and Riccardo Mincigrucci for the thermite reaction project; and Dr. Alex Maznev for the cobalt self-diffraction project.

For me, pursuing a Ph.D. was not only a process of growing as an independent researcher, but also a journey of personal growth. I am deeply grateful to everyone who spent time with me outside the lab and shared meaningful moments both at Caltech and during my visits to Korea.

Lastly, I would like to thank my family, whose unwavering support and love made this journey possible. To my parents especially, thank you for standing by me through every decision and for always believing in me. I will continue striving to be a son you can be proud of.

ABSTRACT

Understanding how materials respond to external stimuli requires probes that can resolve coupled electronic, structural, and chemical changes across relevant length, time, and energy scales. This thesis investigates material dynamics and electronic structure using electron and X-ray spectroscopies, with a focus on how photoexcitation and high pressure modify the spectroscopic responses of solids.

The first part of this thesis focuses on ultrafast electron energy-loss spectroscopy as a probe of carrier, thermal, and structural dynamics. This approach is applied to crystalline silicon, where dense photoexcitation produces a transient reshaping of the bulk plasmon. The plasmon redshifts, broadens beyond the zero-loss peak response, and redistributes spectral weight, indicating that dense photoexcitation modifies the full dielectric response rather than simply introducing free carriers. These results show that the transient plasmon response arises from coupled changes in screening, electronic structure, and damping.

The second part investigates pressure-induced electronic topological transitions in cadmium using experimental and theoretical X-ray absorption spectroscopy. First-principles calculations reveal pressure-driven changes in the Fermi surface topology, while core–valence exciton projections connect these transitions to spectral changes at the Cd K edge. These results demonstrate that X-ray absorption spectroscopy can serve as a sensitive probe of electronic topological transitions.

The final part investigates resonant self-diffraction of femtosecond extreme ultraviolet pulses in cobalt near the Co $M_{2,3}$ edge. The observed self-diffraction signal is attributed to resonant changes in the complex refractive index, highlighting the potential of nonlinear extreme ultraviolet spectroscopy for probing ultrafast electronic dynamics at core-level resonances.

Together, these studies demonstrate that electron and X-ray spectroscopies provide powerful and complementary approaches for uncovering material behavior across multiple regimes, from nonequilibrium electronic dynamics to pressure-driven electronic topological transitions and nonlinear light–matter interactions.

PUBLISHED CONTENT AND CONTRIBUTIONS

1) Lee, W.; Palmer, L. D.; Gage, T. E.; Cushing, S. K. Nonequilibrium Reshaping of the Silicon Bulk Plasmon under Dense Photoexcitation. *In preparation*.

   L.W. helped conceive the project, conducted the experiments, led the data analysis, wrote the manuscript, and prepared the figures.

2) Lee, W.[†]; Palmer, L. D.[†]; Gage, T. E.; Cushing, S. K. Imaging Nanoscale Carrier, Thermal, and Structural Dynamics with Time-Resolved and Ultrafast Electron Energy-Loss Spectroscopy. *Chem. Phys. Rev.* **2025**, *6*, 041303. https://doi.org/10.1063/5.0289128.

   L.W. helped conceive the project and wrote a substantial portion of the manuscript.
   [†] indicates equal contributions.

3) Hinton, J. K.[†]; Schacher, D.[†]; Lee, W.[†]; Smith, G. A.[†]; Siska, E.; Park, C.; Ellison, P. B.; Cushing, S. K.; Schwartz, C. P.; Lawler, K. V.; Salamat, A. Electronic Topological Transitions in Cadmium under Pressure Studied via Theoretical and Experimental X-ray Absorption Spectroscopy. *Phys. Rev. B* **2024**, *110* (20), 205118. https://doi.org/10.1103/PhysRevB.110.205118.

   L.W. performed the exciton projection calculations and wrote the corresponding section of the manuscript.
   [†] indicates equal contributions.

4) Maznev, A. A.; Lee, W.; Cushing, S. K.; Angelis, D. D.; Fainozzi, D.; Foglia, L.; Gutt, C.; Jaouen, N.; Kammerbauer, F.; Masciovecchio, C.; Mincigrucci, R.; Nelson, K. A.; Paltanin, E.; Pelli-Cresi, J. S.; Polewczyk, V.; Ksenzov, D.; Bencivenga, F. Resonant Self-Diffraction of Femtosecond Extreme Ultraviolet Pulses in Cobalt. *In revision*, arXiv:2505.07168. https://doi.org/10.48550/arXiv.2505.07168.

   L.W. performed the self-diffraction calculations and wrote the corresponding section of the manuscript.

5) Kim, Y.-J.; Palmer, L. D.; Lee, W.; Heller, N. J.; Cushing, S. K. Using Electron Energy-Loss Spectroscopy to Measure Nanoscale Electronic and Vibrational Dynamics in a TEM. *J. Chem. Phys.* **2023**, *159* (5), 050901. https://doi.org/10.1063/5.0147356.

   L.W. wrote sections II and IV of the manuscript.

6) Paltanin, E.[†]; Pelli Cresi, J. S. [†]; Principi, E.; Lee, W.; Bencivenga, F.; De Angelis, D.; Foglia, L.; Garzella, D.; Kurdi, G.; Manfredda, M.; Naumenko, D.; Simoncig, A.; Cushing, S. K.; Mincigrucci, R.; Masciovecchio, C. Time-Resolved Chemically-Selective Spectroscopic Investigation of the Redox Reaction between Hematite and Aluminium. *Nat. Commun.* **2025**, *16* (1), 7282. https://doi.org/10.1038/s41467-025-62436-z.

L.W. performed the computations and wrote the corresponding section of the manuscript.

† indicates equal contributions.

TABLE OF CONTENTS

LIST OF FIGURES

LIST OF TABLES

C h a p t e r 1

INTRODUCTION

Adapted with permission from the following:

Kim, Y.-J.; Palmer, L. D.; Lee, W.; Heller, N. J.; Cushing, S. K. Using Electron Energy-Loss Spectroscopy to Measure Nanoscale Electronic and Vibrational Dynamics in a TEM. *J. Chem. Phys.* **2023**, *159* (5), 050901. https://doi.org/10.1063/5.0147356.

Lee, W. †; Palmer, L. D. †; Gage, T. E.; Cushing, S. K. Imaging Nanoscale Carrier, Thermal, and Structural Dynamics with Time-Resolved and Ultrafast Electron Energy-Loss Spectroscopy. *Chem. Phys. Rev.* **2025**, *6* (4), 041303. https://doi.org/10.1063/5.0289128.

† indicates equal contributions. Copyright © 2025, AIP Publishing.

1.1 Electron Energy-Loss Spectroscopy in an Ultrafast Electron Microscope

Studying ultrafast and time-resolved dynamics is crucial for understanding complex transient processes in a material. These studies are particularly significant at the nanoscale, where a material's behavior can be drastically different under non-equilibrium conditions. On timescales ranging from femtoseconds to milliseconds, the interactions and energy transfer between electrons, holes, and phonons in a material determine its electronic, optical, and structural properties. These processes are fundamental to the operation of energy conversion and optoelectronic devices. For example, understanding the excitation, thermalization, transport, and recombination dynamics of charge carriers can lead to the design of solar cells with improved photovoltaic efficiencies,[1–4] while monitoring the trajectories of hot electrons in plasmonic materials can guide effective photocatalytic platforms.[5–8] In addition, nanoscale systems often exhibit size- and shape-dependent properties,[9–11] and photoexcited dynamics

at interfaces, grain boundaries, and defects deviate significantly from their bulk counterparts.[12,13] This highlights the need for imaging techniques with nanometer spatial and femtosecond temporal resolutions.

The spatial resolution limit of imaging techniques is determined by the Abbe diffraction limit, given by $d = \lambda/2\mathrm{NA}$ where λ is the wavelength and NA is the numerical aperture.[14] Since electrons can have shorter wavelengths than photons, transmission electron microscopy (TEM) provides superior spatial resolution compared to optical microscopy. For example, an electron with an energy of 10 keV and a NA of 1.0 has an Abbe limit of 6.1 pm—shorter than the smallest atomic radius (37 pm). Technical advances in aberration-corrected electron optics,[15–18] scanning TEM (STEM),[19,20] and direct electron detectors[21–24] have enabled picometer-scale imaging with resolution limited primarily by inherent atomic vibrations.

For decades, TEM has proven to be a powerful and robust imaging tool; however, its temporal resolution was limited by the detection rate of charge-coupled device (CCD) cameras with scintillators, making it unsuitable for imaging dynamics that occur on timescales faster than milliseconds. To overcome this limitation, ultrafast electron microscopy (UEM) integrates a pump–probe technique within the TEM, enabling spatially resolved measurements at ultrafast timescales.[25–30] **Figure 1.1(a)** shows a standard UEM setup, where a femtosecond (fs) pump pulse photoexcites the specimen, while a photoelectron probe is generated from the photocathode via the photoelectric effect using a femtosecond ultraviolet (UV) pulse. The time delay between the pump and probe pulses can be controlled using a mechanical delay stage to measure a material's photoexcited response. The generated electron pulses are then shaped and focused using condenser lenses. After passing through the specimen, the image is magnified and projected onto the detector through post-specimen lenses. In STEM, scan coils deflect the electron beam to raster across the specimen with a focused probe, providing more localized data compared to conventional TEM. A q-slit selects specific momentum directions for momentum-resolved measurements.

Real-space imaging in a UEM can be correlated with reciprocal and energy spaces via diffraction and spectroscopy, respectively.

This chapter focuses on using electron energy-loss spectroscopy (EELS) to image charge carrier, thermal, and structural dynamics at the nanoscale. Time-resolved and ultrafast EELS in a UEM can probe localized photoexcited dynamics, including charge and thermal transport within a specimen, by utilizing a wide energy range.[30] As the name suggests, EELS measures the energy distribution of incident electrons that have interacted with the specimen as a function of energy loss.[31,32] For a specimen with a thickness less than the electron's inelastic mean free path, most electrons are elastically scattered, which results in negligible energy loss. This is represented by the most intense peak at 0 eV energy loss, known as the zero-loss peak (ZLP), in the EEL spectrum. In contrast, inelastic scattering involves the loss of energy by the incident electrons. The low-loss region, extending from 0 to 50 eV, corresponds to quasiparticle excitations such as phonons, magnons, excitons, and surface and bulk plasmons, as well as excitations of valence electrons to unoccupied states (inter/intraband transitions). This region provides access to a range of a material's properties, such as atomic and lattice vibrations,[33,34] band gap,[35] specimen thickness,[36] dielectric function,[37] valence electron density,[38] surface or interface states,[39] and joint density of states (DOS).[40] The core-loss region, generally above 50 eV, corresponds to the excitation of electrons from atomic core levels, adding element specificity to the technique. This enables the measurement of elemental distributions,[41] local coordination geometry,[42] element-specific unoccupied DOS,[43] and radial distribution function.[44] Time-resolved and ultrafast EELS can therefore theoretically measure all these inelastic excitations along femtosecond to microsecond timescales.

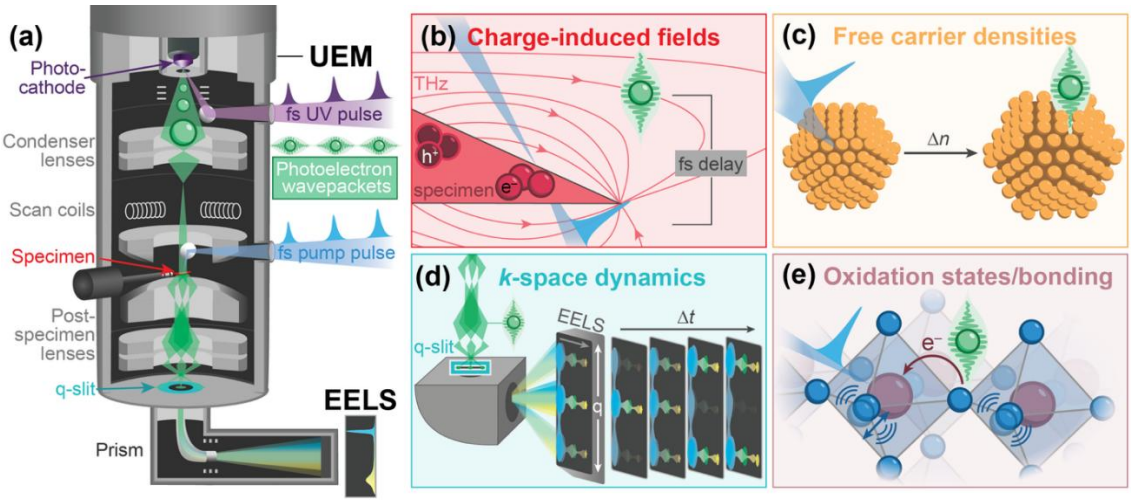

Figure 1.1. Time-resolved and ultrafast electron energy-loss spectroscopy (EELS) in the ultrafast electron microscope (UEM). (a) A standard UEM uses an ultraviolet (UV) pulse-triggered photocathode to generate ultrafast photoelectron wavepackets (green). Scan coils deflect the electron beam in scanning TEM (STEM). A femtosecond (fs) pump (blue) photoexcites the specimen (red) at fixed time delays relative to the photoelectron probe. A q-slit (teal) enables momentum-resolved EELS. Apertures are excluded for clarity. **(b–e)** Time-resolved and ultrafast EELS imaging methods. **(b)** Charge dynamics electron microscopy (CDEM) maps charge-induced terahertz (THz) fields around a specimen. **(c)** Ultrafast low-loss EELS quantifies a material's free carrier density change due to thermal expansion or strain. **(d)** Time- and momentum-resolved EELS measures carrier dynamics in reciprocal space with a q-slit. **(e)** Ultrafast core-loss EELS probes photoinduced changes in oxidation state and bonding due to charge transfer and phonons.

1.2 Background

Photoexcitation alters the spectral features of the EEL spectrum by both local electromagnetic fields and changes in electron or phonon populations (**Figs. 1.1(b)–1.1(e)**). For example, a local electromagnetic field modifies characteristics of the electron probe, enabling ultrafast imaging of charge dynamics at nanometer spatial and femtosecond temporal resolutions (**Fig. 1.1(b)**). Photoexcitation also influences the energy, intensity, and

linewidth of the bulk plasmon and core-loss peaks, which allows spatially and temporally resolved EELS measurements across the full accessible energy range. These changes to spectral features, called differential spectra, are central to time-resolved and ultrafast EELS techniques. Therefore, understanding the origin of these ground-state peaks and how photoexcitation induces differential features is essential for analyzing dynamics in such studies.

Low-Loss EELS

The bulk plasmon is a collective longitudinal oscillation of loosely bound electrons. In metals, it corresponds to the collective excitation of the free-electron gas, while in semiconductors and insulators, it involves the collective oscillation of valence electrons.[45] In EELS, the bulk plasmon excitation typically occurs between 5 and 30 eV and the peak is in the low-loss region of the spectrum, which is dependent on the free or valence carrier density of materials. Since plasmon scattering has the highest scattering cross-section, the plasmon loss feature appears as the most prominent feature after the ZLP.

According to the Drude model,[46–48] the energy-loss function for a bulk plasmon is given by:

$$\mathrm{Im}\left[-\frac{1}{\epsilon(\omega)}\right] = \frac{\omega_p^2 \omega \Gamma}{\left(\omega^2 - \omega_p^2\right)^2 + \omega^2 \Gamma^2} \tag{1.1}$$

where $\omega_p = \sqrt{ne^2/m_e\epsilon_0}$ is the bulk plasmon frequency. Here, n is the valence or free electron density, e is the elementary charge of an electron, m_e is the effective electron mass, and ϵ_0 is the vacuum permittivity. The parameter Γ is the inverse of relaxation time and depends on both electronic and lattice temperatures. The energy-loss function of a perfect conductor has a frequency peaking at ω_p, full-width at half maximum (FWHM) of Γ, and peak height of ω_p/Γ. Therefore, the bulk plasmon provides information about the dielectric function, carrier density, and electron scattering time.

Importantly, the bulk plasmon energy is sensitive to the electron density $n = N/V$, where N is the number of electrons and V is the lattice volume. In photoexcited semiconductors and

insulators, the valence electron density is modified by 1) the promotion of electrons from the valence band to the conduction band and 2) thermal expansion or contraction of the lattice. As a result, ultrafast low-loss EELS can measure changes to a material's carrier density due to photoexcitation while capturing both the electronic and structural effects (**Fig. 1.1(c)**).

The bulk plasmon energy is affected not only by the carrier density but also exhibits dependence on momentum transfer. At small momentum transfer q, the dispersion relation of the bulk plasmon is approximately given by:

$$E_p \approx E_{p,0} + \left(\frac{\hbar^2}{m}\right)\alpha q^2 \tag{1.2}$$

where $E_{p,0}$ is the plasmon energy at $q = 0$, $\hbar = \frac{h}{2\pi}$ is the reduced Planck constant, and $\alpha = \frac{3}{5}\frac{E_F}{\hbar\omega_p}$ is the dispersion coefficient with E_F being the Fermi energy.[48] This relation indicates that the bulk plasmon energy increases quadratically with momentum transfer. It is also noted that electrons can carry a wide range of momentum transfer, unlike photons. This difference enables the extraction of detailed insights into photoexcitation, scattering, and relaxation processes in reciprocal space using momentum-resolved EELS (**Fig. 1.1(d)**).

Core-Loss EELS

In addition to bulk plasmon excitation, electrons can be excited from core levels to unoccupied states of a material, leading to peaks or "edges" in the core-loss region. The energy of the ionization edge is determined by the binding energy of the atomic subshell, making this spectral feature element specific. According to Fermi's golden rule, the transition rate $W_{i\to f}$ for a system transitioning from an initial state Ψ_i to a final state Ψ_f upon interaction with an incident electron of energy $\hbar\omega$ is given by:[49]

$$W_{i\to f} = \frac{2\pi}{\hbar}\left|\langle\Psi_f|\hat{T}|\Psi_i\rangle\right|^2 \delta(E_f - E_i - \hbar\omega). \tag{1.3}$$

Here, $\hat{T}$ is the transition operator for inelastic scattering, expressed as $\hat{T} = e^{\mathrm{i}\mathbf{q}\cdot\mathbf{r}}$. The delta function accounts for energy conservation, indicating that the transition occurs when the energy of the final state matches the energy of the initial state plus the energy loss of probe electrons. The transition operator can be expressed as a Taylor series:

$$\hat{T} = e^{\mathrm{i}\mathbf{q}\cdot\mathbf{r}} = 1 + \mathrm{i}\mathbf{q}\cdot\mathbf{r} - \frac{1}{2}(\mathbf{q}\cdot\mathbf{r})^2 + \cdots. \tag{1.4}$$

For small momentum transfer, higher-order terms can be neglected. Under the dipole approximation and assuming the initial core-level and final state wavefunctions are atomic-like, Eq. (1.3) can be simplified as:

$$W_{i\to f} = \frac{2\pi}{\hbar}\left|\langle\Psi_f|\mathbf{q}\cdot\mathbf{r}|\Psi_i\rangle\right|^2 \delta(E_f - E_i - \hbar\omega). \tag{1.5}$$

The wavefunction overlap integral in Eq. (1.5) will only be nonzero if the symmetry of the wavefunction changes during the transition. This leads to the dipole selection rule $\Delta l = \pm 1$, where Δl is the change in angular momentum quantum number during the transition. For instance, a K edge probes unoccupied states with *p*-character, while $L_{2,3}$ edges probe unoccupied *s*- and *d*-like states. However, if the momentum transfer is sufficiently large to consider the higher-order terms, EELS can detect dipole-forbidden transitions.[50,51]

An understanding of core-level electronic transitions is crucial for interpreting core-loss EELS, as they provide insight into the chemical bonding, local structure, and coordination geometry of materials. In solids, the unoccupied electronic states can be modified by chemical bonding and oxidation states, which appear in the first 30–40 eV above the edge threshold. This region, known as the electron energy-loss near edge structure (ELNES), reveals details about the local chemical structure and bonding.[52] At energy loss beyond the ELNES region, oscillations in the extended energy-loss fine structure (EXELFS) are used to determine interatomic distances and coordination numbers.[53] Ultrafast core-loss EELS measurements can, therefore, probe changes in the chemical bonding and coordination

geometry of a material caused by photoexcitation, such as charge transfer and lattice changes (**Fig. 1.1(e)**).

However, ultrafast core-loss EELS presents several challenges. The energy-differential cross-section for inelastic scattering with energy loss E, denoted as $d\sigma/dE$, follows an inverse power-law relationship:[54]

$$\frac{d\sigma}{dE} \propto E^{-r} \tag{1.6}$$

where r is a real and positive constant. This relationship implies that signal intensity decreases rapidly with increasing energy loss, making it significantly more difficult to detect and analyze ionization edges in the core-loss region compared to spectral features in the low-loss region. Moreover, plasmon scattering can complicate core-loss signals, particularly when multiple scattering becomes significant. This can increase the background intensity and distort the shape and energy of the core-loss spectrum. Additionally, core-loss peaks from shallower core levels, such as the $M_{2,3}$ edges, may overlap with the low-loss region, complicating peak assignment.

1.3 Ultrafast EELS Techniques

Charge Dynamics Electron Microscopy

Charge dynamics electron microscopy (CDEM) exploits the interaction between an electron probe and terahertz (THz) near-fields with picosecond lifetimes. These THz fields are generated by moving charges within and around a specimen, where carriers around a specimen originate from a photoemitted electron plasma. As such, CDEM enables nanoscale imaging of charge generation, separation, and transport with femtosecond to picosecond time resolution.

Figure 1.2(a) illustrates how CDEM maps the motion of a photoemitted electron plasma evolving from a Cu rod by measuring how the plasma energetically impacts the electron probe.[55] The measurements reveal that the electron beam undergoes both acceleration and deceleration during its passage through or near the plasma's evolving electron cloud. Initially,

acceleration dominates due to the motion of the emitted electrons along transverse directions to the electron beam. The electron beam not only gains energy but also shows spectral broadening, which is strongest within 100 femtoseconds after laser excitation. As the plasma evolves, beginning to expand and reabsorb to the Cu surface, the electron probe decelerates. Through experimental data and physics-based numerical simulations, four distinct stages in the plasma's evolution are identified: laser irradiation, photoemission and THz field generation, plasma expansion, and surface reabsorption.

Beyond metallic specimens, CDEM also enables imaging of carrier dynamics in semiconductors.[56] The interaction is mediated by the THz field arising from the photo-Dember effect, which is where asymmetric electron–hole diffusion leads to dipolar field generation. By adjusting the electron beam position and time delay, the THz near-field is retrieved from the measured electron energy shifts. This approach not only spatially resolves the near-field but also enables the reconstruction of charge distributions. The differences in mobility between electrons and holes manifest as distinct spatiotemporal behaviors, as revealed by reconstructed charge density maps in InAs (**Fig. 1.2(b)**). Simulations using a hydrodynamic model of the photo-Dember effect predict transient currents and corresponding energy shifts of the probe electrons, showing strong agreement with the experimental results (**Fig. 1.2(c)**).

CDEM offers a powerful platform for exploring carrier dynamics in semiconductors, nanostructures, and optoelectronic devices. Its unique ability to capture transient THz fields associated with charge carrier motion provides critical insights for optimizing the performance of electronic components. By directly linking nanoscale material structure to functional electronic behavior, CDEM significantly advances our understanding of ultrafast charge carrier dynamics.

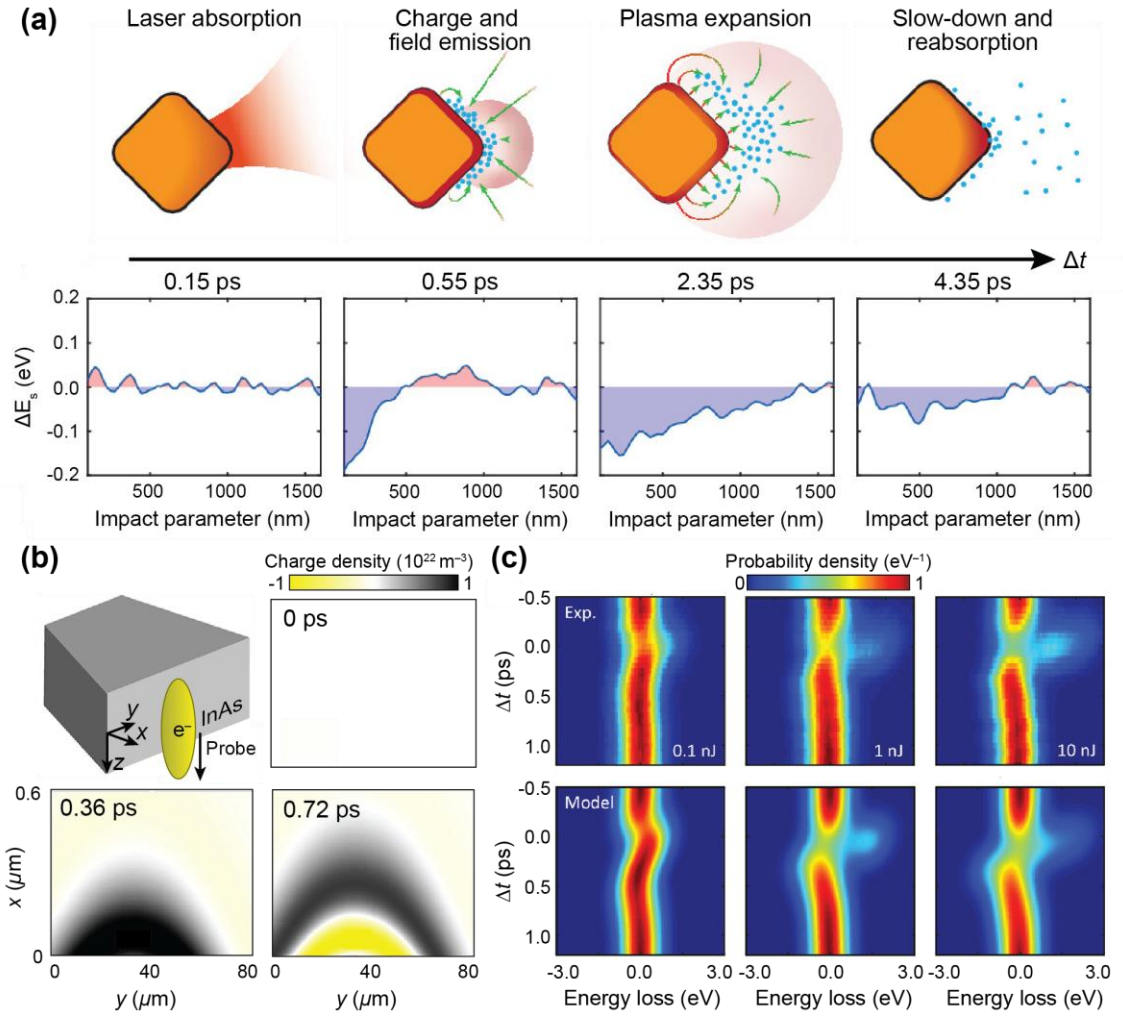

Figure 1.2. Charge dynamics electron microscopy (CDEM). (a) Evolution of the photoemitted electron cloud's plasma around a Cu rod (top) and the corresponding change in the ultrafast electron probe energy due to THz fields at fixed distances from the Cu rod (bottom). Adapted with permission from Ref. 55. **(b)** Spatiotemporal evolution of the charge distribution in an InAs crystal. **(c)** Experimental (top) and simulated (bottom) ultrafast EEL spectra, measured near the InAs surface using CDEM, for varying pump pulse energies. Adapted with permission from Ref. 56.

Ultrafast Low-Loss EELS

As discussed in **Chapter 1.2**, low-loss inelastic scattering probes inter/intraband transitions, as well as the excitation of quasiparticles such as phonons and plasmons. To date, ultrafast EELS has primarily studied surface plasmons and optical near fields because they lead to stronger signals than most low- and core-loss excitations. For example, the coupling of the incident photons to induced local charge density appears as quantized equidistant side peaks around the ZLP, usually referred to as photon-induced near-field microscopy (PINEM).[57–62] PINEM provides a time-resolved picture of the local electromagnetic field, and has led to various applications measuring electron–photon entanglement,[63,64] quantum optics and photonics, and attosecond electron pulse generation.[65] However, this section specifically highlights photoexcited plasmon dynamics and their interplay with a material's electronic and structural properties.

Ultrafast low-loss EELS was first employed to map the chemical bonding dynamics in graphite, revealing how these dynamics modify the spectral features of the π, surface, and bulk σ + π plasmon excitations.[66,67] Graphite serves as an ideal model system for investigating the interplay between structural and electronic changes induced by laser irradiation. As a result, graphite has been extensively studied using other ultrafast and time-resolved EELS techniques, further discussed later. Experimental results show that graphite's bulk plasmon energy initially blueshifts, followed by a redshift at longer time delays (**Fig. 1.3(a)**). This behavior corresponds to interlayer contraction and subsequent expansion, as confirmed by ultrafast electron diffraction (UED) and density functional theory (DFT)-based charge-density calculations. These structural changes were correlated with phase transitions from 2D (sp^2, graphene-like) to 3D (sp^3, diamond-like) electronic structures, highlighting the potential of ultrafast low-loss EELS for probing complex phenomena. The photoinduced structural dynamics and resulting plasmonic response were further validated through *ab initio* DFT calculations.[68]

Ultrafast low-loss EELS was also employed to investigate plasmonic nanomaterials such as gold nanotriangles (AuNTs), enabling direct detection of both localized surface plasmons

(LSPs) and bulk plasmons, which is difficult to achieve with purely optical methods.[69] The time-dependent evolution of the bulk plasmon and LSP peak energies in AuNTs (**Fig. 1.3(b)**) reveals opposite changes in the photoexcited electron density in the AuNTs' bulk and surface regions. This underscores the ability of ultrafast low-loss EELS to measure spatially dependent photoinduced effects in nanoparticles. Additionally, the relaxation times associated with electron–phonon and phonon–phonon interactions extracted from the EELS measurements were consistent with those observed in optical studies, further validating the technique's accuracy in probing ultrafast processes in nanoparticles. Analysis using a two-temperature model estimated the relaxation of electronic and lattice temperatures following laser irradiation, and these predictions were confirmed by the energy shifts and broadening of the plasmon peaks.

Ultrafast low-loss EELS has also been applied to other nanoscale systems such as carbon nanotubes (CNTs), gaining insight into their unique low-dimensional properties. Vanacore *et al*. combined UED and ultrafast low-loss EELS to monitor lattice and charge distribution changes in CNTs under laser excitation.[70] UED data indicated that axial (along the tube axis) CNT deformation is dominated by electron-driven processes, as evidenced by a faster initial expansion, while radial deformation is slower and phonon-driven. The charge distribution dynamics were further examined in single-walled CNTs (SWCNTs) using ultrafast low-loss EELS. A redshift of the bulk plasmon (**Fig. 1.3(c)**) indicates a decreasing in-plane electron density, as predicted by the free-electron model. This suggests that lattice expansion occurs along the nanotube's axis, driven by occupation of antibonding π^* state and a resulting decrease in intrawall electron density. *Ab initio* DFT calculations further reinforce this interpretation, showing significant axial C–C bond expansion upon electronic excitation. A separate study by Zheng *et al*. similarly investigated the ultrafast dynamics in SWCNTs (**Fig. 1.3(d)**).[71] In addition to UED and ultrafast low-loss EELS, optical transient absorption spectroscopy was also utilized to demonstrate how the redshift of the in-plane plasmons influences the ultrafast photoresponse of SWCNTs.

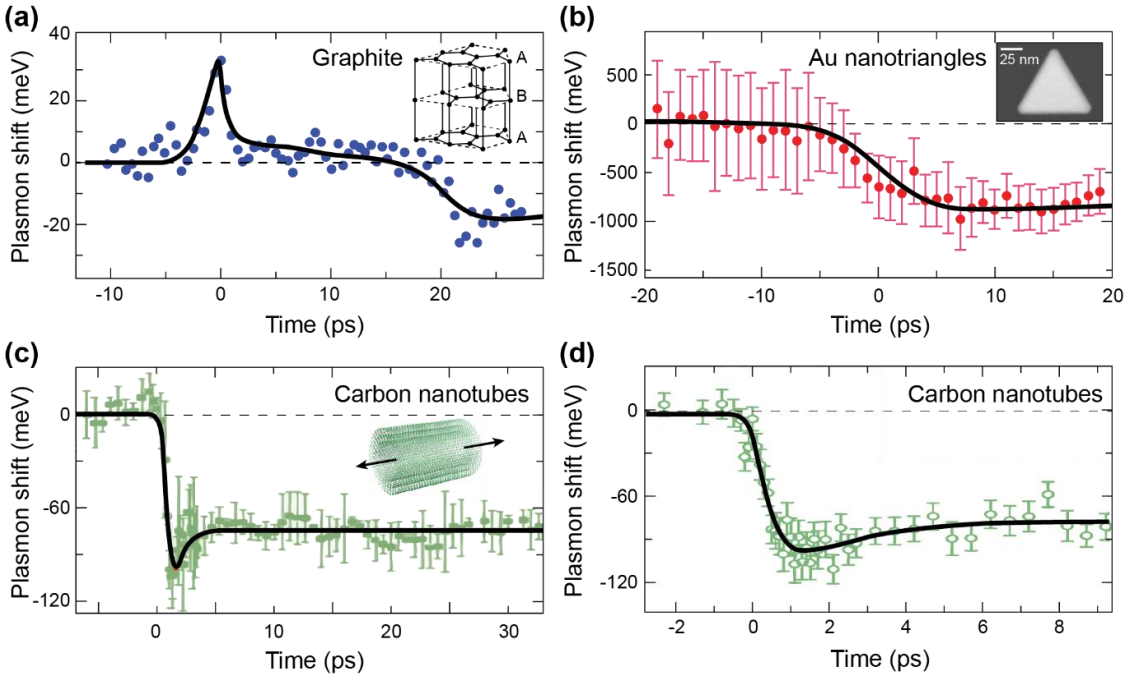

Figure 1.3. Ultrafast low-loss EELS. Time-dependent energy shifts of the bulk plasmon for **(a)** graphite, **(b)** gold (Au) nanotriangles, **(c–d)** and carbon nanotubes. Each inset depicts either the atomic structure or dark-field TEM image. **(a)** Adapted with permission from Ref. 66. **(b)** Adapted with permission from Ref. 69. **(c)** Adapted with permission from Ref. 70. **(d)** Adapted with permission from Ref. 71.

Time- and Momentum-Resolved EELS

One of the key advantages of using electrons as a probe is their ability to provide momentum-resolved information (**Fig. 1.4(a)**). A recent study investigated the ultrafast dynamics of scattering processes and collective excitations in graphite, focusing on how photoexcitation with different pump wavelengths affects valley-specific charge carrier behavior and plasmon dynamics.[72] UED captured pump energy-dependent phonon population dynamics and lattice distortions, providing insight into graphite's structural changes (**Fig. 1.4(b)**). Complementing this, time- and momentum-resolved EELS (tr-q-EELS) tracked the evolution of in-plane π and bulk σ + π plasmons, which are sensitive to both electronic and structural changes (**Fig. 1.4(c)**). Together, these techniques offer a comprehensive view of a

material's photoinduced response, allowing electron–phonon interactions to be directly mapped in reciprocal space.

Graphite's low-loss spectrum at Γ_{000} blueshifts due to increased photocarrier density following photoexcitation (**Fig. 1.4(d)**). To resolve how this photocarrier density is localized within graphite's band structure, tr-q-EELS is measured along the Γ→M direction over 2–8 ps as shown in **Figs. 1.4(e)** and **1.4(f)**. The experimental results clearly demonstrate that plasmon responses depend on both momentum transfer and excitation energy. *Ab initio* DFT simulations accurately reproduce the plasmon dynamics under visible excitation by incorporating effects of thermal lattice expansion and phonon population (**Fig. 1.4(f)**). However, for near-infrared excitation, the simulations fail to fully capture the observed plasmon dynamics (**Fig. 1.4(e)**), suggesting the involvement of additional mechanisms such as long-range charge interactions.

The study demonstrates the ability to control the scattering pathways and plasmonic responses in graphite by tuning the excitation energy. It also highlights the synergistic power of combining diffraction and spectroscopy for probing non-equilibrium states in quantum materials. These findings open avenues for the design of future nanoscale devices that leverage valleytronic and plasmonic functionalities, and they provide a methodological framework for studying related dynamics in other strongly correlated systems including cuprates.

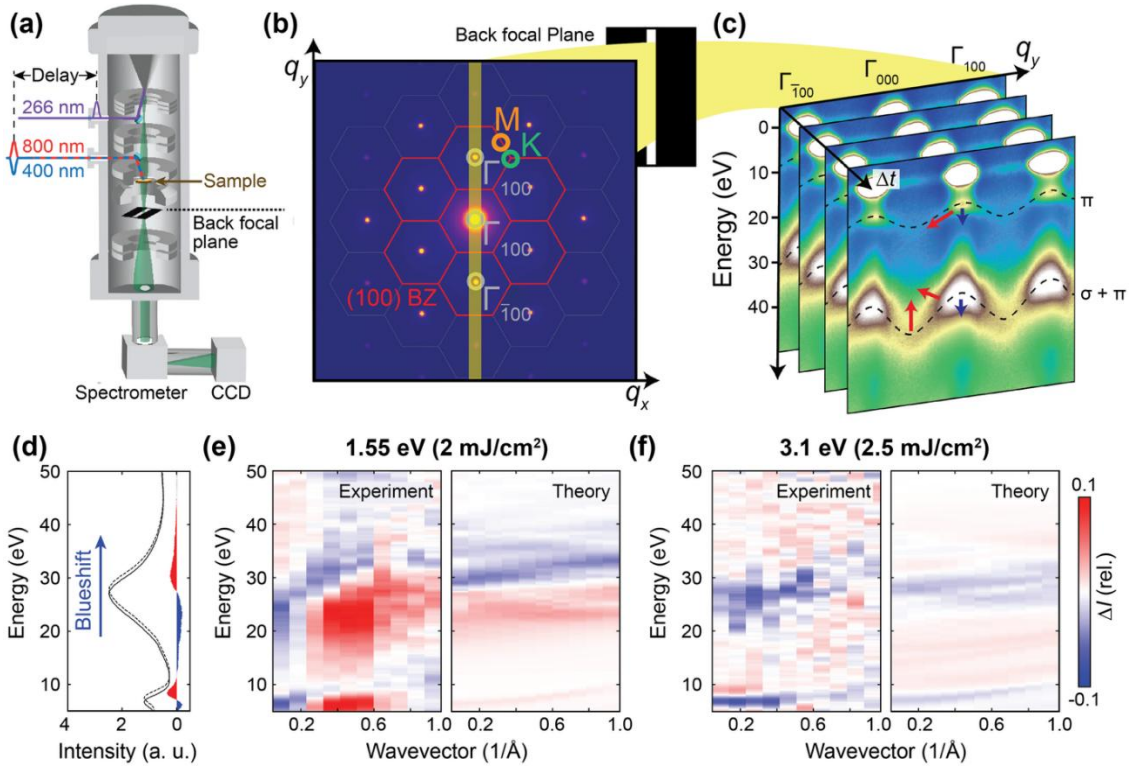

Figure 1.4. Time- and momentum-resolved EELS (tr-q-EELS). (a) Schematic illustration of the tr-q-EELS setup in a UEM where a q-slit at the back focal plane selectively collects scattered electrons along the Γ→M direction. **(b)** Electron diffraction pattern of graphite, highlighting the (100) Brillouin zone (BZ) in red; the yellow rectangle indicates the Γ→M direction. **(c)** Tr-q-EELS acquired along (100) BZ indicates the variable intensity of the π and σ + π plasmons resolved in *k*-space. **(d)** Graphite's EELS response at Γ_{000}. The differential EEL spectrum is obtained using the difference between blueshifted (dashed curve) and unperturbed (solid curve) spectra. **(e,f)** Measured (left) and simulated (right) tr-q-EELS maps along the Γ→M direction for **(e)** 1.55 eV and **(f)** 3.1 eV excitation. Measured spectra are averaged between 2 and 8 ps. Adapted with permission from Ref. 72.

Ultrafast Core-Loss EELS

Ultrafast X-ray absorption spectroscopy probes element-specific carrier and structural dynamics through the X-ray probe's core-level excitation.[73,74] As discussed in **Chapter 1.2**, ultrafast core-loss EELS can, in principle, access the same dynamics as X-ray absorption

under the dipole approximation. However, the nanometer-scale spatial resolution of TEM-EELS allows for localized measurements at features such as junctions, dopants, and defects. Although previous ultrafast core-loss EELS studies have not yet fully exploited the microscope's ultimate spatial resolution, they have demonstrated unique capabilities beyond those of the low-loss EELS techniques described earlier.

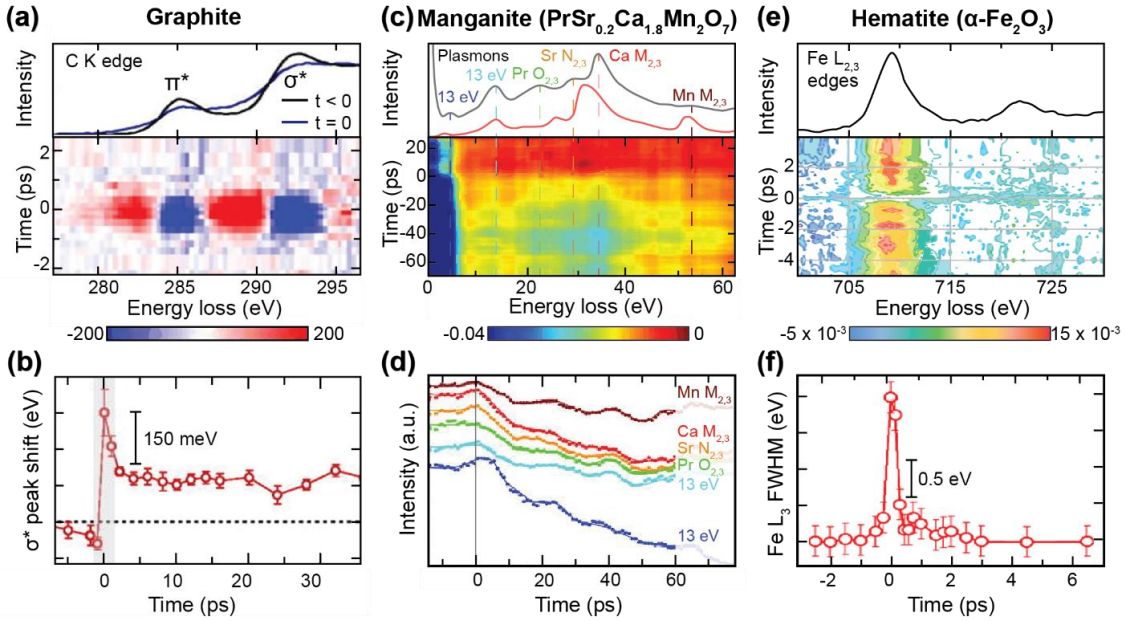

Figure 1.5. Ultrafast core-loss EELS. (a) Ultrafast core-loss EELS of graphite. The electron–photon interaction broadens the spectrum at $\Delta t = 0$ (top) and obscures core-loss dynamics near time zero (bottom). **(b)** Temporal evolution of the σ^* peak. A redshift of the σ^* peak is observed, and the gray-shaded area indicates the time window when PINEM occurs. Adapted with permission from Ref. 75. **(c)** Static experimental (top, gray), simulated (top, red), and transient (bottom) EEL spectra of a $PrSr_{0.2}Ca_{1.8}Mn_2O_7$ film. **(d)** EELS intensity profile for the plasmon and core-level transitions as a function of time delay. Adapted with permission from Ref. 76. **(e)** Static (top) and transient (bottom) Fe $L_{2,3}$ edge of α-Fe_2O_3. **(f)** Intrinsic dynamics of the full width at half maximum (FWHM) of the Fe L_3 edge. Adapted with permission from Ref. 77.

For example, **Figs. 1.5(a)** and **1.5(b)** present ultrafast core-loss EELS measurements of a graphite thin film.[75] In graphite, carbon atoms form strong intralayer σ-bonds with sp^2-hybridized orbitals and weaker interlayer π-bonds with p_z orbitals. These bonding configurations result in distinct absorption peaks in the carbon K edge, as shown in the black spectrum of **Fig. 1.5(a)**. Upon photoexcitation, the transient feature near 290 eV in **Fig. 1.5(a)** arises from a redshift of the peak associated with transitions to empty states with σ^* character (**Fig. 1.5(b)**). This redshift reflects the elongation of the σ-bonds in the basal plane of the photoexcited graphite, as supported by *ab initio* simulations combining molecular dynamics and multiple scattering theory. The prompt redshift of the σ^* peak is attributed to ultrafast energy-gap shrinkage, driven by enhanced electron–phonon interactions following photoexcitation. Notably, a blueshift—typically expected due to thermal lattice contraction—is absent in the transient spectrum, which underscores the sensitivity of core-loss EELS to local bonding changes rather than global lattice responses.

Ultrafast core-loss EELS measurements on bi-layered manganite ($PrSr_{0.2}Ca_{1.8}Mn_2O_7$) demonstrate how correlating diffraction and imaging in the TEM yields a more comprehensive understanding of the electronic and structural dynamics influencing photoexcited core-loss EEL spectra.[76] Here, photothermally induced pressure waves are characterized using UED, while the resulting modulation of the lattice and electronic structure is monitored via ultrafast core-loss EELS. **Figure 1.5(c)** presents both static and transient EEL spectra of manganite in the low-loss region, with plasmon and core-loss features modeled using DFT calculations. As shown in **Fig. 1.5(d)**, the Mn $M_{2,3}$ edges exhibit the highest sensitivity to the coherent structural distortions, and each elemental edge responds differently to these modulations. This highlights the element specificity of the technique.

Beyond photoinduced structural dynamics, ultrafast core-loss EELS has enabled direct observation of charge transfer processes. The charge-transfer dynamics in hematite (α-Fe_2O_3) are probed via the Fe L_3 edge in core-loss EELS, which is sensitive to changes in Fe oxidation state (**Fig. 1.5(e)**).[77] Upon photoexcitation, Fe^{2+}–Fe^{4+} electron–hole pairs generated through Fe 3*d*–3*d* transitions cause a broadening of the Fe L_3 edge (**Fig. 1.5(f)**). Additionally, ultrafast

energy-filtered TEM (EFTEM) is employed to image the charge carrier dynamics in single-crystal hematite, offering potential insights into coupled electronic and structural behavior in future studies.

Despite its potential, ultrafast core-loss EELS faces several challenges. The PINEM effect manifests in femtosecond core-loss EELS near time zero, shown as the spectral broadening in **Figs. 1.5(a)** and **1.5(e)**. This effect can be minimized using a convolution-based average method, which helps extract the intrinsic dynamics of the Fe L_3 edge, as demonstrated in **Fig. 1.5(f)**. Furthermore, core-loss peaks from shallow core levels—such as the peaks shown in **Fig. 1.5(c)**—can overlap with the bulk plasmon, complicating the analysis. As noted in Sec. II, core-level transitions have low scattering cross-sections, and the signal intensity decreases at higher energy loss following the power law. Therefore, careful experimental design is essential to account for both the core-loss scattering cross-section and plasmon overlap.

Ultrafast EELS, although still a rapidly developing technique, has made significant strides in resolving carrier and lattice dynamics in a variety of materials. Current efforts are now focusing on resolving dynamics spatially through spectrum imaging or in momentum space using tr-q-EELS. These ongoing efforts are summarized in **Table 1.I**. Note that the experimental parameters for each report are listed for reference, with intentions to guide future time-resolved and ultrafast EELS efforts. The variables and acronyms within the table (and their meaning) include $\boldsymbol{F}$ (pump fluence), $\boldsymbol{\tau_{laser}}$ (laser pulse width), $\boldsymbol{f_{rep}}$ (laser repetition rate), $\boldsymbol{\beta}$ (collection angle), and $\boldsymbol{V_{acc}}$ (accelerating voltage).

Table 1.I. Reported imaging and optics conditions for ultrafast EELS.

**(NR = not reported)*

Year	Specimen	Loss Region	F (mJ/cm^2)	τ_{laser}	f_{rep}	β	V_{acc}
2009[66,67]	Graphite	Low	5.3	220 fs	100 kHz / 1 MHz	NR	200 kV
2015[70]	SWCNTs	Low	20	220 fs	500 kHz	~7 mrad	NR
2020[71]	SWCNTs	Low	~44	~190 fs	200 kHz	>100 mrad	NR
2022[69]	AuNTs	Low	0.008	150 fs	80 MHz	NR	80 kV
2023[55]	Cu	Low	189	50 fs	100 kHz	NR	200 kV
2023[56]	InAs crystal	Low	1.6	50 fs	1 MHz	NR	200 kV
2025[72]	Graphite	Low	2 and 2.5	NR	1 MHz	NR	200 kV
2014[76]	Manganite	Low and Core	NR	80 fs	1 MHz	NR	NR
2015[75]	Graphite	Core (Low in Supporting Information)	10	~10 ns	6 kHz	10 mrad	NR
				~250 fs	500 kHz		
2017[77]	Hematite	Core	12	NR	500 kHz	NR	NR

1.4 Summary and Outlook

Ultrafast EELS is rapidly evolving into a powerful technique for directly imaging charge, lattice, and heat dynamics across previously inaccessible time and length scales. With its ability to combine sub-nanometer spatial, femtosecond temporal, and variable momentum resolutions, ultrafast EELS uniquely enables the study of transient carrier dynamics and heat dissipation in complex materials and device architectures. UEM EELS has elucidated charge carrier dynamics in real- and momentum-space through revolutionary methods including ultrafast low- and core-loss EELS, CDEM, and tr-q-EELS.

The next frontier for ultrafast EELS will be shaped by efforts to probe functional systems and devices in their working environments (e.g., under applied bias, at variable temperatures, and in gas or liquid media). Integrating *in situ* and operando cells with ultrafast EELS will enable transformative insights into catalytic cycles, thermal transport, quantum phase transitions, and interfacial charge transfer. Monochromated sources, laser-free ultrafast electron pulses, optimized energy-filtered detection, and high-speed time-to-digital converter detectors offer the necessary technological advancements for enhancing technique accessibility and utility. Together, these advances position ultrafast EELS not only as a complementary tool to ultrafast electron diffraction and ultrafast optical and X-ray spectroscopies but as a central platform for visualizing electronic and thermal processes in emerging materials under working conditions. As the field continues to mature, ultrafast EELS will play a key role in uncovering structure–function relationships in next-generation quantum, energy, and nanoscale systems.

1.5 References

(1) Baxter, J. B.; Richter, C.; Schmuttenmaer, C. A. Ultrafast Carrier Dynamics in Nanostructures for Solar Fuels. *Annu. Rev. Phys. Chem.* **2014**, *65*, 423–447.

(2) Shi, J.; Li, Y.; Li, Y.; Li, D.; Luo, Y.; Wu, H.; Meng, Q. From Ultrafast to Ultraslow: Charge-Carrier Dynamics of Perovskite Solar Cells. *Joule* **2018**, *2* (5), 879–901.

(3) Othonos, A. Probing Ultrafast Carrier and Phonon Dynamics in Semiconductors. *J. Appl. Phys.* **1998**, *83* (4), 1789–1830.

(4) Klimov, V. I. Optical Nonlinearities and Ultrafast Carrier Dynamics in Semiconductor Nanocrystals. *J. Phys. Chem. B* **2000**, *104* (26), 6112–6123.

(5) Zhou, L.; Huang, Q.; Xia, Y. Plasmon-Induced Hot Electrons in Nanostructured Materials: Generation, Collection, and Application to Photochemistry. *Chem. Rev.* **2024**, *124* (14), 8597–8619.

(6) Boriskina, S. V.; Ghasemi, H.; Chen, G. Plasmonic Materials for Energy: From Physics to Applications. *Mater. Today* **2013**, *16* (10), 375–386.

(7) Mascaretti, L.; Naldoni, A. Hot Electron and Thermal Effects in Plasmonic Photocatalysis. *J. Appl. Phys.* **2020**, *128* (4), 041101.

(8) Tang, H.; Chen, C.-J.; Huang, Z.; Bright, J.; Meng, G.; Liu, R.-S.; Wu, N. Plasmonic Hot Electrons for Sensing, Photodetection, and Solar Energy Applications: A Perspective. *J. Chem. Phys.* **2020**, *152* (22), 220901.

(9) Cao, S.; Tao, F.; Tang, Y.; Li, Y.; Yu, J. Size- and Shape-Dependent Catalytic Performances of Oxidation and Reduction Reactions on Nanocatalysts. *Chem. Soc. Rev.* **2016**, *45* (17), 4747–4765.

(10) An, K.; Somorjai, G. A. Size and Shape Control of Metal Nanoparticles for Reaction Selectivity in Catalysis. *ChemCatChem* **2012**, *4* (10), 1512–1524.

(11) El-Sayed, M. A. Small Is Different: Shape-, Size-, and Composition-Dependent Properties of Some Colloidal Semiconductor Nanocrystals. *Acc. Chem. Res.* **2004**, *37* (5), 326–333.

(12) Prezhdo, O. V.; Duncan, W. R.; Prezhdo, V. V. Dynamics of the Photoexcited Electron at the Chromophore–Semiconductor Interface. *Acc. Chem. Res.* **2008**, *41* (2), 339–348.

(13) Ginsberg, N. S.; Tisdale, W. A. Spatially Resolved Photogenerated Exciton and Charge Transport in Emerging Semiconductors. *Annu. Rev. Phys. Chem.* **2020**, *71*, 1–30.

(14) Hon, A. The Relation of Aperture and Power in the Microscope (Continued). *J. R. Microsc. Soc.* **1882**, *2* (4), 460–473..

(15) Batson, P. E.; Dellby, N.; Krivanek, O. L. Sub-Ångstrom Resolution Using Aberration Corrected Electron Optics. *Nature* **2002**, *418* (6898), 617–620.

(16) Nellist, P. D.; Chisholm, M. F.; Dellby, N.; Krivanek, O. L.; Murfitt, M. F.; Szilagyi, Z. S.; Lupini, A. R.; Borisevich, A.; Sides, W. H.; Pennycook, S. J. Direct Sub-Angstrom Imaging of a Crystal Lattice. *Science* **2004**, *305* (5691), 1741–1741.

(17) Kisielowski, C.; Freitag, B.; Bischoff, M.; van Lin, H.; Lazar, S.; Knippels, G.; Tiemeijer, P.; van der Stam, M.; von Harrach, S.; Stekelenburg, M.; Haider, M.; Uhlemann, S.; Müller, H.; Hartel, P.; Kabius, B.; Miller, D.; Petrov, I.; Olson, E.; Donchev, T.; Kenik, E.; Lupini, A.; Bentley, J.; Pennycook, S.; Anderson, I.; Minor, A.; Schmid, A.; Duden, T.; Radmilovic, V.; Ramasse, Q.; Watanabe, M.; Erni, R.; Stach, E.; Denes, P.; Dahmen, U. Detection of Single Atoms and Buried Defects in Three Dimensions by Aberration-Corrected Electron Microscope with 0.5-Å Information Limit. *Microsc. Microanal.* **2008**, *14* (5), 469–477.

(18) Erni, R.; Rossell, M. D.; Kisielowski, C.; Dahmen, U. Atomic-Resolution Imaging with a Sub-50-pm Electron Probe. *Phys. Rev. Lett.* **2009**, *102* (9), 096101.

(19) Kimoto, K.; Asaka, T.; Nagai, T.; Saito, M.; Matsui, Y.; Ishizuka, K. Element-Selective Imaging of Atomic Columns in a Crystal Using STEM and EELS. *Nature* **2007**, *450* (7170), 702–704.

(20) Batson, P. E. Simultaneous STEM Imaging and Electron Energy-Loss Spectroscopy with Atomic-Column Sensitivity. *Nature* **1993**, *366* (6457), 727–728.

(21) Jiang, Y.; Chen, Z.; Han, Y.; Deb, P.; Gao, H.; Xie, S.; Purohit, P.; Tate, M. W.; Park, J.; Gruner, S. M.; Elser, V.; Muller, D. A. Electron Ptychography of 2D Materials to Deep Sub-Ångström Resolution. *Nature* **2018**, *559* (7714), 343–349.

(22) Chen, Z.; Jiang, Y.; Shao, Y.-T.; Holtz, M. E.; Odstrčil, M.; Guizar-Sicairos, M.; Hanke, I.; Ganschow, S.; Schlom, D. G.; Muller, D. A. Electron Ptychography Achieves Atomic-Resolution Limits Set by Lattice Vibrations. *Science* **2021**, *372* (6544), 826–831.

(23) Yang, H.; Rutte, R. N.; Jones, L.; Simson, M.; Sagawa, R.; Ryll, H.; Huth, M.; Pennycook, T. J.; Green, M. L. H.; Soltau, H.; Kondo, Y.; Davis, B. G.; Nellist, P. D. Simultaneous Atomic-Resolution Electron Ptychography and Z-Contrast Imaging of Light and Heavy Elements in Complex Nanostructures. *Nat. Commun.* **2016**, *7* (1), 12532.

(24) Ophus, C. Four-Dimensional Scanning Transmission Electron Microscopy (4D-STEM): From Scanning Nanodiffraction to Ptychography and Beyond. *Microsc. Microanal.* **2019**, *25* (3), 563–582.

(25) Zewail, A. H. Four-Dimensional Electron Microscopy. *Science* **2010**, *328* (5975), 187–193.

(26) Flannigan, D. J.; Zewail, A. H. 4D Electron Microscopy: Principles and Applications. *Acc. Chem. Res.* **2012**, *45* (10), 1828–1839.

(27) Barwick, B.; Zewail, A. H. Photonics and Plasmonics in 4D Ultrafast Electron Microscopy. *ACS Photonics* **2015**, *2* (10), 1391–1402.

(28) Barwick, B.; Park, H. S.; Kwon, O.-H.; Baskin, J. S.; Zewail, A. H. 4D Imaging of Transient Structures and Morphologies in Ultrafast Electron Microscopy. *Science* **2008**, *322* (5905), 1227–1231.

(29) Kim, Y.-J.; Park, W.-W.; Nho, H.-W; and Kwon, O.-H. High-Resolution Correlative Imaging in Ultrafast Electron Microscopy. *Adv. Phys. X* **2024**, *9* (1), 2316710.

(30) LaGrange, T.; Cattaneo, P.; Barwick, B.; Flannigan, D. J.; Weissenrieder, J.; Carbone, F. Laser-Driven Ultrafast Transmission Electron Microscopy. *Nat. Rev. Methods Primers* **2025**, *5* (1), 61.

(31) Heller, N. J.; Washington, A. J.; Cushing, S. K. *Electron Energy Loss Spectroscopy*; ACS In Focus; American Chemical Society, 2025.

(32) Kim, Y.-J.; Palmer, L. D.; Lee, W.; Heller, N. J.; Cushing, S. K. Using Electron Energy-Loss Spectroscopy to Measure Nanoscale Electronic and Vibrational Dynamics in a TEM. *J. Chem. Phys.* **2023**, *159* (5), 050901.

(33) Miyata, T.; Fukuyama, M.; Hibara, A.; Okunishi, E.; Mukai, M.; Mizoguchi, T. Measurement of Vibrational Spectrum of Liquid Using Monochromated Scanning Transmission Electron Microscopy–Electron Energy Loss Spectroscopy. *Microscopy* **2014**, *63* (5), 377–382.

(34) Hage, F. S.; Kepaptsoglou, D. M.; Ramasse, Q. M.; Allen, L. J. Phonon Spectroscopy at Atomic Resolution. *Phys. Rev. Lett.* **2019**, *122* (1), 016103.

(35) Granerød, C. S.; Bilden, S. R.; Aarholt, T.; Yao, Y.-F.; Yang, C. C.; Look, D. C.; Vines, L.; Johansen, K. M.; Prytz, Ø. Direct Observation of Conduction Band Plasmons and the Related Burstein-Moss Shift in Highly Doped Semiconductors: A STEM-EELS Study of Ga-Doped ZnO. *Phys. Rev. B* **2018**, *98* (11), 115301.

(36) Zhang, H.-R.; Egerton, R. F.; Malac, M. Local Thickness Measurement through Scattering Contrast and Electron Energy-Loss Spectroscopy. *Micron* **2012**, *43* (1), 8–15.

(37) Zhang, L.; Erni, R.; Verbeeck, J.; Van Tendeloo, G. Retrieving the Dielectric Function of Diamond from Valence Electron Energy-Loss Spectroscopy. *Phys. Rev. B* **2008**, *77* (19), 195119.

(38) Eljarrat, A.; López-Conesa, L.; López-Vidrier, J.; Hernández, S.; Garrido, B.; Magén, C.; Peiró, F.; Estradé, S. Retrieving the Electronic Properties of Silicon Nanocrystals Embedded in a Dielectric Matrix by Low-Loss EELS. *Nanoscale* **2014**, *6* (24), 14971–14983.

(39) Erni, R.; Browning, N. D. The Impact of Surface and Retardation Losses on Valence Electron Energy-Loss Spectroscopy. *Ultramicroscopy* **2008**, *108* (2), 84–99.

(40) Keast, V. J. Ab Initio Calculations of Plasmons and Interband Transitions in the Low-Loss Electron Energy-Loss Spectrum. *J. Electron Spectrosc. Relat. Phenom.* **2005**, *143* (2), 97–104.

(41) Haberfehlner, G.; Orthacker, A.; Albu, M.; Li, J.; Kothleitner, G. Nanoscale Voxel Spectroscopy by Simultaneous EELS and EDS Tomography. *Nanoscale* **2014**, *6* (23), 14563–14569.

(42) Schmid, H.; Okunishi, E.; Mader, W. Defect Structures in ZnO Studied by High-Resolution Structural and Spectroscopic Imaging. *Ultramicroscopy* **2013**, *127*, 76–84.

(43) Muller, D. A. Simple Model for Relating EELS and XAS Spectra of Metals to Changes in Cohesive Energy. *Phys. Rev. B* **1998**, *58* (10), 5989–5995.

(44) Crescenzi, M. D.; Chiarello, G. Extended Energy Loss Fine Structure Measurement Above Shallow and Deep Core Levels of 3d Transition Metals. *J. Phys. C: Solid State Phys.* **1985**, *18* (18), 3595.

(45) Kittel, C.; McEuen, P. *Introduction to Solid State Physics*; John Wiley & Sons, 2018.

(46) Drude, P. Zur Elektronentheorie Der Metalle. *Ann. Phys.* **1900**, *306* (3), 566–613.

(47) Drude, P. Zur Elektronentheorie Der Metalle; II. Teil. Galvanomagnetische Und Thermomagnetische Effecte. *Ann. Phys.* **1900**, *308* (11), 369–402.

(48) Raether, H. *Excitation of Plasmons and Interband Transitions by Electrons*; Springer, 2006.

(49) Groot, F. de; Kotani, A. *Core Level Spectroscopy of Solids*; Advances in condensed matter science; CRC Press: Boca Raton, 2008.

(50) Auerhammer, J. M.; Rez, P. Dipole-Forbidden Excitations in Electron-Energy-Loss Spectroscopy. *Phys. Rev. B* **1989**, *40* (4), 2024–2030.

(51) Löffler, S.; Ennen, I.; Tian, F.; Schattschneider, P.; Jaouen, N. Breakdown of the Dipole Approximation in Core Losses. *Ultramicroscopy* **2011**, *111* (8), 1163–1167.

(52) Keast, V. J.; Scott, A. J.; Brydson, R.; Williams, D. B.; Bruley, J. Electron Energy-Loss near-Edge Structure – a Tool for the Investigation of Electronic Structure on the Nanometre Scale. *J. Microsc.* **2001**, *203* (2), 135–175.

(53) Sarikaya, M.; Qian, M.; Stern, E. A. EXELFS Revisited. *Micron* **1996**, *27* (6), 449–466.

(54) Thomas, P. J.; Midgley, P. A. An Introduction to Energy-Filtered Transmission Electron Microscopy. *Top. Catal.* **2002**, *21* (4), 109–138.

(55) Madan, I.; Dias, E. J. C.; Gargiulo, S.; Barantani, F.; Yannai, M.; Berruto, G.; LaGrange, T.; Piazza, L.; Lummen, T. T. A.; Dahan, R.; Kaminer, I.; Vanacore, G. M.; García de Abajo, F. J.; Carbone, F. Charge Dynamics Electron Microscopy: Nanoscale Imaging of Femtosecond Plasma Dynamics. *ACS Nano* **2023**, *17* (4), 3657–3665.

(56) Yannai, M.; Dahan, R.; Gorlach, A.; Adiv, Y.; Wang, K.; Madan, I.; Gargiulo, S.; Barantani, F.; Dias, E. J. C.; Vanacore, G. M.; Rivera, N.; Carbone, F.; García de Abajo, F. J.; Kaminer, I. Ultrafast Electron Microscopy of Nanoscale Charge Dynamics in Semiconductors. *ACS Nano* **2023**, *17* (4), 3645–3656.

(57) Barwick, B.; Flannigan, D. J.; Zewail, A. H. Photon-Induced Near-Field Electron Microscopy. *Nature* **2009**, *462* (7275), 902–906.

(58) Park, S. T.; Lin, M.; Zewail, A. H. Photon-Induced Near-Field Electron Microscopy (PINEM): Theoretical and Experimental. *New J. Phys.* **2010**, *12* (12), 123028.

(59) Tanriover, I.; Li, Y.; Gage, T. E.; Arslan, I.; Liu, H.; Mirkin, C. A.; Aydin, K. Unveiling Spatial and Temporal Dynamics of Plasmon-Enhanced Localized Fields in Metallic

Nanoframes through Ultrafast Electron Microscopy. *ACS Nano* **2024**, *18* (41), 28258–28267.

(60) Liu, H.; Gage, T. E.; Singh, P.; Jaiswal, A.; Schaller, R. D.; Tang, J.; Park, S. T.; Gray, S. K.; Arslan, I. Visualization of Plasmonic Couplings Using Ultrafast Electron Microscopy. *Nano Lett.* **2021**, *21* (13), 5842–5849.

(61) Liebtrau, M.; Sivis, M.; Feist, A.; Lourenço-Martins, H.; Pazos-Pérez, N.; Alvarez-Puebla, R. A.; de Abajo, F. J. G.; Polman, A.; Ropers, C. Spontaneous and Stimulated Electron–Photon Interactions in Nanoscale Plasmonic Near Fields. *Light Sci. Appl.* **2021**, *10* (1), 82.

(62) Zheng, D.; Huang, S.; Zhu, C.; Xu, P.; Li, Z.; Wang, H.; Li, J.; Tian, H.; Yang, H.; Li, J. Nanoscale Visualization of a Photoinduced Plasmonic Near-Field in a Single Nanowire by Free Electrons. *Nano Lett.* **2021**, *21* (24), 10238–10243.

(63) Wang, K.; Dahan, R.; Shentcis, M.; Kauffmann, Y.; Ben Hayun, A.; Reinhardt, O.; Tsesses, S.; Kaminer, I. Coherent Interaction between Free Electrons and a Photonic Cavity. *Nature* **2020**, *582* (7810), 50–54.

(64) Dahan, R.; Nehemia, S.; Shentcis, M.; Reinhardt, O.; Adiv, Y.; Shi, X.; Be'er, O.; Lynch, M. H.; Kurman, Y.; Wang, K.; Kaminer, I. Resonant Phase-Matching between a Light Wave and a Free-Electron Wavefunction. *Nat. Phys.* **2020**, *16* (11), 1123–1131.

(65) Priebe, K. E.; Rathje, C.; Yalunin, S. V.; Hohage, T.; Feist, A.; Schäfer, S.; Ropers, C. Attosecond Electron Pulse Trains and Quantum State Reconstruction in Ultrafast Transmission Electron Microscopy. *Nat. Photon.* **2017**, *11* (12), 793–797.

(66) Carbone, F.; Kwon, O.-H.; Zewail, A. H. Dynamics of Chemical Bonding Mapped by Energy-Resolved 4D Electron Microscopy. *Science* **2009**, *325* (5937), 181–184.

(67) Carbone, F.; Barwick, B.; Kwon, O.-H.; Park, H. S.; Spencer Baskin, J.; Zewail, A. H. EELS Femtosecond Resolved in 4D Ultrafast Electron Microscopy. *Chem. Phys. Lett.* **2009**, *468* (4), 107–111.

(68) Carbone, F. The Interplay between Structure and Orbitals in the Chemical Bonding of Graphite. *Chem. Phys. Lett.* **2010**, *496* (4), 291–295.

(69) Kuwahara, M.; Mizuno, L.; Yokoi, R.; Morishita, H.; Ishida, T.; Saitoh, K.; Tanaka, N.; Kuwahara, S.; Agemura, T. Transient Electron Energy-Loss Spectroscopy of Optically Stimulated Gold Nanoparticles Using Picosecond Pulsed Electron Beam. *Appl. Phys. Lett.* **2022**, *121* (14), 143503.

(70) Vanacore, G. M.; van der Veen, R. M.; Zewail, A. H. Origin of Axial and Radial Expansions in Carbon Nanotubes Revealed by Ultrafast Diffraction and Spectroscopy. *ACS Nano* **2015**, *9* (2), 1721–1729.

(71) Zheng, D.; Zhu, C.; Li, Z.; Li, Z.; Li, J.; Sun, S.; Zhang, Y.; Wang, F.; Tian, H.; Yang, H.; Li, J. Ultrafast Lattice and Electronic Dynamics in Single-Walled Carbon Nanotubes. *Nanoscale Adv.* **2020**, *2* (7), 2808–2813.

(72) Barantani, F.; Claude, R.; Iyikanat, F.; Madan, I.; Sapozhnik, A. A.; Puppin, M.; Weaver, B.; LaGrange, T.; Abajo, F. J. G. de; Carbone, F. Ultrafast Momentum-Resolved Visualization of the Interplay between Phonon-Mediated Scattering and Plasmons in Graphite. *Sci. Adv.* **2025**, *11* (14), eadu1001.

(73) Kraus, P. M.; Zürch, M.; Cushing, S. K.; Neumark, D. M.; Leone, S. R. The Ultrafast X-ray Spectroscopic Revolution in Chemical Dynamics. *Nat. Rev. Chem.* **2018**, *2* (6), 82–94.

(74) Liu, H.; Klein, I. M.; Michelsen, J. M.; Cushing, S. K. Element-Specific Electronic and Structural Dynamics Using Transient XUV and Soft X-ray Spectroscopy. *Chem* **2021**, *7* (10), 2569–2584.

(75) van der Veen, R. M.; Penfold, T. J.; Zewail, A. H. Ultrafast Core-Loss Spectroscopy in Four-Dimensional Electron Microscopy. *Struct. Dyn.* **2015**, *2* (2), 024302.

(76) Piazza, L.; Ma, C.; Yang, H. X.; Mann, A.; Zhu, Y.; Li, J. Q.; Carbone, F. Ultrafast Structural and Electronic Dynamics of the Metallic Phase in a Layered Manganite. *Struct. Dyn.* **2013**, *1* (1), 014501.

(77) Su, Z.; Baskin, J. S.; Zhou, W.; Thomas, J. M.; Zewail, A. H. Ultrafast Elemental and Oxidation-State Mapping of Hematite by 4D Electron Microscopy. *J. Am. Chem. Soc.* **2017**, *139* (13), 4916–4922.

Chapter 2

NONEQUILIBRIUM RESHAPING OF THE SILICON BULK PLASMON UNDER DENSE PHOTOEXCITATION

Adapted with permission from the following:

Lee, W.; Palmer, L. D.; Gage, T. E.; Cushing, S. K. Nonequilibrium Reshaping of the Silicon Bulk Plasmon under Dense Photoexcitation. *In preparation*.

2.1 Introduction

The interaction of intense femtosecond optical pulses with semiconductors drives the electronic system far from equilibrium and produces transient states that evolve on ultrafast timescales.[1–3] Following photoexcitation, electrons and holes are promoted across the band structure into non-thermal distributions.[4] These excited carriers subsequently undergo carrier–carrier scattering, dynamic screening, quasiparticle renormalization, and carrier–phonon coupling, leading to time-dependent modifications of the electronic structure and dielectric response.[5] Understanding how these nonequilibrium processes influence collective excitations is central to ultrafast science and to the broader goal of controlling a material's properties with light.

Among the available probes of nonequilibrium dynamics, the bulk plasmon is particularly sensitive because it is governed by the frequency-dependent dielectric function of a material.[6] Within a simple free-electron description, the bulk plasmon frequency is determined primarily by the carrier density and effective mass.[7] In covalent semiconductors such as silicon, however, the situation is considerably more complex. The bulk plasmon near 16.8 eV originates from collective oscillations of valence electrons and is strongly influenced by band dispersion, screening, local-field effects, and many-body interactions.[8–11] Under strong photoexcitation, these contributions can evolve simultaneously such that changes in plasmon

energy, linewidth, and spectral weight encode complementary information about transient dielectric renormalization.

Silicon provides an ideal platform for studying these effects because its equilibrium electronic structure is well characterized, while femtosecond optical excitation can generate dense electron–hole populations approaching 10^{21} cm^{-3}.[12] In this regime, photoexcitation does not simply introduce a Drude-like free-carrier population into a fixed background. Instead, the excited carriers modify the screening environment and alter the electronic structure governing the collective response of valence electrons. Consequently, screening,[13] band-structure renormalization,[14] and transient weakening of covalent bonding[15,16] can all contribute to the nonequilibrium plasmon response.

Here, we employ ultrafast electron energy-loss spectroscopy (EELS) to directly probe the evolution of the silicon bulk plasmon following femtosecond optical excitation as illustrated in **Fig. 2.1(a)**. The central experimental result is a correlated reshaping of the low-loss response: the plasmon redshifts, broadens, and exhibits an increased spectral weight. This combination is more robust than the energy shift alone because it directly shows that photoexcitation redistributes spectral intensity away from the sharper plasmon maximum and into a broader low-loss response.

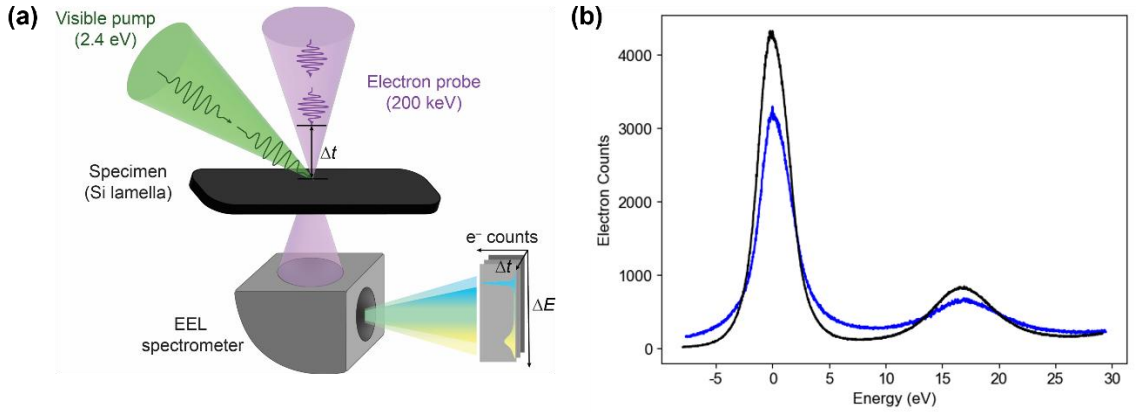

Figure 2.1. Ultrafast low-loss electron energy-loss spectroscopy (EELS) of photoexcited silicon. (a) Schematic of the time-resolved EELS measurement. A 515 nm optical pump excites electron–hole pairs in crystalline silicon, while an electron probe measures the transient low-loss EEL spectrum as a function of time delay. **(b)** Representative low-loss EEL spectra acquired before (black) and immediately after photoexcitation (blue), highlighting the transient changes of the bulk plasmon peak following photoexcitation.

2.2 Methods

In the ultrafast EELS experiments, a femtosecond optical pump pulse was used to excite electron−hole pairs across the silicon band structure, driving the specimen into a transient nonequilibrium electronic state (**Fig. B.1**). The subsequent evolution of this state was probed by a time-delayed ultrafast electron pulse though acquisition of low-loss EEL spectra at controlled time delays. In the low-loss region, the measured EELS intensity is proportional to the energy-loss function:[17]

$$\mathrm{Im}\left[-\frac{1}{\epsilon(\omega,\Delta t)}\right] \tag{2.1}$$

where $\epsilon(\omega,\Delta t)$ is the transient dielectric function at frequency ω and time delay Δt. The bulk plasmon appears as a pronounced peak in the loss function and is determined by the condition:[18]

$$\mathrm{Re}[\epsilon(\omega, \Delta t)] = 0, \qquad \mathrm{Im}[\epsilon(\omega, \Delta t)] \ll 1 \tag{2.2}$$

such that transient changes in the plasmon energy, linewidth, and spectral weight provide a direct measure of photoinduced modifications to the dielectric response of silicon.

Although the incident electron probe can also generate electron–hole pairs in silicon, this contribution is negligible under the experimental conditions. Using Werner's formalism to estimate beam-induced carrier generation,[19,20] the carrier density generated by the electron probe was estimated to be below 10^8 cm^{-3}, which is many orders of magnitude smaller than the photoexcited carrier density (**Fig. B.2**). Therefore, the transient electronic response observed in the EEL spectra is dominated by photoexcitation rather than carriers induced by the electron beam.

Ultrafast EELS measurements were performed using the ultrafast electron microscope (UEM) at the Center for Nanoscale Materials, Argonne National Laboratory. The instrument is based on a modified JEOL JEM-2100 Plus transmission electron microscope integrated with a femtosecond laser system. A Light Conversion laser operating at a fundamental wavelength of 1030 nm, with a pulse duration of 280 fs and repetition rate of 10 kHz, was used for the pump–probe experiments. The laser output was divided into pump and probe paths using a beam splitter. In the probe path, the laser beam was frequency-quadrupled to 257 nm and directed onto the LaB_6 photocathode to generate ultrafast electron wave packets. In the pump path, the laser beam was frequency-doubled to 515 nm and used to photoexcite a crystalline silicon lamella with a thickness of 150 nm. The photoexcited carrier density was estimated to be 9.2×10^{20} cm^{-3} from the pump fluence and energy, together with the specimen thickness and the reflectivity and absorption coefficient of silicon at 515 nm. Details of this calculation are provided in **Appendix B**.

Low-loss EEL spectra were acquired as a function of time delay to measure the transient bulk plasmon response following photoexcitation. Spectra acquired at negative time delays were used as the steady-state reference state. Measurements were performed over a delay range of −500 to 2500 ps with a temporal step size of 25 ps and three acquisition loops. At each time

delay, spectra were collected with an exposure time of 100 s at an acceleration voltage of 200 kV.

2.3 Results and Discussion

Figure 2.1(b) shows representative low-loss EEL spectra of silicon, including the zero-loss peak (ZLP) and bulk plasmon peak. The ZLP and bulk plasmons are fitted using Voigt and Lorentzian functions, respectively, which provided the lowest reduced chi-square values among the tested fitting models. Details of the fitting procedure are provided in **Appendix B**. The same fitting functions are used for all time delays to extract the peak position, linewidth, and amplitude.

Following photoexcitation, the bulk plasmon exhibits a prompt shift to lower energy (**Fig 2.2 (a)**). The bulk plasmon energy is determined from the energy difference between the fitted bulk plasmon position and ZLP position for each spectrum. This procedure removes contributions from energy-axis drift. As shown in **Fig. 2.2(b)**, the maximum redshift reaches approximately –170 meV relative to its equilibrium plasmon energy near 16.8 eV, corresponding to a fractional shift of ~1%.

The magnitude of this redshift can be compared with a simple free-carrier screening estimate. For a screened valence plasmon frequency,[21]

$$\omega_p' = \sqrt{\frac{n_v e^2}{\epsilon_0 m^* \epsilon_\infty}} \tag{2.3}$$

where n_v is the valence electron density participating in the collective excitation, m^* is an effective electronic mass, and ϵ_∞ is the high-frequency dielectric constant. In the presence of photoexcited carriers, the leading-order effect can be written as

$$\frac{\Delta E_p'}{E_p'} \approx -\frac{1}{2}\frac{\Delta \epsilon}{\epsilon_\infty}. \tag{2.4}$$

Within a linear-response picture, the additional screening scales approximately with the photoexcited carrier density, $\Delta\epsilon \propto n_{ph}$, giving the approximate scaling

$$\frac{\Delta E_p'}{E_p'} \sim -\frac{1}{2}\frac{n_{ph}}{n_v}. \tag{2.5}$$

For a photoexcited carrier density of 9.2×10^{20} cm^{-3} and valence electron density of 2×10^{23} cm^{-3} in silicon, the fractional change is $n_{ph}/n_v = 4.6 \times 10^{-3}$, corresponding to a predicted screening-induced redshift of –38 meV. Therefore, perturbative free-carrier screening accounts for only a fraction of the experimentally observed –170 meV shift. This comparison does not uniquely identify the missing microscopic mechanism, but it rules out a purely scalar free-carrier screening picture.

The remaining redshift likely reflects additional modifications of the dielectric response induced by dense photoexcitation. Possible contributions include carrier-induced changes in interband screening, band-structure renormalization, transient changes in band curvature and effective mass, and modifications of bonding character. In this work, we therefore treat them collectively as additional dielectric-response renormalization beyond the simple screening estimate.

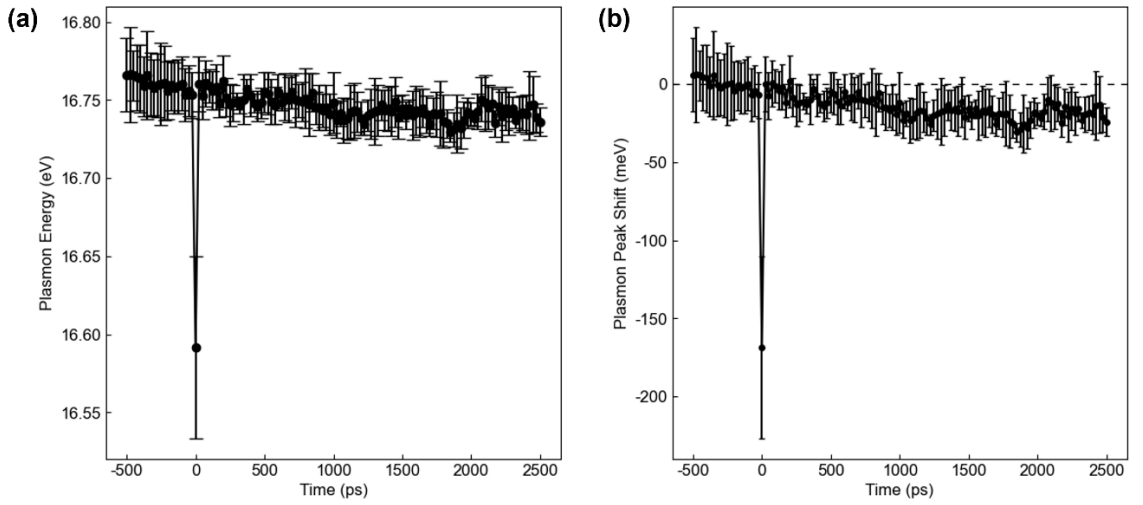

Figure 2.2. Ultrafast redshift of the silicon bulk plasmon. (a) Extracted bulk plasmon energy as a function of time delay. **(b)** Plasmon energy shift relative to the negative-delay equilibrium value. The maximum redshift reaches approximately −170 meV at a photoexcited carrier density of 9.2×10^{20} cm^{-3}.

The bulk plasmon linewidth broadens over the same delay range in which the redshift is observed (**Fig 2.3(a)**). The measured plasmon linewidth contains contributions from both the intrinsic material response and instrumental energy resolution. The instrumental contribution is tracked by the full width at half maximum (FWHM) of the ZLP, which reflects the probe energy distribution, spectrometer stability, and possible pump-induced broadening of the electron beam.[22,23] A key experimental observation is that the bulk plasmon linewidth increases more strongly than the ZLP linewidth (**Fig. 2.3(b)**). This indicates that the plasmon broadening cannot be attributed solely to instrumental broadening or changes in the probe energy resolution.

Instead, the enhanced plasmon linewidth reflects an increase in intrinsic damping of the collective excitation. In the energy-loss function, the plasmon linewidth corresponds to the damping rate of the collective charge oscillation.[24] A broader plasmon peak therefore corresponds to a shorter plasmon lifetime and stronger damping. Under dense

photoexcitation, this damping can arise from additional carrier-induced scattering channels, enhanced electron–hole interactions, transient disorder in the electronic distribution, and redistribution of oscillator strength into nearby loss channels. The simultaneous redshift and broadening therefore suggest that photoexcitation both weakens the effective restoring force of the bulk plasmon and increases its damping rate.

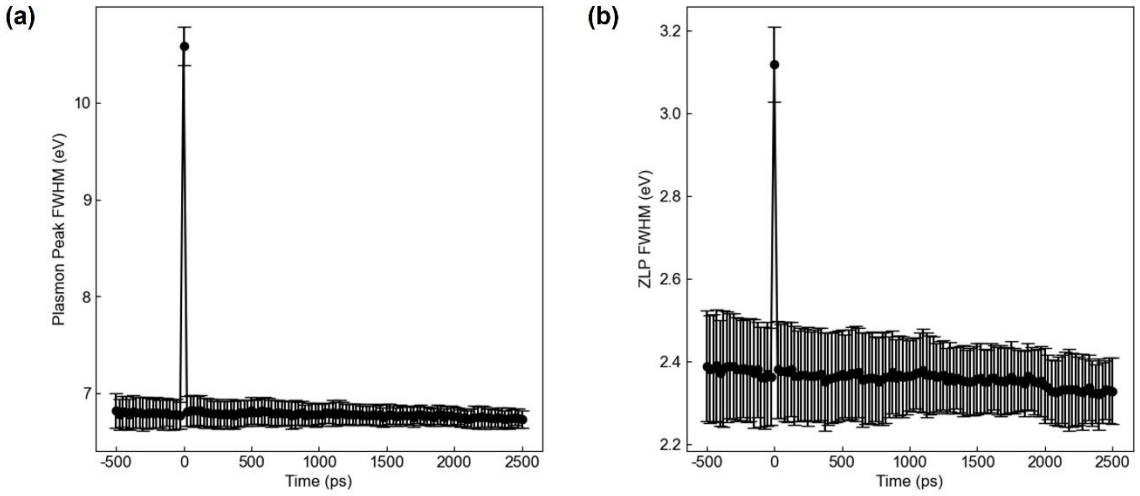

Figure 2.3. Time-dependent broadening of the bulk plasmon peak and zero-loss peak (ZLP). (a) Full width at half maximum (FWHM) of the bulk plasmon peak as function of time delay. **(b)** FWHM of the ZLP as a function of time delay.

To further examine how the bulk plasmon response changes after photoexcitation, the bulk plasmon spectral weight is evaluated by integrating the EELS intensity over a moving window centered on the fitted plasmon peak position and normalizing by the integrated ZLP area from the same spectrum:

$$W_{pl}(\Delta t) = \frac{\int_{E_p(\Delta t)-7.5\ \mathrm{eV}}^{E_p(\Delta t)+7.5\ \mathrm{eV}} I(E,\ \Delta t)\, dE}{\int_{E_{ZLP}(\Delta t)-5.0\ \mathrm{eV}}^{E_{ZLP}(\Delta t)+5.0\ \mathrm{eV}} I(E,\ \Delta t)\, dE}. \tag{2.6}$$

Here, $E_p(\Delta t)$ and $E_{ZLP}(\Delta t)$ are the fitted bulk plasmon and ZLP positions for each spectrum. The integration windows are chosen to capture the full plasmon peak region and elastic scattering intensity while following time-dependent peak shifts. Normalization by the ZLP area accounts for time-dependent changes in the electron-beam current, total counts, and elastic scattering intensity.

At time zero, the bulk plasmon peak amplitude decreases (**Fig. 2.4(a)**). This indicates that the plasmon response becomes less sharply concentrated at the peak maximum after photoexcitation. In contrast, the integrated plasmon spectral weight $W_{pl}(\Delta t)$ increases (**Fig. 2.4(b)**). This contrast between decreasing peak amplitude and increasing integrated spectral weight is consistent with the linewidth analysis in **Fig 2.3**. Since the bulk plasmon broadens more strongly than the ZLP, the increase in $W_{pl}(\Delta t)$ cannot be explained by a degradation of instrumental resolution. Rather, the loss intensity is redistributed over a wider energy range around the plasmon resonance.

This behavior indicates that photoexcitation does not merely shift the bulk plasmon peak, but reshapes the energy-loss function itself. The sharper equilibrium plasmon response is suppressed, while spectral intensity spreads across the broader region as additional carrier-induced damping and loss channels become active. Therefore, the increase in the integrated plasmon spectral weight should not be interpreted as an independent enhancement of a coherent plasmon mode. Instead, it reflects damping-driven spectral redistribution within the plasmon window, consistent with the observed increase in plasmon linewidth.

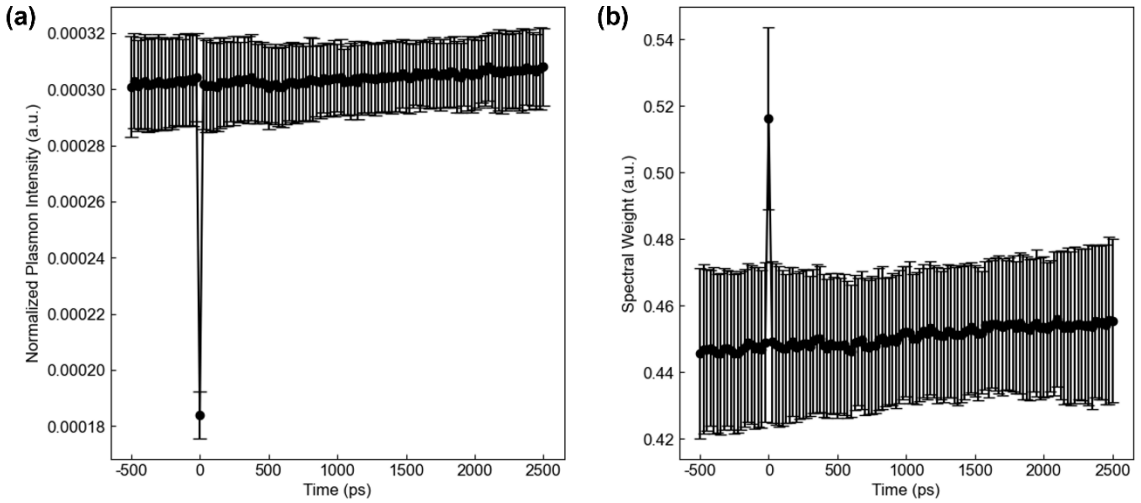

Figure 2.4. Photoinduced redistribution of plasmon spectral weight. (a) Fitted bulk plasmon peak amplitude as a function of time delay. The prompt decrease in amplitude indicates suppression of the sharp plasmon maximum after photoexcitation. **(b)** Normalized plasmon spectral weight obtained by integrating the loss intensity over a moving window centered on the fitted plasmon position and normalizing by the ZLP area.

Taken together, the measurements show that dense photoexcitation reshapes the silicon bulk plasmon loss feature. The energy redshift demonstrates that the real part of the dielectric response is modified. The linewidth broadening indicates increased damping. The simultaneous decrease in peak amplitude and increase in spectral weight show that intensity is redistributed away from the sharper plasmon maximum into a broader plasmon-loss region. These correlated observables provide stronger evidence for nonequilibrium reshaping of the loss function.

2.4 Conclusions

In conclusion, time-resolved EELS reveals that 515 nm excitation of crystalline silicon at a carrier density of 9.2×10^{20} cm^{-3} produces a prompt −170 meV redshift of the bulk plasmon near 16.8 eV. The shift is accompanied by linewidth broadening beyond the ZLP response, suppression of the plasmon peak intensity, and increased spectral weight within the plasmon

energy window. A screening estimate gives only –38 meV at this density, indicating that the observed response cannot be explained by a simple free-carrier picture alone. Instead, the transient plasmon response reflects a broader reshaping of the silicon dielectric function, involving changes in screening, damping, electronic structure, and spectral-weight redistribution under dense photoexcitation. These results establish ultrafast EELS as a sensitive probe of nonequilibrium collective electronic dynamics and motivate quantitative modeling of the coupled electronic and thermal contributions to the transient dielectric response.

2.5 References

(1) Rossi, F.; Kuhn, T. Theory of Ultrafast Phenomena in Photoexcited Semiconductors. *Rev. Mod. Phys.* **2002**, *74* (3), 895–950.

(2) Sundaram, S. K.; Mazur, E. Inducing and Probing Non-Thermal Transitions in Semiconductors Using Femtosecond Laser Pulses. *Nat. Mater.* **2002**, *1* (4), 217–224.

(3) Elsaesser, T.; Woerner, M. Femtosecond Infrared Spectroscopy of Semiconductors and Semiconductor Nanostructures. *Phys. Rep.* **1999**, *321* (6), 253–305.

(4) Shah, J. *Ultrafast Spectroscopy of Semiconductors and Semiconductor Nanostructures*; Springer Science & Business Media, 2013.

(5) Kira, M.; Koch, S. W. Many-Body Correlations and Excitonic Effects in Semiconductor Spectroscopy. *Prog. Quantum Electron.* **2006**, *30* (5), 155–296.

(6) Pines, D.; Bohm, D. A Collective Description of Electron Interactions: II. Collective vs Individual Particle Aspects of the Interactions. *Phys. Rev.* **1952**, *85* (2), 338–353.

(7) Ashcroft, N. W.; Mermin, N. D. *Solid State Physics*; Holt, Rinehart and Winston, 1976.

(8) Olevano, V.; Reining, L. Excitonic Effects on the Silicon Plasmon Resonance. *Phys. Rev. Lett.* **2001**, *86* (26), 5962–5965.

(9) Daling, R.; van Haeringen, W.; Farid, B. Plasmon Dispersion in Silicon Obtained by Analytic Continuation of the Random-Phase-Approximation Dielectric Matrix. *Phys. Rev. B* **1991**, *44* (7), 2952–2960.

(10) Weissker, H.-C.; Serrano, J.; Huotari, S.; Bruneval, F.; Sottile, F.; Monaco, G.; Krisch, M.; Olevano, V.; Reining, L. Signatures of Short-Range Many-Body Effects in the Dielectric Function of Silicon for Finite Momentum Transfer. *Phys. Rev. Lett.* **2006**, *97* (23), 237602.

(11) Car, R.; Tosatti, E.; Baroni, S.; Leelaprute, S. Dielectric Band Structure of Crystals: General Properties and Calculations for Silicon. *Phys. Rev. B* **1981**, *24* (2), 985–999.

(12) Sokolowski-Tinten, K.; von der Linde, D. Generation of Dense Electron-Hole Plasmas in Silicon. *Phys. Rev. B* **2000**, *61* (4), 2643–2650.

(13) Rossi, F.; Kuhn, T. Theory of Ultrafast Phenomena in Photoexcited Semiconductors. *Rev. Mod. Phys.* **2002**, *74* (3), 895–950.

(14) Reeves, C. C.; Cushing, S. K.; Vlček, V. Role of Effective Mass and Long-Range Interactions in the Band-Gap Renormalization of Photoexcited Semiconductors. *Phys. Rev. B* **2025**, *112* (7), 075105.

(15) Stampfli, P.; Bennemann, K. H. Time Dependence of the Laser-Induced Femtosecond Lattice Instability of Si and GaAs: Role of Longitudinal Optical Distortions. *Phys. Rev. B* **1994**, *49* (11), 7299–7305.

(16) De Angelis, D.; Principi, E.; Bencivenga, F.; Fausti, D.; Foglia, L.; Klein, Y.; Manfredda, M.; Mincigrucci, R.; Montanaro, A.; Pedersoli, E.; Pelli Cresi, J. S.; Perosa, G.; Prince, K. C.; Razzoli, E.; Shwartz, S.; Simoncig, A.; Spampinati, S.; Svetina, C.; Szlachetko, J.; Tripathi, A.; Vartanyants, I. A.; Zangrando, M.; Capotondi, F. Free Electron Laser Stochastic Spectroscopy Revealing Silicon Bond Softening Dynamics. *Phys. Rev. B* **2023**, *107* (21), 214305.

(17) Egerton, R. F. *Electron Energy-Loss Spectroscopy in the Electron Microscope*; Springer US: Boston, MA, 2011.

(18) Joshi, N.; Jangir, S.; Joshi, K. B. Optical Response and Electron Energy Loss Spectra of Boron Arsenide Using Linear Response Theory. *RSC Adv.* **2026**, *16* (17), 15266–15282.

(19) Werner, U.; Koch, F.; Oelgart, G. Kilovolt Electron Energy Loss Distribution in Si. *J. Phys. D: Appl. Phys.* **1988**, *21* (1), 116.

(20) Zhou, R.; Yu, M.; Tweddle, D.; Hamer, P.; Chen, D.; Hallam, B.; Ciesla, A.; Altermatt, P. P.; Wilshaw, P. R.; Bonilla, R. S. Understanding and Optimizing EBIC pn-Junction Characterization from Modeling Insights. *J. Appl. Phys.* **2020**, *127* (2), 024502.

(21) Kakeshita, T.; Lee, S.; Tajima, S. Anisotropic Drude Response and the Effect of Anisotropic C Substitution in $Mg(B_{1-x}C_x)_2$. *Phys. Rev. Lett.* **2006**, *97* (3), 037002.

(22) Plemmons, D. A.; Tae Park, S.; Zewail, A. H.; Flannigan, D. J. Characterization of Fast Photoelectron Packets in Weak and Strong Laser Fields in Ultrafast Electron Microscopy. *Ultramicroscopy* **2014**, *146*, 97–102.

(23) Bellido, E. P.; Rossouw, D.; Botton, G. A. Toward 10 meV Electron Energy-Loss Spectroscopy Resolution for Plasmonics. *Microsc. Microanal.* **2014**, *20* (3), 767–778.

(24) Sánchez, A. M.; Beanland, R.; Gass, M. H.; Papworth, A. J.; Goodhew, P. J.; Hopkinson, M. Mapping Quantum Dot-in-Well Structures on the Nanoscale Using the Plasmon Peak in Electron Energy Loss Spectra. *Phys. Rev. B* **2005**, *72* (7), 075339.

C h a p t e r 3

ELECTRONIC TOPOLOGICAL TRANSITIONS IN CADMIUM UNDER PRESSURE STUDIED VIA THEORETICAL AND EXPERIMENTAL X-RAY ABSORPTION SPECTROSCOPY

Adapted with permission from the following:

Hinton, J. K.†; Schacher, D.†; Lee, W.†; Smith, G. A.†; Siska, E.; Park, C.; Ellison, P. B.; Cushing, S. K.; Schwartz, C. P.; Lawler, K. V.; Salamat, A. Electronic Topological Transitions in Cadmium under Pressure Studied via Theoretical and Experimental X-ray Absorption Spectroscopy. *Phys. Rev. B* **2024**, *110* (20), 205118. https://doi.org/10.1103/PhysRevB.110.205118.

† indicates equal contributions.

3.1 Introduction

The ground-state allotrope of elemental cadmium (Cd) remains in the hexagonal close-packed (hcp) structural motif under high-pressure compression up to 174 GPa.[1] Based on geometric and energetic considerations, the ideal c/a ratio for hcp is $\sqrt{8/3} \approx 1.633$; however, Cd has an unusually high ambient c/a ratio of about 1.86.[1] Only zinc (Zn) and mercury (Hg) have comparably high c/a ratios.[2] Nonideal c/a ratios often indicate some nontrivial electronic structure, and as such, materials with anomalous c/a ratios, like Cd, are excellent test cases for new probes of electronic structure. A discontinuity in the c/a ratio has historically been used as preliminary evidence of electronic structural changes and cause to further investigate such electronic properties via the topology of the Fermi surface.[3–7]

The topology of the Fermi surface indicates the relative position in reciprocal space of the electrons at the Fermi energy and can be used to understand a variety of other properties of

a material in the metallic state.[8] With increasing pressures and no structural phase transitions, the Fermi surface will change continuously.[9] The presence of a noncontinuous deformation of the Fermi surface indicates a nontrivial change in the electronic structure and is known as an electronic topological transition (ETT) or Lifshitz transition.[10] While such phase transitions can be sampled by theoretical methods, characterizing these methods experimentally, particularly under high-pressure conditions, remains challenging. A variety of the probes used to characterize phase transitions at high pressure, including diffraction, vibrational spectroscopy, or using other characteristic thermodynamic properties, are either largely insensitive to or do not provide an atomic-level understanding of the underlying ETT process.[11] When available, angle-resolved photoemission spectroscopy (ARPES) is ideal for understanding electronic behavior;[12] unfortunately, ARPES remains inapplicable for high-pressure materials.

Several previous works have investigated the possible relationship between c/a anomalies and ETTs in Cd at varying pressures;[6,13–15] however, c/a discontinuities can occur for reasons other than ETTs.[16,17] Although the electronic structure of Cd has been studied at low pressure,[18,19] these works do not provide direct quantifiable evidence of an ETT in Cd. Vibrational Raman spectroscopy is often used to investigate ETTs;[10,20–22] however, there are disagreements even with the same system as to whether a mode should harden, soften, or just change linewidth as the system experiences an ETT. Additionally, some systems may not display optical Raman modes due to their crystal structures.[9] The Fermi surface of Cd was directly measured via the de Haas-van Alphen effect under ambient conditions[23] and attempts were made for measurements up to 2 GPa;[24] however, the pressure calibration and hydrostaticity of the pressure transmitting media (PTM) used in the latter work obfuscate the certainty of an ETT. Resistance measurements,[25] magnetoresistance measurements,[26] and structural measurements using x-ray diffraction (XRD)[1,7,27] suffer from similar hydrostaticity concerns and only infer the presence of an ETT.

Here, we observe a connection between the electronic behavior as observed spectroscopically and the projection of the calculated core-valence exciton density onto the

electronic band structure, suggesting and describing an ETT in Cd below 1 GPa. This work further validates the technique of using x-ray absorption spectroscopy (XAS) to explore ETTs at high pressure[28] and, when paired with the computational results, gives new insights into the mechanism of ETTs under pressure. Structural data as determined by XRD is shown and compared with the spectroscopic data to separate electronic and structural effects. No XAS discontinuities are observed after the ETT, indicating that in the range studied, there are no further ETTs.

3.2 Methods

The absorption length of the Cd K-edge was calculated in Hephaestus to be 23 μm. Cd (99.999%, Sigma-Aldrich) samples were cut from wire to match the calculated absorption length, as commercially available Cd powder samples with the appropriate mesh size could not be sourced at the time of this work. All samples were handled in an inert argon (Ar) environment prior to and during loading. Samples were at no point exposed to ambient air conditions, and a lack of reaction with air was verified with Raman for surface effects and XRD for bulk effects. No oxidation effects were seen by XAS, Raman, or XRD. Ruby fluorescence was used as the primary pressure marker,[29] with gold (Au) also loaded for use as an XRD pressure marker.[30] Ruby and Au had average dimensions of 15×15 μm (length×width) and were arranged to be out of the absorption path of Cd. Using an in-house-designed diamond anvil cell (DAC), samples were gas loaded with helium (He) in a premachined beryllium (Be) gasket, preindented to a thickness of about 23 μm. Samples were monitored via x-ray imaging to check for bridging between the diamonds and found to not be bridging (**Fig. C.5**). XRD and XAS experiments were carried out at 16-BMD, Sector 16 of the Advanced Photon Source.[31] XRD measurements (λ = 0.4132 Å) used axial geometry, while XAS measurements were taken in radial geometry through the x-ray transparent Be gasket on the Cd K-edge (26.7112 keV). The incoming x-ray beam size was around 4 μm at full width at half maximum, and the full width at about 1% of maximum is around 20 μm (**Fig. C.1**). Due to focusing methods,[32] there are no practical effects of a higher harmonic on the current measurement (see **Appendix C** for further discussion).

Since the sample itself is pure elemental Cd, the lowest pressure sample (loaded inertly at ambient pressure in an Ar environment) is collected as the internally consistent reference for energy calibration and referred to as the energy standard loadings within this work. Energy scans were made repeatedly to improve counting statistics. The scans were reproducible within 0.1–0.5 eV deviation, depending on the number of repetitions applied for each measurement. While the source of deviation is, strictly speaking, unknown, it is suspected to be due to heat accumulation on the monochromator motor and a slight offset in the calibration parameter due to a thermal expansion of mechanical parts. The energy calibration scheme for 16-BMD, Sector 16 of the Advanced Photon Source can be found in the work of Park *et al*.[31]

Raw XAS data, primarily x-ray absorption near edge structure (XANES), were reduced using the Athena software. Extended x-ray absorption fine structure (EXAFS) data were fit using the Artemis software package, and further analysis details of EXAFS data can be found in **Appendix C**. Ruby spectra were fit using Fityk for the central wavelength position which was used to calculate pressure[29]. XRD data were processed in Dioptas[32] and GSASII[33]. A La Bail refinement was carried out on each data point to extract lattice parameters. Au was fitted to the equation of state of Takemura and Dewaele[30] to compare to Ruby fluorescence measurements and was found to be in good agreement.

K-edge XAS calculations on Cd were performed with density functional theory (DFT) using the Bethe-Salpeter equation (BSE) as implemented in the OCEAN code[34–36] as a function of pressure with optimized structures every 0.5 GPa between 0 and 5 GPa. The Perdew-Burke-Ernzerhof (PBE) functional as implemented in the Quantum Espresso package was used with an energy cutoff of 2450 eV (180 Ry) for the DFT portion of the calculation[37–39]. The self-consistent field (SCF) calculation was done on a 10×10×10 k grid while the screening calculation was done on a 2×2×2 k grid. The pseudopotentials have a valency of $4s^2\,4p^6\,4d^{10}\,5s^2$.[40] The maximum energy for bands in the final state wave function was set to 150 eV above the edge. Lorentzian broadening was set to 7.32 eV to better match experimental data.[41] This formalism allows for using the experimentally determined crystallographic

orientation of the sample obtained from XRD to be applied to XAS calculations. The same computational input parameters for the K-edge XAS calculations are used with the generalized minimal residual (GMRES) method[42] (rather than the Haydock recursion method) to solve the BSE and calculate the real-space excitonic wavefunction. Ambient temperature Raman measurements as a function of pressure are also presented. Steel and rhenium (Re) gaskets are used with a lithium fluoride (LiF) PTM. $Sm:SrB_4O_7$ is used as a pressure marker for its temperature independence.[43,44] A 532 nm excitation line is used with matching Optigrate filters. Further DAC specification followed the methods of Hinton *et al*.[45]

3.3 Results and Discussion

Previous calculations suggested an ETT in Cd at varying pressures depending on the details of the method.[6,13,14,46] In our calculations probing for low pressure ETTs, distinct changes are observed in the band structure and in the topology of the Fermi surface between 0 and 0.5 GPa, particularly along the Γ–M, H–K, and H–L high symmetry paths in the first Brillouin zone. Between Γ and M, the peak of one band initially below the Fermi energy rises above it as the pressure is increased from 0 to 0.5 GPa (**Fig. 3.1(a)**). Across the same symmetry M–K path, a connection is formed in the sixfold symmetric corner features of the Fermi surface (**Figs. 3.1(b)** and **3.1(c)**). Along H–K, a surface that is connected at 0 GPa becomes disconnected at 0.5 GPa (**Figs. 3.1(b)** and **3.1(c)**), and we observe a band crossing the Fermi energy along this same symmetry path (**Fig. 3.1(a)**). Along H–L, a new surface appears in the Fermi surface (**Figs. 3.1(b)** and **3.1(c)**), and this corresponds to another band rising above the Fermi energy in **Fig. 3.1(a)**.

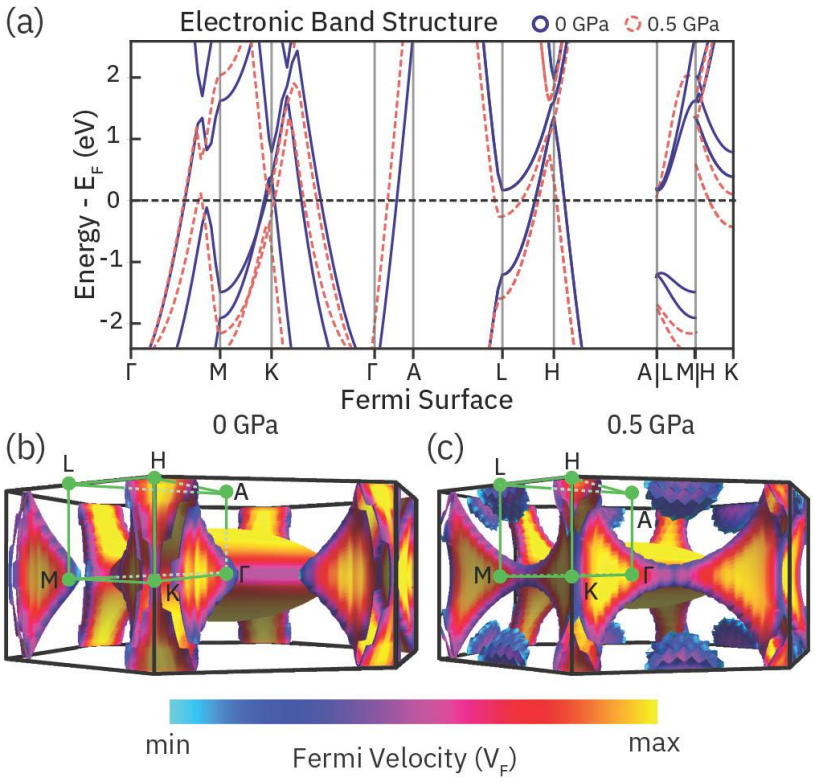

Figure 3.1. Computational evidence for ETT between 0 and 1 GPa. (a) Electronic band structure of Cd for 0 GPa (solid blue) and 0.5 GPa (dashed orange). **(b-c)** The Fermi surface of Cd in the first Brillouin zone, with high symmetry points marked in green: **(b)** 0 GPa, and **(c)** 0.5 GPa. Note the qualitative change in the Fermi surface between 0 and 0.5 GPa. Plotted with Fermisurfer software.[47]

The changes described lead to the formation of a new hole in the manifold, which represents a discontinuous change in the topology between 0 and 0.5 GPa. A new feature in the Fermi surface is also found with increasing pressure that occurs between the A and L points. These effects continue to increase in magnitude with increasing pressure, and the manifold connection grows throughout the Brillouin zone parallel to M–K as the pressure rises from 0.5 to 5 GPa. Despite these electronic changes at the Fermi energy, the total and partial densities of states show minimal changes as the ETT is crossed (**Figs. C.19** and **C.20**). These

computational observations suggest an ETT between 0 and 1 GPa, and no other ETT is predicted to occur up to 10 GPa.

To experimentally explore the predicted ETT, we first turn to XRD. Diffraction is widely used for observing phase transitions; however, it is largely insensitive to ETTs that do not correspond with significant first or second-order atomic structure changes. Here, the high-pressure diffraction is performed using a He PTM, the highest degree of hydrostaticity possible to compare to previous studies. Strong preferred orientation leading to poor powder averaging is observed across multiple samples (**Figs. C.6**–**C.8**). Structural exploration revealed that previously observed anomalies in the c/a ratio with volume at about 12 GPa (or around $V/V_0 = 0.85$)[1,7,27] are not observed when a hydrostatic PTM, He, is used (**Fig. 3.2(a)**). No further structural discontinuities are observed in the c/a ratio experimental data. Although calculated volumes predict discontinuities in c/a between 0–1 and 2–3 GPa, no further structural discontinuities are observed in the c/a ratio experimental data.

A change in slope in the pressure derivative of the bulk modulus is observed in the F-f plot (**Fig. 3.2(b)**) corresponding to approximately 3 GPa. The change in slope suggests a second-order phase transition. No discontinuities to the Fermi surface or electronic band structure are observed in correlation with this second-order structural transition. While a change in slope cannot be ruled out between 0–1 GPa in the F-f plot, the lack of experimental data in this range and the fact that F-f plots cannot use points at 0 GPa prevent a definitive conclusion; therefore, we cannot assign the lowest data point alone as a slope change, since this being an outlier is a possibility. Our limited EXAFS data also shows no structural anomaly, supporting no structural phase transition below 1 GPa (**Fig. C.12**).

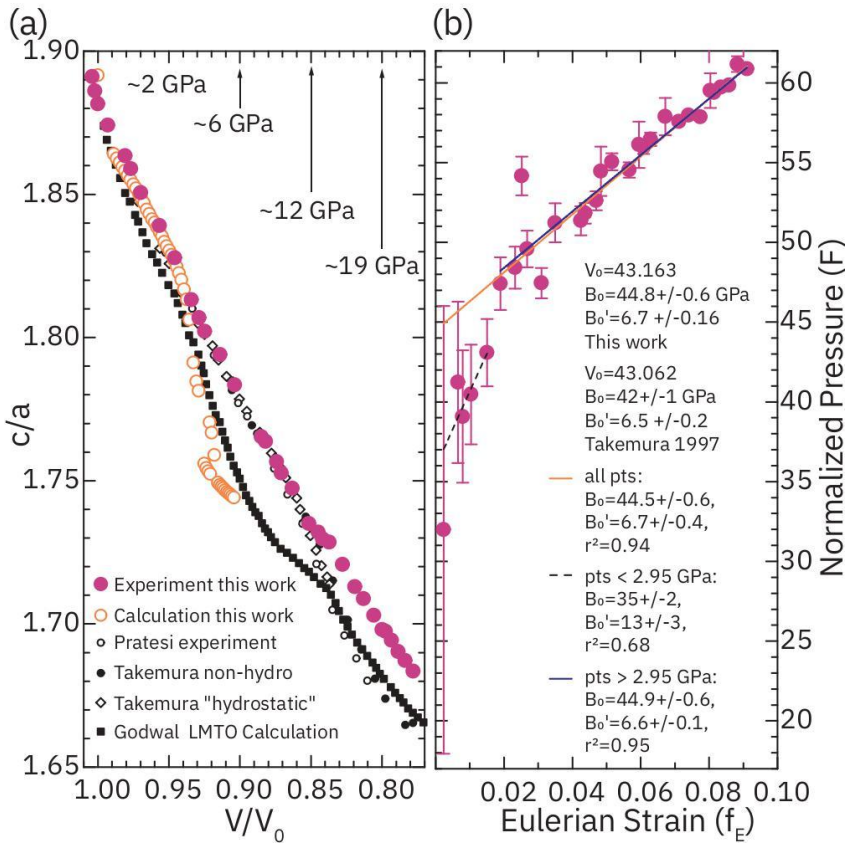

Figure 3.2. Structural information for Cd obtained via XRD from 0 to 25 GPa. (a) c/a vs V/V_0 plot with experimental (closed pink circles) and computational data (open orange circles) from this work plotted over literature data of Pratesi *et al.*[27] (black open circles), Takemura[1] (black closed circles and black open diamonds), and Godwal *et al.*[13] (black closed squares). Errors for the experimental points are less than the diameter of the points shown. **(b)** Normalized pressure (F) vs Eulerian strain (f_E) plot from XRD where $F = P[3 f_E (1 + 2 f_E)^{5/2}] - 1$ and $f_E = (1/2)[(V_0/V)^{2/3} - 1]$. Linear fits of the data are shown for above and below 2.95 GPa, and for the full data set.

The room temperature responses of the Raman active E_{2g} phonon mode of Cd frequency, linewidth, and intensity are shown in **Figs. C.26–C.35** and **Table C.III** for pressures from 0–10 GPa. Data points were collected from compression, decompression, as well as for samples that were previously heated to above the melting temperature. The calculated zone-

centered Raman frequencies, electron-phonon couplings, and phonon linewidths across the predicted 0.5 GPa ETT are given in **Table C.IV**. Further details and values of experimental frequency versus pressure and zone center phonon calculations are available in **Appendix C**. Our experimental Raman data do not show clear discontinuities about the ETTs in the aggregate for frequency, linewidth, or intensity. Additionally, our calculated values do not indicate discontinuities in the frequency, linewidth, or electron-phonon couplings. Taken together, this indicates that neither structural probe, diffraction, nor vibrational Raman, were effective probes for identifying this ETT in Cd. Although it is still possible (and common) to investigate ETTs by both structural methods, our dataset for Cd makes a good case study for systems where these methods will not work based on the fundamental properties of the material. For example, it is possible for a material to have no Raman modes allowed or experience an isostructural electronic change; in this case neither probe would be able to indicate a change.

Although these structural probes did not provide conclusive evidence correlating to the ETT observed in calculations, XAS can also be used to investigate the presence of an ETT as it relates directly to the electronic behavior. XAS can be broken into two regions: the XANES region and EXAFS region. EXAFS uses high energy scattering states to probe local atomic structure (or short-range order) through scattering. The near edge is an indicator of electronic behavior—XAS at the K-edge excites the 1*s* core electron to states above the Fermi energy. By projection of the calculated core-valence excitonic wavefunction onto the electron band structure, we can infer the *p*-orbital character of the band. Since the XAS process involves forcing a core electron into an unoccupied state above the Fermi surface, examining the XANES regions provides information pertaining to the electronic behaviors of the predicted ETT.

Figure 3.3 gives the experimental and calculated XANES from 0 to 5 GPa, with the experiment represented in dashed lines vertically offset above the calculations in solid lines. The spectra at 0 GPa, obtained from the energy standard DAC, are black and the higher pressures are in color as indicated by the legend. The experimental XAS show a

discontinuous change between 0 and 0.8 GPa indicated by the shift between 0 GPa and the higher-pressure lines 0.8–4.5 GPa. Above 0.8 GPa, the changes are more gradual. The spectra shown in **Fig. 3.3** are from one Cd sample (called sample 2 in **Appendix C**). We observe a similar shift in another sample (sample 3 in **Appendix C**). Sample 3 had been pressure-cycled and thus, some hysteresis in the energy shift is observed. The behavior of sample 3 suggests that the ETT observed in sample 2 is reproducible. Further data and details are available in **Appendix C**.

Theoretically calculated spectra are presented from 0.5–5.0 GPa in 0.5 GPa resolution. In addition to the energy offset applied to the calculated spectra, a scaling factor of about 16% is applied to the energy to account for the well-known DFT error of underestimating the band gap.[48] The same background correction used in the experiment is applied to the calculated spectra to account for the gradually dropping oscillator strength inherent to the calculation. Both of the above changes are for ease of visual comparison. See **Appendix C** for a comparison between experimental and calculated spectra that have not had scaling or background subtractions.

Our simulations show a large discontinuous change between 0 and 0.5 GPa, followed by a gradual change above 0.5 GPa. Theoretical calculations here consider both the orientation of the sample and the polarization of incident light orientation. Since Cd is hexagonal, the contributions from the *a* and *b* planes will be equal to each other while the *c* plane is different. This can be accounted for in the crystal orientation tensor and is most visible in the third XANES peak. The third peak will be asymmetric if the contribution from only one plane is considered, and the asymmetry shifts depending on which plane is considered. The asymmetry observed in the third peak is more obvious in the experiment than in theory. **Figure 3.3** shows that the third XANES peak of the experimental spectra is asymmetrical to the right, while the third XANES peak of the theoretically calculated spectra seems to show more of a doublet. This difference is likely due to the sample's intense preferred orientation, which is common for a sample sourced from wire. XRD patterns demonstrating different samples' preferred orientation are in **Appendix C**. Both experiment and theory see the peak

at ~26740 eV move higher in energy with increasing pressure, even when considering preferred orientation, suggesting the electronic structure is well captured by the theory.

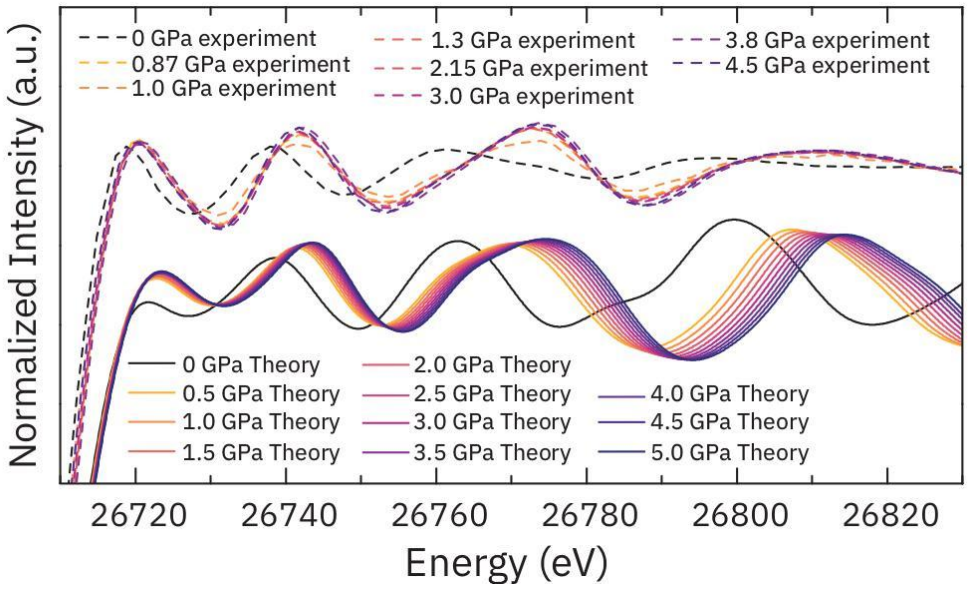

Figure 3.3. Calculated and experimental XANES spectra collected for Cd between 0 and 5 GPa (dashed lines show experimental observations). The 0 GPa point is from the energy standard, and the subsequent points are from sample 2. The large shift between the black lines at 0 GPa and the color lines at pressure is consistent with an electronic change occurring. Solid lines are calculated XANES spectra using OCEAN; the same energetic shift and scaling factor are applied to each calculated spectrum. Points have 0.5 GPa resolution. The same large peaks at approximately 26720, 26740, and 26775 eV, as well as the blue shift as a function of pressure are seen in both experiment and theory. See text and **Appendix C** for normalization and alignment details.

To explore the electronic nature of this change in the Cd XANES data further, the x-ray core-valence exciton distributions are projected onto the electronic band structure. To accomplish this, the core-valence exciton wavefunction at energy ω is defined using the two-particle Green's function and photon operator $\hat{T}$ acting on the ground state $|\Phi_0\rangle$:

$$|\Phi(\omega)\rangle = \frac{1}{\omega - H_{BSE} + \mathrm{i}\eta}\hat{T}|\Phi_0\rangle. \quad (3.1)$$

Here, the two-particle Green's function is defined as $G_2(\omega) = (\omega - H_{BSE} + \mathrm{i}\eta)^{-1}$ with the BSE Hamiltonian H_{BSE} and broadening parameter η, and the GMRES method is used to solve

$$(\omega - H_{BSE} + \mathrm{i}\eta) = \hat{T}|\Phi_0\rangle \quad (3.2)$$

for $|\Phi(\omega)\rangle$. With $|\Phi(\omega)\rangle$, it is possible to know which bands contribute to a peak in the spectrum, as the exciton wavefunctions having a hole at core level α and electrons in the band index n with momentum $\mathbf{k}$ are expressed as coefficients $C_{\mathrm{nk}\alpha}$ and Bloch states $|\mathrm{n}\mathbf{k}\rangle = e^{i\mathbf{k}\cdot\mathbf{r}}u_{\mathrm{nk}}(\mathbf{r})$:[34]

$$|\Phi(\omega)\rangle = \sum_{\mathrm{nk}\alpha} C_{\mathrm{nk}\alpha} e^{\mathrm{i}\mathbf{k}\cdot\mathbf{r}} u_{\mathrm{nk}}(\mathbf{r}) \quad (3.3)$$

The core-valence exciton wavefunctions are then projected onto the bands in reciprocal space to understand what transitions the XANES spectrum represents or the imaginary part of the dielectric function $\epsilon_2(\omega)$, in terms of each band n and k point:[49]

$$\epsilon_2(\omega) = \langle\Phi(\omega)|\Phi(\omega)\rangle = \langle\Phi(\omega)|(\textstyle\sum_{\mathrm{nk}}|\mathrm{n}\mathbf{k}\rangle\langle\mathrm{n}\mathbf{k}|)|\Phi(\omega)\rangle = \sum_{\mathrm{nk}}|\langle\mathrm{n}\mathbf{k}|\Phi(\omega)\rangle|^2 \quad (3.4)$$

This above projection is interpolated along high-symmetry lines since the k points for the GMRES calculation are on a Monkhorst-Pack grid.

This approach has been previously used to understand the physical origins of extreme ultraviolet photoexcited-state spectra.[50,51] Here, the same approach is used for the first time to bridge the electronic changes in reciprocal space (**Fig. 3.1**) with the spectral changes in XANES (**Fig. 3.3**). As the technique allows for a detailed understanding of the cause of measured x-ray absorption spectra, it can be used to show the underlying causes of experimental changes, i.e., an ETT.

Figure 3.4 shows the core-valence exciton density projected onto the Cd band structure for the first and second XAS peaks around 26720 and 26740 eV, respectively, at three different pressures (0, 0.5, and 2.0 GPa). The size and color of the dots in the figure refer to the amplitude of the core-valence transition at that point in reciprocal space. For the first peak, only slight differences in the transition amplitudes are calculated between 0 and 0.5 GPa. The change in transition amplitudes is primarily along the Γ–A, Γ–M, and Γ–K paths with smaller changes in the A–L and L–M pathways. Transition amplitudes increase as the point is approached in each case and new transitions become possible at energies closer to the Fermi level. Theoretically, this leads to an energy shift and shape change in the XAS spectra after the ETT.

For the second peak in **Fig. 3.3** at ~26740 eV, a more prominent and discontinuous spectral shift in the experimental and calculated XANES spectra is observed. In **Fig. 3.4**, excitons projected onto the band structure at 0.5 and 2.0 GPa show changes throughout reciprocal space when compared to 0 GPa. Specifically, transitions around 30 eV above the Fermi energy between the Γ and A points are more pronounced at 0 GPa than at higher pressures. The most intense transition is located near the K point at 0.5 and 2.0 GPa whereas it is located around the Γ point at 0 GPa. These changes should lead to a more blue-shifted peak with a longer tail, consistent with **Fig. 3.3** and are strongly indicative of a phase transition.

Figure 3.4 in combination with the experiment therefore confirms that the changes in the band structure from the ETT, as calculated in **Fig. 3.1**, are probed by XANES spectral changes. For Cd, the projected transition amplitudes also suggest a more *p*-orbital character after the ETT, given the dipole selection rules in XAS.

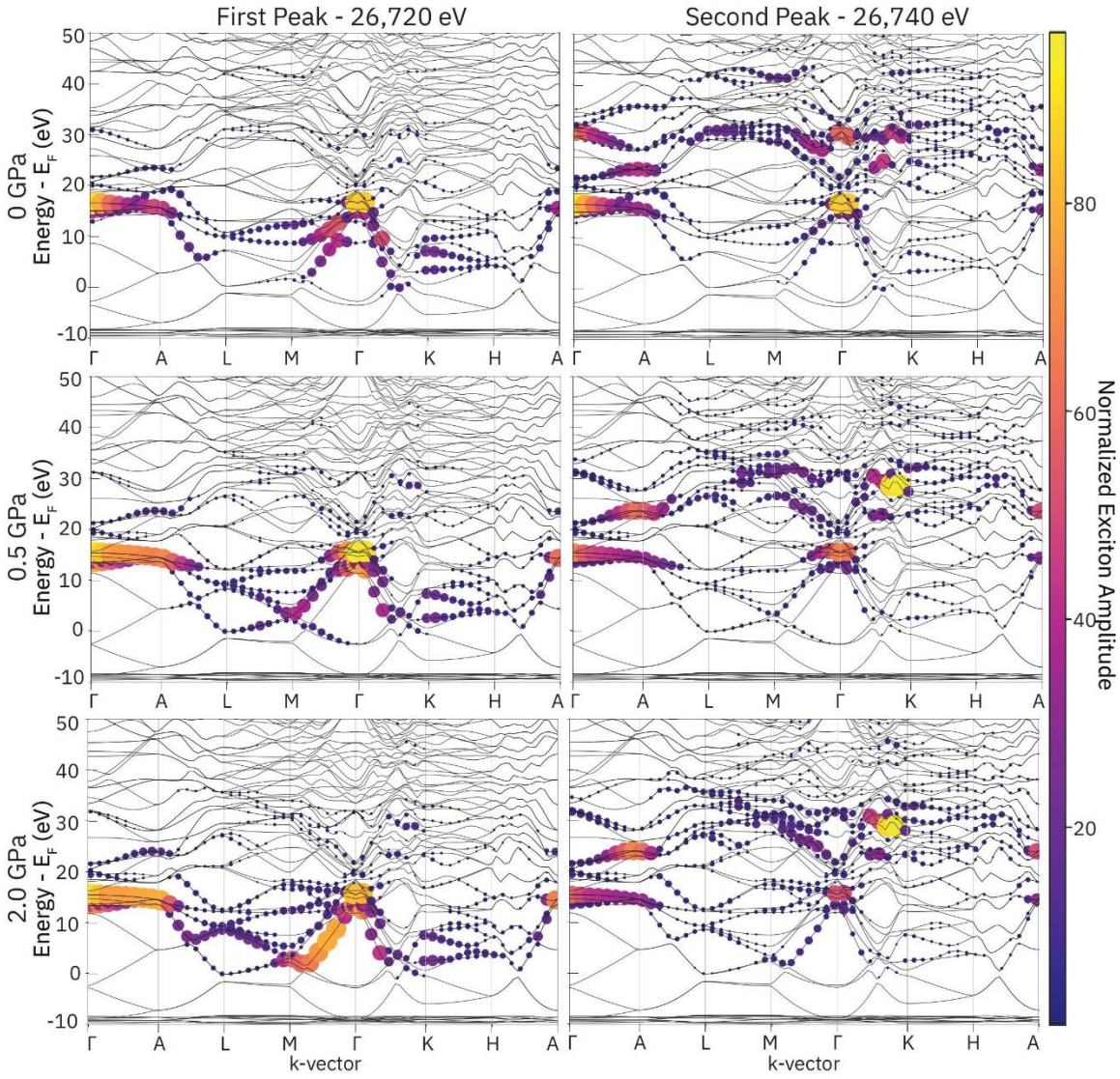

Figure 3.4. Core-valence exciton projection on band structure for first and second peaks (~26720 and 26740 eV) at 0, 0.5, and 2 GPa. The sizes and colors of the circles indicate the strength of the projected amplitude, with indigo indicating a relatively small transition and yellow indicating a large projection. The first peak projections show changes in transition amplitudes between 0 and 0.5 GPa along the Γ–A, Γ–M, and Γ–K paths with smaller changes in the A–L and L–M pathways. The second peak projections show changes throughout reciprocal space in the same pressure range. Notably, the most intense transition is located around the Γ point at 0 GPa and then becomes the K point at 0.5 and 2.0 GPa.

These amplitude changes, along with the others described in the text, provide strong evidence for the ETT in Cd.

3.4 Conclusions

While diffraction remains a powerful tool for the study of most phase transitions, we show that for Cd, it is largely insensitive to ETTs. In order to explore this, experimental spectroscopic measurements of Cd XAS between 0 and 5 GPa were taken. The case study on Cd shown here, including experimental and computational XANES data combined with band structure projections, provides and establishes a protocol for future works. Other disputed systems[4,5,16,17] can be revisited or new systems can be explored since this technique is available at pressures up to hundreds of GPa and for a wide variety of materials.[52] Based on all of our experimental and computational results, our data indicates the presence of an ETT in elemental Cd below 1 GPa. A second transition at a higher pressure is also observed, which is solely structural and second order in nature. We note that this technique is quite general and can be applied to a wide variety of experimental systems. Indeed, by taking advantage of the possibility of performing x-ray Raman spectroscopy in the cases where XAS will not work, almost all materials should be accessible.[53] This has wide implications in the field of static high-pressure research.

3.5 References

(1) Takemura, K. Structural Study of Zn and Cd to Ultrahigh Pressures. *Phys. Rev. B* **1997**, *56* (9), 5170–5179.

(2) Takemura, K. The Zinc Story under High Pressure. *Jr. Miner. Mater. Charact. Eng.* **2019**, *7* (5), 354–372.

(3) Novikov, D. L.; Freeman, A. J.; Christensen, N. E.; Svane, A.; Rodriguez, C. O. LDA Simulations of Pressure-Induced Anomalies in c/a and Electric-Field Gradients for Zn and Cd. *Phys. Rev. B* **1997**, *56* (12), 7206–7214.

(4) Takemura, K. Zn under Pressure: A Singularity in the hcp Structure at c/a = √3. *Phys. Rev. Lett.* **1995**, *75* (9), 1807–1810.

(5) Takemura, K. Absence of the c/a Anomaly in Zn under High Pressure with a Helium-Pressure Medium. *Phys. Rev. B* **1999**, *60* (9), 6171–6174.

(6) Godwal, B. K.; Meenakshi, S.; Rao, R. S.; Vijayakumar, V. Ca Anomalies, Thermoelectric Power and Electronic Topological Transitions in Cd. *J. Phys. Chem. Solids* **1998**, *59* (5), 747–751.

(7) Godwal, B. K.; Raju, S. V.; Geballe, Z.; Jeanloz, R. Electronic Phase Transitions in Cadmium at High Pressures. *J. Phys.: Conf. Ser.* **2012**, *377* (1), 012033.

(8) Dugdale, S. B. Life on the Edge: A Beginner's Guide to the Fermi Surface. *Phys. Scr.* **2016**, *91* (5), 053009.

(9) Zhang, Y.; Yang, C.; Alatas, A.; Said, A. H.; Salke, N. P.; Hong, J.; Lin, J.-F. Pressure Effect on Kohn Anomaly and Electronic Topological Transition in Single-Crystal Tantalum. *Phys. Rev. B* **2019**, *100* (7), 075145.

(10) Lifshitz, I. M. Anomalies of Electron Characteristics of a Metal in the High Pressure Region. *Sov. Phys. JETP* **1960**, *11* (5), 1130–1135.

(11) Beaulieu, S.; Dong, S.; Tancogne-Dejean, N.; Dendzik, M.; Pincelli, T.; Maklar, J.; Xian, R. P.; Sentef, M. A.; Wolf, M.; Rubio, A.; Rettig, L.; Ernstorfer, R. Ultrafast Dynamical Lifshitz Transition. *Sci. Adv.* **2021**, *7* (17), eabd9275.

(12) Zhang, Y.; Wang, C.; Yu, L.; Liu, G.; Liang, A.; Huang, J.; Nie, S.; Sun, X.; Zhang, Y.; Shen, B.; Liu, J.; Weng, H.; Zhao, L.; Chen, G.; Jia, X.; Hu, C.; Ding, Y.; Zhao, W.; Gao, Q.; Li, C.; He, S.; Zhao, L.; Zhang, F.; Zhang, S.; Yang, F.; Wang, Z.; Peng, Q.; Dai, X.; Fang, Z.; Xu, Z.; Chen, C.; Zhou, X. J. Electronic Evidence of

Temperature-Induced Lifshitz Transition and Topological Nature in $ZrTe_5$. *Nat. Commun.* **2017**, *8* (1), 15512.

(13) Godwal, B. K.; Meenakshi, S.; Rao, R. S. c/a Anomalies and Electronic Topological Transitions in Cd. *Phys. Rev. B* **1997**, *56* (23), 14871–14874.

(14) Novikov, D. L.; Katsnelson, M. I.; Trefilov, A. V.; Freeman, A. J.; Christensen, N. E.; Svane, A.; Rodriguez, C. O. Anisotropy of Thermal Expansion and Electronic Topological Transitions in Zn and Cd under Pressure. *Phys. Rev. B* **1999**, *59* (7), 4557–4560.

(15) Qiu, S. L.; Apostol, F.; Marcus, P. M. Structural Anomalies in hcp Metals under Pressure: Zn and Cd. *J. Phys.: Condens. Matter* **2004**, *16* (36), 6405.

(16) Dubrovinsky, L.; Dubrovinskaia, N.; Bykova, E.; Bykov, M.; Prakapenka, V.; Prescher, C.; Glazyrin, K.; Liermann, H.-P.; Hanfland, M.; Ekholm, M.; Feng, Q.; Pourovskii, L. V.; Katsnelson, M. I.; Wills, J. M.; Abrikosov, I. A. The Most Incompressible Metal Osmium at Static Pressures above 750 Gigapascals. *Nature* **2015**, *525* (7568), 226–229.

(17) Woolman, G. A.; Ackland, G. J. Detectability of Core-Level Crossing and Electronic Topological Transformations: The Case of Osmium. *Phys. Rev. B* **2022**, *106* (8), L081102.

(18) Blaha, P.; Schwarz, K.; Dederichs, P. H. Electronic Structure of hcp Metals. *Phys. Rev. B* **1988**, *38* (14), 9368–9374.

(19) Daniuk, S.; Jarlborg, T.; Kontrym-Sznajd, G.; Majsnerowski, J.; Stachowiak, H. Electronic Structure of Mg, Zn and Cd. *J. Phys.: Condens. Matter* **1989**, *1* (44), 8397.

(20) Pradhan, G. K.; Bera, A.; Kumar, P.; Muthu, D. V. S.; Sood, A. K. Raman Signatures of Pressure Induced Electronic Topological and Structural Transitions in Bi_2Te_3. *Solid State Commun.* **2012**, *152* (4), 284–287.

(21) Bera, A.; Pal, K.; Muthu, D. V. S.; Waghmare, U. V.; Sood, A. K. Pressure-Induced Phase Transition in Bi_2Se_3 at 3 GPa: Electronic Topological Transition or Not? *J. Phys.: Condens. Matter* **2016**, *28* (10), 105401.

(22) Zhang, A.; Ma, X.; Liu, C.; Lou, R.; Wang, Y.; Yu, Q.; Wang, Y.; Xia, T.; Wang, S.; Zhang, L.; Wang, X.; Chen, C.; Zhang, Q. Topological Phase Transition between Distinct Weyl Semimetal States in $MoTe_2$. *Phys. Rev. B* **2019**, *100* (20), 201107.

(23) Tsui, D. C.; Stark, R. W. De Haas-van Alphen Effect, Magnetic Breakdown, and the Fermi Surface of Cadmium. *Phys. Rev. Lett.* **1966**, *16* (1), 19–22.

(24) Bud'ko, S. L.; Voronovskii, A. N.; Gapotchenko, A. G.; ltskevich, E. S. The Fermi Surface of Cadmium at an Electron-Topological Phase Transition under Pressure. *Sov. Phys. JETP* **1984**, *59* (2), 454–457.

(25) Lynch, R. W.; Drickamer, H. G. The Effect of Pressure on the Resistance and Lattice Parameters of Cadmium and Zinc. *J. Phys. Chem. Solids* **1965**, *26* (1), 63–68.

(26) Itskevich, E. S.; Voronovskii, A. N. Change of Topology of the Fermi Surface of Cadmium under Pressure. *Sov. Phys. JETP Lett.* **1966**, *4* (6), 154–157.

(27) Pratesi, G.; Di Cicco, A.; Minicucci, M.; Itiè, J.-P. Anomalies in the Structure of Solid Cd under Pressure: An X-ray Diffraction Study. *J. Phys.: Condens. Matter* **2005**, *17* (17), 2625.

(28) Yamaoka, H.; Jeschke, H. O.; Yang, X.; He, T.; Goto, H.; Hiraoka, N.; Ishii, H.; Mizuki, J.; Kubozono, Y. Electronic Structures of Bi_2Se_3 and $Ag_xBi_2Se_3$ under Pressure Studied by High-Resolution X-ray Absorption Spectroscopy and Density Functional Theory Calculations. *Phys. Rev. B* **2020**, *102* (15), 155118.

(29) Shen, G.; Wang, Y.; Dewaele, A.; Wu, C.; Fratanduono, D. E.; Eggert, J.; Klotz, S.; Dziubek, K. F.; Loubeyre, P.; Fat'yanov, O. V.; Asimow, P. D.; Mashimo, T.;

Wentzcovitch, R. M. M. Toward an International Practical Pressure Scale: A Proposal for an IPPS Ruby Gauge (IPPS-Ruby2020). *High Pressure Res.* **2020**, *40* (3), 299–314.

(30) Takemura, K.; Dewaele, A. Isothermal Equation of State for Gold with a He-Pressure Medium. *Phys. Rev. B* **2008**, *78* (10), 104119.

(31) Park, C.; Popov, D.; Ikuta, D.; Lin, C.; Kenney-Benson, C.; Rod, E.; Bommannavar, A.; Shen, G. New Developments in Micro-X-ray Diffraction and X-ray Absorption Spectroscopy for High-Pressure Research at 16-BM-D at the Advanced Photon Source. *Rev. Sci. Instrum.* **2015**, *86* (7), 072205.

(32) Prescher, C.; Prakapenka, V. B. *DIOPTAS*: A Program for Reduction of Two-Dimensional X-ray Diffraction Data and Data Exploration. *High Pressure Res.* **2015**, *35* (3), 223–230.

(33) Toby, B. H.; Von Dreele, R. B. *GSAS-II*: The Genesis of a Modern Open-Source All Purpose Crystallography Software Package. *J. Appl. Cryst.* **2013**, *46* (2), 544–549.

(34) Vinson, J. Advances in the OCEAN-3 Spectroscopy Package. *Phys. Chem. Chem. Phys.* **2022**, *24* (21), 12787–12803.

(35) Vinson, J.; Rehr, J. J.; Kas, J. J.; Shirley, E. L. Bethe-Salpeter Equation Calculations of Core Excitation Spectra. *Phys. Rev. B* **2011**, *83* (11), 115106.

(36) Hamann, D. R. Optimized Norm-Conserving Vanderbilt Pseudopotentials. *Phys. Rev. B* **2013**, *88* (8), 085117.

(37) Perdew, J. P.; Burke, K.; Ernzerhof, M. Generalized Gradient Approximation Made Simple. *Phys. Rev. Lett.* **1996**, *77* (18), 3865–3868.

(38) Giannozzi, P.; Baroni, S.; Bonini, N.; Calandra, M.; Car, R.; Cavazzoni, C.; Ceresoli, D.; Chiarotti, G. L.; Cococcioni, M.; Dabo, I.; Corso, A. D.; Gironcoli, S. de; Fabris,

S.; Fratesi, G.; Gebauer, R.; Gerstmann, U.; Gougoussis, C.; Kokalj, A.; Lazzeri, M.; Martin-Samos, L.; Marzari, N.; Mauri, F.; Mazzarello, R.; Paolini, S.; Pasquarello, A.; Paulatto, L.; Sbraccia, C.; Scandolo, S.; Sclauzero, G.; Seitsonen, A. P.; Smogunov, A.; Umari, P.; Wentzcovitch, R. M. QUANTUM ESPRESSO: A Modular and Open-Source Software Project for Quantum Simulations of Materials. *J. Phys.: Condens. Matter* **2009**, *21* (39), 395502.

(39) Giannozzi, P.; Andreussi, O.; Brumme, T.; Bunau, O.; Nardelli, M. B.; Calandra, M.; Car, R.; Cavazzoni, C.; Ceresoli, D.; Cococcioni, M.; Colonna, N.; Carnimeo, I.; Corso, A. D.; Gironcoli, S. de; Delugas, P.; DiStasio, R. A.; Ferretti, A.; Floris, A.; Fratesi, G.; Fugallo, G.; Gebauer, R.; Gerstmann, U.; Giustino, F.; Gorni, T.; Jia, J.; Kawamura, M.; Ko, H.-Y.; Kokalj, A.; Küçükbenli, E.; Lazzeri, M.; Marsili, M.; Marzari, N.; Mauri, F.; Nguyen, N. L.; Nguyen, H.-V.; Otero-de-la-Roza, A.; Paulatto, L.; Poncé, S.; Rocca, D.; Sabatini, R.; Santra, B.; Schlipf, M.; Seitsonen, A. P.; Smogunov, A.; Timrov, I.; Thonhauser, T.; Umari, P.; Vast, N.; Wu, X.; Baroni, S. Advanced Capabilities for Materials Modelling with Quantum ESPRESSO. *J. Phys.: Condens. Matter* **2017**, *29* (46), 465901.

(40) van Setten, M. J.; Giantomassi, M.; Bousquet, E.; Verstraete, M. J.; Hamann, D. R.; Gonze, X.; Rignanese, G.-M. The PseudoDojo: Training and Grading a 85 Element Optimized Norm-Conserving Pseudopotential Table. *Comput. Phys. Commun.* **2018**, *226*, 39–54.

(41) Campbell, J. L.; Papp, T. Width of the Atomic *K–N*7 Levels. *At. Data Nucl. Data Tables* **2001**, *77* (1), 1–56.

(42) Saad, Y.; Schultz, M. H. GMRES: A Generalized Minimal Residual Algorithm for Solving Nonsymmetric Linear Systems. *SIAM J. Sci. and Stat. Comput.* **1986**, *7* (3), 856–869.

(43) Rashchenko, S. V.; Likhacheva, A. Yu.; Bekker, T. B. Preparation of a Macrocrystalline Pressure Calibrant $SrB_4O_7:Sm^{2+}$ Suitable for the H*P*-H*T* Powder Diffraction. *High Pressure Res.* **2013**, *33* (4), 720–724.

(44) Rashchenko, S. V.; Kurnosov, A.; Dubrovinsky, L.; Litasov, K. D. Revised Calibration of the $Sm:SrB_4O_7$ Pressure Sensor Using the Sm-Doped Yttrium-Aluminum Garnet Primary Pressure Scale. *J. Appl. Phys.* **2015**, *117* (14), 145902.

(45) Hinton, J. K.; Childs, C.; Smith, D.; Ellison, P. B.; Lawler, K. V.; Salamat, A. Response of the Mode Gruneisen Parameters with Anisotropic Compression: A Pressure and Temperature Dependent Raman Study of β-Sn. *Phys. Rev. B* **2020**, *102* (18), 184112.

(46) Srinivasan, V.; Godwal, B. K.; Grossman, J. C.; Jeanloz, R. Electronic Topological Transitions in Cd at High Pressures. arXiv:1511.01989.

(47) Kawamura, M. FermiSurfer: Fermi-Surface Viewer Providing Multiple Representation Schemes. *Comput. Phys. Commun.* **2019**, *239*, 197–203.

(48) Perdew, J. P. Density Functional Theory and the Band Gap Problem. *Int. J. Quantum Chem.* **1985**, *28* (S19), 497–523.

(49) Benedict, L. X.; Shirley, E. L. *Ab Initio* Calculation of $\varepsilon_2(\omega)$ Including the Electron-Hole Interaction: Application to GaN and CaF_2. *Phys. Rev. B* **1999**, *59* (8), 5441–5451.

(50) Klein, I. M.; Liu, H.; Nimlos, D.; Krotz, A.; Cushing, S. K. *Ab Initio* Prediction of Excited State and Polaron Effects in Transient XUV Measurements of α-Fe_2O_3. *J. Am. Chem. Soc.* **2022**, *144* (28), 12834–12841.

(51) Klein, I. M.; Krotz, A.; Lee, W.; Michelsen, J. M.; Cushing, S. K. *Ab Initio* Calculations of XUV Ground and Excited States for First-Row Transition Metal Oxides. *J. Phys. Chem. C* **2023**, *127* (2), 1077–1086.

(52) Purans, J.; Menushenkov, A. P.; Besedin, S. P.; Ivanov, A. A.; Minkov, V. S.; Pudza, I.; Kuzmin, A.; Klementiev, K. V.; Pascarelli, S.; Mathon, O.; Rosa, A. D.; Irifune, T.; Eremets, M. I. Local Electronic Structure Rearrangements and Strong Anharmonicity in YH_3 under Pressures up to 180 GPa. *Nat. Commun.* **2021**, *12* (1), 1765.

(53) Mizuno, Y.; Ohmura, Y. Theory of X-ray Raman Scattering. *J. Phys. Soc. Jpn.* **1967**, *22* (2), 445–449.

Chapter 4

RESONANT SELF-DIFFRACTION OF FEMTOSECOND EXTREME ULTRAVIOLET PULSES IN COBALT

Adapted with permission from the following:

Maznev, A. A.; Lee, W.; Cushing, S. K.; Angelis, D. D.; Fainozzi, D.; Foglia, L.; Gutt, C.; Jaouen, N.; Kammerbauer, F.; Masciovecchio, C.; Mincigrucci, R.; Nelson, K. A.; Paltanin, E.; Pelli-Cresi, J. S.; Polewczyk, V.; Ksenzov, D.; Bencivenga, F. Resonant Self-Diffraction of Femtosecond Extreme Ultraviolet Pulses in Cobalt. *In revision*, arXiv:2505.07168. https://doi.org/10.48550/arXiv.2505.07168.

4.1 Introduction

The advent of free electron lasers (FELs) enabled the expansion of nonlinear optical spectroscopy methods into extreme ultraviolet (EUV) and X-ray ranges.[1] In particular, four-wave mixing (FWM) techniques with EUV and EUV/optical fields are being actively developed.[2–5] Self-diffraction (SD) is the simplest non-collinear FWM process, in which the interference of two coherent beams crossed in the sample results in a spatially periodic excitation acting as a diffraction grating for the same beams. It is a well-known technique[6,7] widely used in nonlinear optical studies.[8–11] The SD geometry has also been used by theoreticians investigating nonlinear optical interactions in condensed matter.[12,13]

In the EUV range, a related FWM technique referred to as EUV transient grating (TG) spectroscopy has recently been developed at the FERMI FEL.[4,14] In the TG technique, a time-delayed probe pulse diffracts off a spatially periodic excitation produced by two time-coincident pump pulses crossed at the sample. SD of time-coincident pulses can be thought of as a degenerate version of a TG experiment at a zero pump-probe delay, where a pump beam serves as a zero-delay probe. The SD geometry has the advantage of simplicity, which

is important at short wavelengths where manipulating multiple noncollinear beams is significantly more difficult than in a conventional optical experiment.[15] Even more importantly, in the EUV TG experiments performed to date, the FEL wavelength could not be continuously tuned because of the narrow-band multilayer mirrors in the probe beam path. The SD approach overcomes this limitation, enabling studies in the vicinity of resonances, which has been identified by theoreticians as an especially promising application of FWM at short wavelengths.[16]

Here, we describe an EUV SD experiment on a thin cobalt (Co) film, with the photon energy scanned across the $M_{2,3}$ edge of Co. We observe a great enhancement of the SD efficiency at the resonant absorption edge and a fine structure above the edge. The results are compared with *ab initio* calculations using density functional theory (DFT) and the Bethe-Salpeter equation (BSE) based on the assumption that the electronic system is nearly thermalized within the FEL pulse duration.

4.2 Methods

The experiment was conducted at the TIMER beamline at FERMI and is schematically shown in **Fig. 4.1(a)**. Two 50 fs EUV pulses are obtained by bisecting the FEL output with a grazing incidence mirror. The beams are spatially and temporally overlapped at the sample, with a crossing angle of 2θ=18.4° (the bisector being normal to the sample surface) and a FWHM spot size of 300 μm. Each of the incident beams gives rise to two first order SD beams. One of the SD beams from pump A coincides with the transmitted pump B; the other SD beam goes into a background-free direction making an angle of $\psi = \arcsin(3\sin(\theta)) = 28.7°$ to the sample normal and is detected by a CCD camera. Note that for the background-free SD, the Bragg diffraction condition is not satisfied. However, the Bragg condition is relaxed for thin gratings. Based on the expression for TG diffraction efficiency in transmission in Ref. 17, we find that in our geometry the signal reduction due to the deviation from the Bragg condition is less than 4%. The sample was a 20-nm-thick Co film deposited by e-beam evaporation on a 30 nm silicon nitride membrane. The measurements were performed at room temperature in high vacuum.

The CCD camera images obtained by averaging over 250 FEL shots show a bright spot at the expected position of the SD signal, which only appears when the two pump beams are overlapped at the sample, see representative images in **Fig. 4.1(b)**. To quantify the SD signal, the CCD image is integrated within a region of interest chosen to include the entire SD spot.

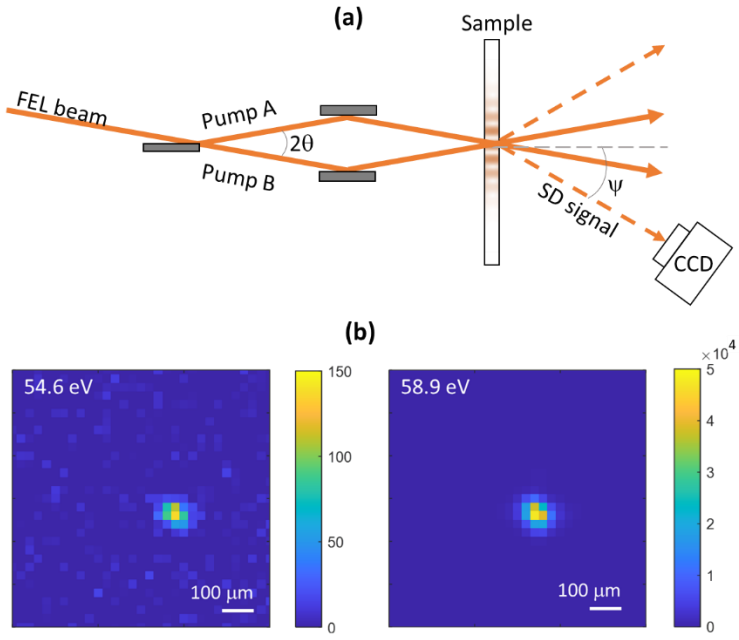

Figure 4.1. Experimental schematic and energy-dependent SD signal detection. (a) Schematic of the experiment. Dashed lines show background-free SD beams. **(b)** Images of the SD signal spot on the detector at photon energies corresponding to the smallest (54.6 eV) and largest (58.9 eV) SD signal. The color scale bars show CCD counts (note the substantial scale difference between the two images).

4.3 Results and Discussion

Figure 4.2(a) shows the dependence of the SD signal on the FEL photon energy ($h\nu$) in the range 54.6 – 72.1 eV (wavelengths 17.2 – 22.7 nm). For each value of $h\nu$, we obtained 3 – 8 images used to calculate the average value shown in **Fig. 4.2(a)** and the standard error shown as the error bars. The FEL pulse energy at the sample was ~1 μJ, with variations within a factor of two across the $h\nu$ scan. To compensate for the variations of the FEL

intensity, the signal is normalized by the cube of the FEL intensity in accordance with the expected intensity dependence of a FWM signal.

The most conspicuous feature in **Fig. 4.2(a)** is the sharp increase of the SD signal at the absorption edge. Between 54.6 eV and the peak at 58.8 eV, the increase is a factor of 500. Past the absorption edge, the SD signal decreases but remains higher than pre-edge. Furthermore, the SD spectrum above the edge exhibits a fine structure involving a shoulder at ~61 eV, a dip at 62.5 eV, and a peak at 64 eV. This fine structure is not present in the EUV absorption spectrum of Co.[18]

Figure. 4.2(b) shows the dependence of the SD signal on the FEL pulse energy at the sample at 59 eV, i.e., near the peak of the SD response, and confirms the cubic dependence mentioned above. At the high end of the intensity range, we had to use just a few FEL shots per image to avoid overloading of the detector, and the shutter did not provide sufficient accuracy for counting the number of shots, which explains the deviation of the data taken at high intensities from the cubic trend. Note that the dynamic range of this measurement amounted to 4 orders of magnitude and the signal level, on the high end, exceeded 5000 photons/shot.

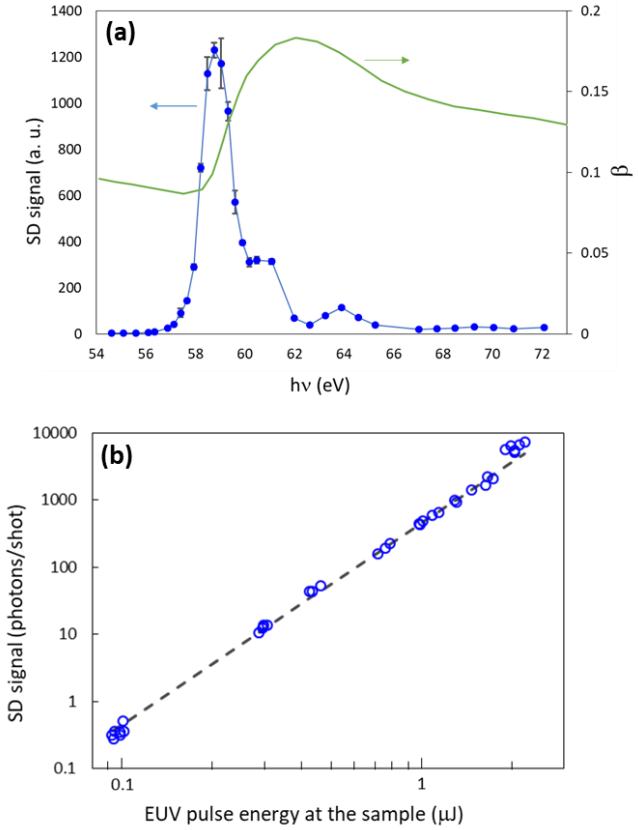

Figure 4.2. Photon energy and intensity dependence of the SD signal. (a) The dependence of the SD signal normalized by the cube of the FEL intensity on the photon energy (blue) and the spectrum of the imaginary part of the refractive index β adopted from Ref. 18 (green). Error bars reflect the standard error obtained from multiple measurements done at the same photon energy; where the error bars are not shown, they are smaller than the symbol size. **(b)** The dependence of the SD signal on the FEL intensity at the sample at $h\nu = 59$ eV (symbols). The dashed line shows a cubic dependence fit.

A natural question to ask is whether the observed resonant SD phenomenon is due to a coherent $\chi^{(3)}$ response involving the core hole and initially excited electron,[16] or whether it is caused by an incoherent population of excited electrons resulting from multi-step relaxation of the initial excitation.[19] The dephasing time of the M_2 and M_3 resonances in Co is estimated from the corresponding linewidths as ~3 fs,[20] which is much shorter than the FEL pulse

duration. While the short dephasing time does not preclude the presence of a coherent $\chi^{(3)}$ response, the latter seems inconsistent with a recently reported TG measurement with a variably delayed probe pulse on a similar sample with the pump and probe photon energy 59.6 eV, i.e., close to the peak of our SD spectrum.[17] In that experiment, the initial fast response was characterized by a short rise time comparable to the FEL pulse duration and a slower decay time of ~250 fs. Due to the short dephasing time, a coherent $\chi^{(3)}$ response would only exist while the pump and probe pulses overlapped, which is incompatible with the observed slow decay. As mentioned above, our SD measurement can be considered a degenerate version of TG experiment at the zero pump-probe delay. Consequently, we believe that our SD signal is more likely to be produced by an incoherent population of excited electrons than by a coherent $\chi^{(3)}$ response.

The simplest way to model the formation of the SD signal due to an incoherent electronic excitation is to assume that the electrons get thermalized faster than the FEL pulse duration. It was reported that electronic thermalization following optical excitation of Co occurs within 2 fs.[21] While thermalization of the excitation produced by ~60 eV EUV photons may take longer, we believe that assuming a thermalized electronic sub-system is a reasonable first step towards developing the theory of the observed phenomenon.

We calculate the variation of the complex refractive index at the EUV wavelength caused by an electronic temperature change using DFT and BSE.[22–25] The electronic temperature is implemented in the BSE Hamiltonian H^{BSE} by modifying the fractional occupation numbers[26–28]

$$H_{ij}^{BSE} = \epsilon_i \delta_{ij} + \sqrt{\tilde{f}_i}[V_X - W]\sqrt{\tilde{f}_j}. \tag{4.1}$$

In Eq. (4.1), the notation $i = \{vc\mathbf{k}\}$ represents the electron-hole pair indexes for each valence and conduction bands (v and c) and k-points ($\mathbf{k}$). The Hamiltonian includes the bare energies ϵ_i, the occupation number difference between the nominal electron (f_{ei}) and hole (f_{hi}) states $\tilde{f}_i = |f_{ei} - f_{hi}|$, and the two electron-hole interaction terms, the direct W and exchange V_X.

While the electron-hole correlation function in the BSE can be expanded into an infinite series, the first-order electron-hole interaction terms are only considered here. Additionally, the Tamm-Dancoff approximation is employed to simplify the calculations and make them computationally more efficient, while still providing reasonably accurate results for calculating the complex dielectric function.[29] The individual occupation numbers are given by the Fermi-Dirac distribution function $(E, \mu(T_e), T_e) = \{\exp[(E - \mu(T_e))/(k_B T_e)] + 1\}^{-1}$ where μ is the chemical potential, k_B is the Boltzmann constant, and T_e indicates the electron temperature. The chemical potential is determined using the electronic density of states in Co obtained from DFT (see **Appendix D** for further discussion). By solving the BSE via the Haydock recursion method, the complex dielectric function is derived from the photon operator $\hat{T}$ acting on the ground state $|\Phi_0\rangle$ and two-particle Green's function at energy ω defined as $G_2(\omega) = (\omega - H^{BSE} + i\eta)^{-1}$ with the BSE Hamiltonian and broadening parameter η,

$$\epsilon(\omega) = 1 - \frac{4\pi}{\Omega_V q^2}\left\langle \Phi_0 \middle| \hat{T}^\dagger \frac{1}{\omega - H^{BSE} + i\eta} \hat{T} \middle| \Phi_0 \right\rangle, \tag{4.2}$$

where Ω_V is the unit cell volume and q denotes the magnitude of the photon momentum.[24,30] The dielectric function is then converted into the complex refractive index: $\tilde{n} = 1 - \delta + \mathrm{i}\beta$.

The diffraction efficiency of a refractive index grating in a weakly absorbing material is proportional to $(\Delta\delta)^2 + (\Delta\beta)^2$, where $\Delta\delta$ and $\Delta\beta$ are the amplitudes of the modulation of the real and imaginary parts of the refractive index, respectively.[31] In our case, the material is strongly absorbing at the EUV wavelength, which leads to a more complicated expression for the diffraction efficiency.[17] Representing the refractive index variation as $(\Delta\delta)^2 + (\Delta\beta)^2 = A(h\nu)\rho^2$, where $A(h\nu)$ is a function of the photon energy and ρ is the absorbed energy density and using Eq. (5) from Ref. 17, we obtain the following expression for the normalized SD signal,

$$\frac{I_{SD}}{I_0^3} \propto A(h\nu)\frac{e^{-\frac{d}{L\cos\psi}}}{L^2}\,\frac{e^{-\frac{d}{L^*}} - 2e^{-\frac{d}{2L^*}}\cos(\Delta Q_z d) + 1}{\Delta Q_z^2 + \frac{1}{4L^{*2}}}, \tag{4.3}$$

where I_{SD} is the SD signal, I_0 is the pump pulse energy, d is the sample thickness, L is the absorption length at the EUV wavelength, $L^* = L(3/\cos\theta - 1/\cos\psi)^{-1}$, and $\Delta Q_z = k(\cos\theta - \cos\psi)$, where k is the EUV wave vector. (We only retained the terms dependent on the photon energy.) We calculate $A(h\nu)$ by computing $(\Delta\delta)^2 + (\Delta\beta)^2$ at a fixed electronic temperature rise of 100 K above a background temperature of 300 K (see **Appendix D** for further discussion) and take $L(h\nu)$ from Ref. 18. (As one can see from **Fig. D.4**, the variations of δ and β are comparable in magnitude.)

Figure 4.3 shows the calculated SD spectrum alongside the experimental data. The calculated SD spectrum reproduces a sharp peak at the Co $M_{2,3}$ edge and exhibits smaller peaks above the edge, qualitatively agreeing with experiment. At the Co $M_{2,3}$ edge, EUV photons excite core 3p electrons to unoccupied states near the Fermi level in the conduction band formed by 3d states. Changes in the electron temperature alter the electronic population near the Fermi level, as described by Fermi-Dirac statistics. When the final state of the transition lies at the Fermi level, the refractive index becomes highly sensitive to variations in the electronic temperature, which explains the intense SD peak. The interactions between electrons involved in the transition and screening processes lead to collective excitations above the Co $M_{2,3}$ edge.[32] This many-body effect is captured by using the screened Coulomb potential in the direct term (W) of the BSE Hamiltonian in Eq. (4.1). The transition probability is modified due to the changes in the electronic population and spectral changes resulting from the state-filling effect are therefore observed beyond the absorption edge. The fine structure above the edge is less accurately reproduced by our calculations, because the model used here is primarily designed for calculating the spectrum near an absorption edge and may not be as suitable for simulating the extended SD spectrum.

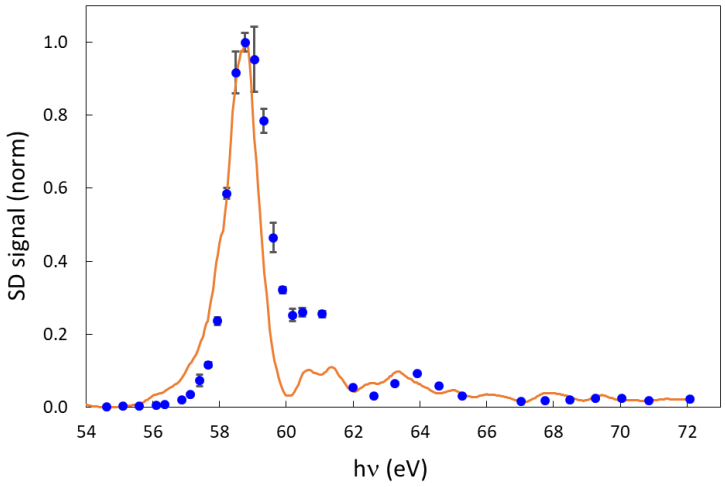

Figure 4.3. Calculated SD spectrum (solid curve), assuming the EUV excitation modulates the complex refractive index via electronic temperature, compared with experimental data (dots). Both the theoretical curve and experimental data are normalized to their respective maxima.

4.4 Conclusions and Outlook

While the present experiment provides a proof-of-principle for resonant EUV SD, further developments can be anticipated. Firstly, the fact that the M-edge resonance is much more prominent in the SD spectrum than in the absorption spectrum indicates the potential of the SD technique as a spectroscopy tool. We expect the fine structure in the SD spectrum to be specific to a particular chemical compound, which may lead to a nonlinear near-edge EUV spectroscopy technique based on SD. One can also envision looking for signatures of coherent FWM effects: for example, a photon echo can be detected in SD by introducing a delay between the two pulses.[33,34] Even though we believe that the coherent $\chi^{(3)}$ response is unlikely to tangibly contribute to the SD signal in the present experiment, one can use absorption edges of lighter elements with longer dephasing time[5] and shorter EUV pulses. Experiments with gas phase samples, where hundreds-fs dephasing times have been reported[35] may prove especially promising. Whereas the present experiment was conducted

at an FEL facility, the simplicity of the SD setup and large signal levels may enable "table-top" EUV FWM experiments with high-harmonic generation sources.[36]

In summary, we have demonstrated femtosecond SD in the EUV range. By scanning the photons energy across the $M_{2,3}$ edge of Co, we obtain an SD spectrum revealing a resonant peak at the absorption edge, and a fine structure above the edge. The SD spectrum is much more structured than the EUV absorption spectrum, which may yield a useful nonlinear EUV spectroscopy tool. While a model based on an incoherent mechanism in which the SD signal is produced by a modulation of the electronic temperature yields a reasonable agreement with the experiment, it is anticipated that SD can be used to study coherent FWM effects in the EUV and possibly X-ray ranges.

4.5 References

(1) Chergui, M.; Beye, M.; Mukamel, S.; Svetina, C.; Masciovecchio, C. Progress and Prospects in Nonlinear Extreme-Ultraviolet and X-ray Optics and Spectroscopy. *Nat. Rev. Phys.* **2023**, *5* (10), 578–596.

(2) Bencivenga, F.; Cucini, R.; Capotondi, F.; Battistoni, A.; Mincigrucci, R.; Giangrisostomi, E.; Gessini, A.; Manfredda, M.; Nikolov, I. P.; Pedersoli, E.; Principi, E.; Svetina, C.; Parisse, P.; Casolari, F.; Danailov, M. B.; Kiskinova, M.; Masciovecchio, C. Four-Wave Mixing Experiments with Extreme Ultraviolet Transient Gratings. *Nature* **2015**, *520* (7546), 205–208.

(3) Foglia, L.; Capotondi, F.; Mincigrucci, R.; Naumenko, D.; Pedersoli, E.; Simoncig, A.; Kurdi, G.; Calvi, A.; Manfredda, M.; Raimondi, L.; Mahne, N.; Zangrando, M.; Masciovecchio, C.; Bencivenga, F. First Evidence of Purely Extreme-Ultraviolet Four-Wave Mixing. *Phys. Rev. Lett.* **2018**, *120* (26), 263901.

(4) Bencivenga, F.; Mincigrucci, R.; Capotondi, F.; Foglia, L.; Naumenko, D.; Maznev, A. A.; Pedersoli, E.; Simoncig, A.; Caporaletti, F.; Chiloyan, V.; Cucini, R.; Dallari, F.; Duncan, R. A.; Frazer, T. D.; Gaio, G.; Gessini, A.; Giannessi, L.; Huberman, S.; Kapteyn, H.; Knobloch, J.; Kurdi, G.; Mahne, N.; Manfredda, M.; Martinelli, A.;

Murnane, M.; Principi, E.; Raimondi, L.; Spampinati, S.; Spezzani, C.; Trovò, M.; Zangrando, M.; Chen, G.; Monaco, G.; Nelson, K. A.; Masciovecchio, C. Nanoscale Transient Gratings Excited and Probed by Extreme Ultraviolet Femtosecond Pulses. *Sci. Adv.* **2019**, *5* (7), eaaw5805.

(5) Rottke, H.; Engel, R. Y.; Schick, D.; Schunck, J. O.; Miedema, P. S.; Borchert, M. C.; Kuhlmann, M.; Ekanayake, N.; Dziarzhytski, S.; Brenner, G.; Eichmann, U.; Von Korff Schmising, C.; Beye, M.; Eisebitt, S. Probing Electron and Hole Colocalization by Resonant Four-Wave Mixing Spectroscopy in the Extreme Ultraviolet. *Sci. Adv.* **2022**, *8* (20), eabn5127.

(6) Carman, R. L.; Chiao, R. Y.; Kelley, P. L. Observation of Degenerate Stimulated Four-Photon Interaction and Four-Wave Parametric Amplification. *Phys. Rev. Lett.* **1966**, *17* (26), 1281–1283.

(7) Vinetskiĭ, V. L.; Kukhtarev, N. V.; Odulov, S. G.; Soskin, M. S. Dynamic Self-Diffraction of Coherent Light Beams. *Sov. Phys. Usp.* **1979**, *22* (9), 742.

(8) Göbel, E. O.; Leo, K.; Damen, T. C.; Shah, J.; Schmitt-Rink, S.; Schäfer, W.; Müller, J. F.; Köhler, K. Quantum Beats of Excitons in Quantum Wells. *Phys. Rev. Lett.* **1990**, *64* (15), 1801–1804.

(9) Kner, P.; Schäfer, W.; Lövenich, R.; Chemla, D. S. Coherence of Four-Particle Correlations in Semiconductors. *Phys. Rev. Lett.* **1998**, *81* (24), 5386–5389.

(10) Kane, D. J.; Trebino, R. Characterization of Arbitrary Femtosecond Pulses Using Frequency-Resolved Optical Gating. *IEEE J. Quant. Electron.* **1993**, *29* (2), 571–579.

(11) Rappen, T.; Peter, U.; Wegener, M.; Schäfer, W. Coherent Dynamics of Continuum and Exciton States Studied by Spectrally Resolved Fs Four-Wave Mixing. *Phys. Rev. B* **1993**, *48* (7), 4879–4882.

(12) Lvovsky, A. I.; Hartmann, S. R. Superradiant Self-Diffraction. *Phys. Rev. A* **1999**, *59* (5), 4052–4057.

(13) Meier, T.; Chernyak, V.; Mukamel, S. Femtosecond Photon Echoes in Molecular Aggregates. *J. Chem. Phys.* **1997**, *107* (21), 8759–8780.

(14) Bencivenga, F.; Capotondi, F.; Foglia, L.; Mincigrucci, R.; Masciovecchio, C. Extreme Ultraviolet Transient Gratings. *Adv. Phys. X* **2023**, *8* (1), 2220363.

(15) Mincigrucci, R.; Foglia, L.; Naumenko, D.; Pedersoli, E.; Simoncig, A.; Cucini, R.; Gessini, A.; Kiskinova, M.; Kurdi, G.; Mahne, N.; Manfredda, M.; Nikolov, I. P.; Principi, E.; Raimondi, L.; Zangrando, M.; Masciovecchio, C.; Capotondi, F.; Bencivenga, F. Advances in Instrumentation for FEL-Based Four-Wave-Mixing Experiments. *Nucl. Instrum. Methods Phys. Res. Sect. A* **2018**, *907*, 132–148.

(16) Tanaka, S.; Mukamel, S. X-Ray Four-Wave Mixing in Molecules. *J. Chem. Phys.* **2002**, *116* (5), 1877–1891.

(17) Foglia, L.; Mincigrucci, R.; Maznev, A. A.; Baldi, G.; Capotondi, F.; Caporaletti, F.; Comin, R.; De Angelis, D.; Duncan, R. A.; Fainozzi, D.; Kurdi, G.; Li, J.; Martinelli, A.; Masciovecchio, C.; Monaco, G.; Milloch, A.; Nelson, K. A.; Occhialini, C. A.; Pancaldi, M.; Pedersoli, E.; Pelli-Cresi, J. S.; Simoncig, A.; Travasso, F.; Wehinger, B.; Zanatta, M.; Bencivenga, F. Extreme Ultraviolet Transient Gratings: A Tool for Nanoscale Photoacoustics. *Photoacoustics* **2023**, *29*, 100453.

(18) Saadeh, Q.; Naujok, P.; Thakare, D.; Wu, M.; Philipsen, V.; Scholze, F.; Buchholz, C.; Salami, Z.; Abdulhadi, Y.; García, D. O.; Mentzel, H.; Babuschkin, A.; Laubis, C.; Soltwisch, V. On the Optical Constants of Cobalt in the M-Absorption Edge Region. *Optik* **2023**, *273*, 170455.

(19) Medvedev, N.; Zastrau, U.; Förster, E.; Gericke, D. O.; Rethfeld, B. Short-Time Electron Dynamics in Aluminum Excited by Femtosecond Extreme Ultraviolet Radiation. *Phys. Rev. Lett.* **2011**, *107* (16), 165003.

(20) Campbell, J. L.; Papp, T. Widths of the Atomic *K–N*7 Levels. *At. Data Nucl. Data Tables* **2001**, *77* (1), 1–56.

(21) de Roulet, B. R.; Drescher, L.; Sato, S. A.; Leone, S. R. Initial Electron Thermalization in Metals Measured by Attosecond Transient Absorption Spectroscopy. *Phys. Rev. B* **2024**, *110* (17), 174301.

(22) Giannozzi, P.; Andreussi, O.; Brumme, T.; Bunau, O.; Nardelli, M. B.; Calandra, M.; Car, R.; Cavazzoni, C.; Ceresoli, D.; Cococcioni, M.; Colonna, N.; Carnimeo, I.; Corso, A. D.; Gironcoli, S. de; Delugas, P.; DiStasio, R. A.; Ferretti, A.; Floris, A.; Fratesi, G.; Fugallo, G.; Gebauer, R.; Gerstmann, U.; Giustino, F.; Gorni, T.; Jia, J.; Kawamura, M.; Ko, H.-Y.; Kokalj, A.; Küçükbenli, E.; Lazzeri, M.; Marsili, M.; Marzari, N.; Mauri, F.; Nguyen, N. L.; Nguyen, H.-V.; Otero-de-la-Roza, A.; Paulatto, L.; Poncé, S.; Rocca, D.; Sabatini, R.; Santra, B.; Schlipf, M.; Seitsonen, A. P.; Smogunov, A.; Timrov, I.; Thonhauser, T.; Umari, P.; Vast, N.; Wu, X.; Baroni, S. Advanced Capabilities for Materials Modelling with Quantum ESPRESSO. *J. Phys.: Condens. Matter* **2017**, *29* (46), 465901.

(23) Giannozzi, P.; Baroni, S.; Bonini, N.; Calandra, M.; Car, R.; Cavazzoni, C.; Ceresoli, D.; Chiarotti, G. L.; Cococcioni, M.; Dabo, I.; Corso, A. D.; Gironcoli, S. de; Fabris, S.; Fratesi, G.; Gebauer, R.; Gerstmann, U.; Gougoussis, C.; Kokalj, A.; Lazzeri, M.; Martin-Samos, L.; Marzari, N.; Mauri, F.; Mazzarello, R.; Paolini, S.; Pasquarello, A.; Paulatto, L.; Sbraccia, C.; Scandolo, S.; Sclauzero, G.; Seitsonen, A. P.; Smogunov, A.; Umari, P.; Wentzcovitch, R. M. QUANTUM ESPRESSO: A Modular and Open-Source Software Project for Quantum Simulations of Materials. *J. Phys.: Condens. Matter* **2009**, *21* (39), 395502.

(24) Vinson, J. Advances in the OCEAN-3 Spectroscopy Package. *Phys. Chem. Chem. Phys.* **2022**, *24* (21), 12787–12803.

(25) Vinson, J.; Rehr, J. J.; Kas, J. J.; Shirley, E. L. Bethe-Salpeter Equation Calculations of Core Excitation Spectra. *Phys. Rev. B* **2011**, *83* (11), 115106.

(26) Schleife, A.; Rödl, C.; Fuchs, F.; Hannewald, K.; Bechstedt, F. Optical Absorption in Degenerately Doped Semiconductors: Mott Transition or Mahan Excitons? *Phys. Rev. Lett.* **2011**, *107* (23), 236405.

(27) Sangalli, D.; Dal Conte, S.; Manzoni, C.; Cerullo, G.; Marini, A. Nonequilibrium Optical Properties in Semiconductors from First Principles: A Combined Theoretical and Experimental Study of Bulk Silicon. *Phys. Rev. B* **2016**, *93* (19), 195205.

(28) Klein, I. M.; Krotz, A.; Lee, W.; Michelsen, J. M.; Cushing, S. K. *Ab Initio* Calculations of XUV Ground and Excited States for First-Row Transition Metal Oxides. *J. Phys. Chem. C* **2023**, *127* (2), 1077–1086.

(29) Benedict, L. X.; Shirley, E. L.; Bohn, R. B. Optical Absorption of Insulators and the Electron-Hole Interaction: An *Ab Initio* Calculation. *Phys. Rev. Lett.* **1998**, *80* (20), 4514–4517.

(30) Benedict, L. X.; Shirley, E. L. *Ab Initio* Calculation of $\varepsilon_2(\omega)$ Including the Electron-Hole Interaction: Application to GaN and CaF_2. *Phys. Rev. B* **1999**, *59* (8), 5441–5451.

(31) Nelson, K. A.; Casalegno, R.; Miller, R. J. D.; Fayer, M. D. Laser-induced Excited State and Ultrasonic Wave Gratings: Amplitude and Phase Grating Contributions to Diffraction. *J. Chem. Phys.* **1982**, *77* (3), 1144–1152.

(32) Connerade, J. P. Controlled Collapse and the Profiles of 'Giant Resonances.' In *Giant Resonances in Atoms, Molecules, and Solids*; Connerade, J. P., Esteva, J. M., Karnatak, R. C., Eds.; Springer US: Boston, MA, 1987; pp 3–23.

(33) Abella, I. D.; Kurnit, N. A.; Hartmann, S. R. Photon Echoes. *Phys. Rev.* **1966**, *141* (1), 391–406.

(34) Bennhardt, D.; Thomas, P.; Eccleston, R.; Mayer, E. J.; Kuhl, J. Polarization Dependence of Four-Wave-Mixing Signals in Quantum Wells. *Phys. Rev. B* **1993**, *47* (20), 13485–13490.

(35) Wituschek, A.; Bruder, L.; Allaria, E.; Bangert, U.; Binz, M.; Borghes, R.; Callegari, C.; Cerullo, G.; Cinquegrana, P.; Giannessi, L.; Danailov, M.; Demidovich, A.; Di Fraia, M.; Drabbels, M.; Feifel, R.; Laarmann, T.; Michiels, R.; Mirian, N. S.; Mudrich, M.; Nikolov, I.; O'Shea, F. H.; Penco, G.; Piseri, P.; Plekan, O.; Prince, K. C.; Przystawik, A.; Ribič, P. R.; Sansone, G.; Sigalotti, P.; Spampinati, S.; Spezzani, C.; Squibb, R. J.; Stranges, S.; Uhl, D.; Stienkemeier, F. Tracking Attosecond Electronic Coherences Using Phase-Manipulated Extreme Ultraviolet Pulses. *Nat. Commun.* **2020**, *11* (1), 883.

(36) Makos, I.; Orfanos, I.; Nayak, A.; Peschel, J.; Major, B.; Liontos, I.; Skantzakis, E.; Papadakis, N.; Kalpouzos, C.; Dumergue, M.; Kühn, S.; Varju, K.; Johnsson, P.; L'Huillier, A.; Tzallas, P.; Charalambidis, D. A 10-Gigawatt Attosecond Source for Non-Linear XUV Optics and XUV-Pump-XUV-Probe Studies. *Sci. Rep.* **2020**, *10* (1), 3759.

Appendix A

TIME-RESOLVED CHEMICALLY-SELECTIVE SPECTROSCOPIC INVESTIGATION OF THE REDOX REACTION BETWEEN HEMATITE AND ALUMINUM

Adapted with permission from the following:

Paltanin, E.†; Pelli Cresi, J. S. †; Principi, E.; Lee, W.; Bencivenga, F.; De Angelis, D.; Foglia, L.; Garzella, D.; Kurdi, G.; Manfredda, M.; Naumenko, D.; Simoncig, A.; Cushing, S. K.; Mincigrucci, R.; Masciovecchio, C. Time-Resolved Chemically-Selective Spectroscopic Investigation of the Redox Reaction between Hematite and Aluminium. *Nat. Commun.* **2025**, *16* (1), 7282. https://doi.org/10.1038/s41467-025-62436-z.

A.1 Introduction

Redox reactions are fundamental chemical processes involved in many vital systems, such as cellular respiration and photosynthesis, as well as in combustion and fermentation. Electron transfer is the initial and fastest step of a redox reaction, typically occurring within hundreds of femtoseconds. The rapid redistribution of electrons initiates bond breaking and formation, followed by nuclear rearrangement on the picosecond timescale. Thermite reactions—redox processes between a metal and an oxide—are particularly exothermic and irreversible. They are widely used in welding, materials synthesis, propulsion and pyrotechnics. When at least one of the reactants is nanostructured, these systems are referred to as metastable intermolecular composites (MICs), which exhibit enhanced performance due to lower ignition thresholds and faster reaction kinetics enabled by increased surface contact.[1,2] The interest in MICs has led to studies using differential scanning calorimetry,[2]

X-ray diffraction,[3,4] Mössbauer spectroscopy,[3] mass spectrometry,[5] and photoemission spectroscopy,[6] under various ignition conditions including electrical discharge,[3] furnace heating,[4] and nanosecond pulsed lasers.[1,2,5]

These prior investigations focused on microsecond-to-second timescales, targeting slower steps like oxygen migration and complete product formation. In contrast, the ignition phase itself typically unfolds over nanoseconds or longer, requiring higher temporal resolution to be properly investigated. Ultrafast soft X-ray and extreme ultraviolet (EUV) spectroscopic techniques have been effectively applied to intramolecular photochemical reactions,[7,8] but chemically resolved studies of bimolecular reactions on the femtosecond scale remain absent. Time-resolved X-ray absorption spectroscopy (tr-XAS) at the Fe $M_{2,3}$ edge, sensitive to oxidation state changes in α-Fe_2O_3, has proven to be a powerful probe of ultrafast dynamics.[9,10]

In this work, we investigate the redox reaction between aluminum and hematite using femtosecond EUV transient absorption spectroscopy. By initiating the process with an ultrashort optical pulse and probing the dynamics at the Fe $M_{2,3}$ and Al $L_{2,3}$ absorption edges, we track early electron transfer events with chemical selectivity (**Fig. A.1**). This approach enables the first femtosecond-resolved, element-specific observation of a bimolecular redox reaction involving a thermite system at the nanoscale.

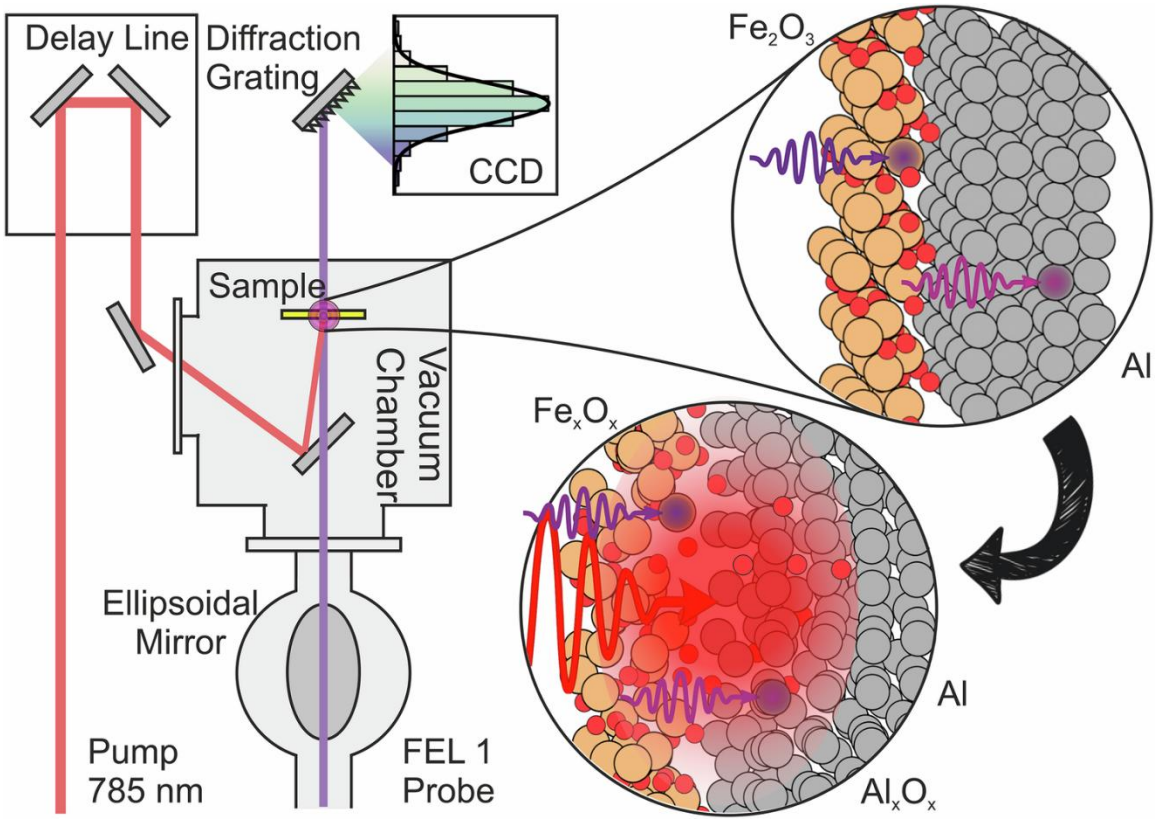

Figure A.1. Sketch of the experimental layout. The red line represents the path of the visible pump laser, which is delivered in the experimental chamber (in high vacuum) from the femtosecond laser facility of FERMI and it is focused on the sample using a lens. The free electron laser (FEL) radiation is employed to probe the dynamics at the Fe $M_{2,3}$ and Al $L_{2,3}$ absorption edges and it is illustrated by the violet line. It is delivered to the sample chamber via the beam transport vacuum pipes and it is focused on the sample with an ellipsoidal mirror. A motorized hollow mirror allows to work with the laser and the FEL beams in a quasi-collinear geometry at the sample. The transmitted extreme ultraviolet (EUV) radiation is detected with a spectrometer composed by a diffraction grating and CCD camera, while the pump is filtered. The laser pump drives the sample out of equilibrium, reaching high temperatures and triggering the redox process between α-Fe_2O_3 and Al. The label "FEL 1" refers to the FERMI EUV source operating in the low-photon-energy range.[11] In the sketches, the orange spheres represent Fe atoms, the red spheres represent the O atoms and the gray spheres represent Al atoms.

A.2 Results

Pump-Probe Dynamics

The transient transmission is calculated as follows:

$$\Delta T = T_{pp} - T_{pre} \quad \text{(A. 1)}$$

where T_{pre} is the transmission of the unperturbed sample, and T_{pp} is the transmission after pump excitation. In two different sets of measurements, dynamics were recorded for several photon energies across the Al $L_{2,3}$ edge and Fe $M_{2,3}$ edge for the α-Fe_2O_3/Al sample (see **Figs. A.2(a)** and **2(c)**). The temporal sampling has been chosen in such a way as to probe both ultrafast electron-phonon coupling dynamics in the vicinity of time zero with steps of 100 fs and the slower lattice dynamics at larger delays with steps of 10 ps, while intermediate steps of 1 ps in the region of transition between these two regimes are also taken. The pump-probe traces are reported in **Figs. A.2(b)** and **2(d)** along with their fits. The functions employed for the fits are described in the SI. The time constants obtained from the fitting procedure are listed in **Table A.I**.

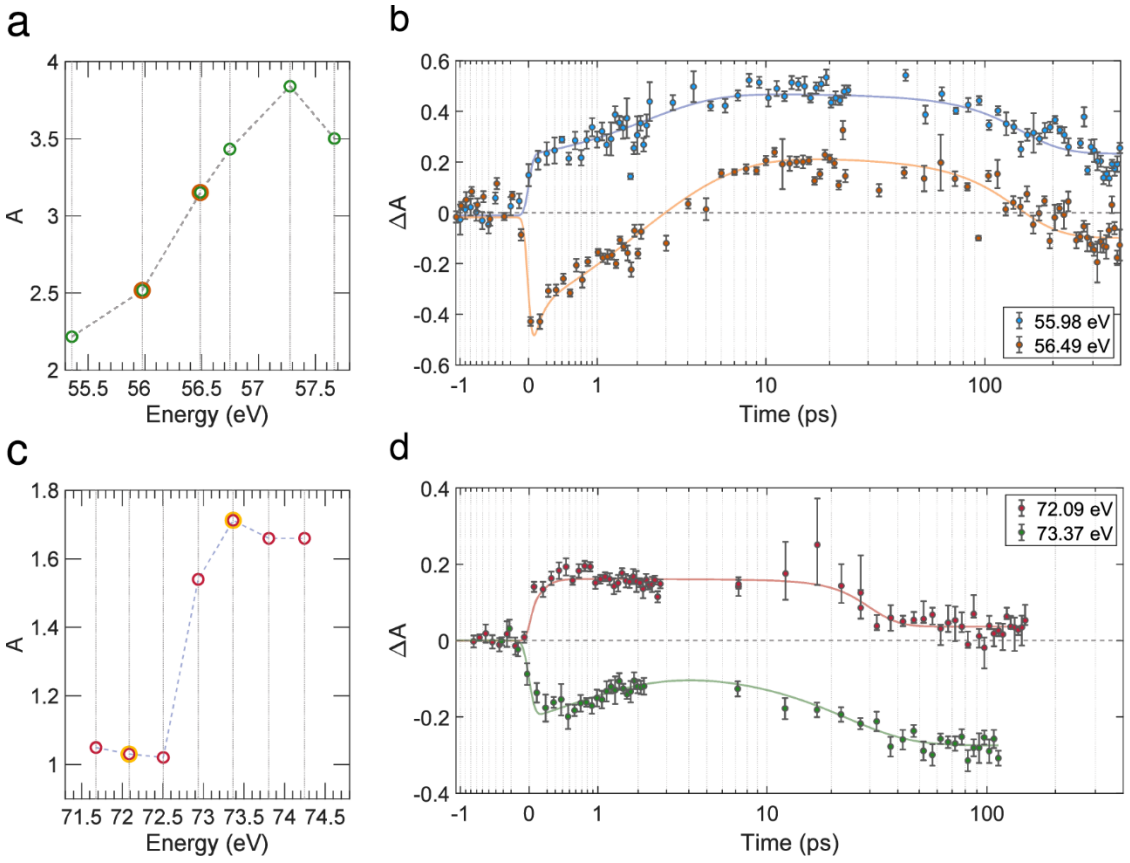

Figure A.2. Static absorption spectra. (a) Absorption at the $M_{2,3}$ edge of iron in hematite and **(c)** $L_{2,3}$ edge of aluminum measured on the α-Fe_2O_3/Al sample. Absorption dynamics probed at **(b)** 55.98 eV and 56.49 eV for the Fe $M_{2,3}$ edge and **(d)** 72.09 eV and 73.37 eV Al $L_{2,3}$ edge. The photon energies which were investigated with the FERMI FEL are highlighted in green in **(a)** and red in **(c)**. The photon energies whose dynamics are shown in **(b)** are highlighted in orange in **(a)** and the photon energies whose dynamics are shown in **(d)** are highlighted in yellow in **(c)**. The fitting functions used for the curves in **(b)** and **(d)** are given in Eqs. (A.9)–(A.11). Error bars are calculated using Eq. (A.6).

Table A.I. Kinetic constants from the fits of the pump-probe traces for aluminum and hematite.

		Fast τ_1 (ps)	Slow τ_2 (ps)
Pre-edge	Al	1.18 ± 0.13	8.3 ± 1.1
	Fe	2.60 ± 0.08	42.0 ± 10.9
Post-edge	Al	1.54 ± 0.21	3.3 ± 0.3
	Fe	1.58 ± 0.16	40.0 ± 6.9

The time constants for the fast part of the dynamic, *i.e.* τ_1, derived from the fit result in few picoseconds for both α-Fe_2O_3 and Al. For Al, τ_1 is reasonable for the equilibration of hot electrons with the lattice via electron-phonon collision in a metal whose behavior resembles that of an ideal free-electron gas and could be described with the two temperature model (TTM).[12,13] For α-Fe_2O_3, τ_1 is larger than for Al and this could be ascribed to the different relaxation dynamics. In the case of hematite, excited carriers interact with the lattice via scattering off electrons with optical phonons which leads to small polaron formation and localization of the charge carrier.[14] The dynamics at 56.49 eV required a second exponential decay ($\tau_1^* = 0.1 \pm 0.06$ ps) to fit the data (see **Appendix A.4**). The presence of this additional term is justified by the fact that this specific photon energy is close to the spectral region where the feature associated with the process of small polaron formation is observed (namely, a blue shift of the invariant absorption point, which is highlighted in **Fig. A.3** and described later). The polaron is interpreted as an additional decay because its formation is associated with the disappearance of hot electrons from the conduction band.

The time constant for the second part of the dynamic, *i.e.* τ_2, is on the order of tens of picoseconds for Al and on the order of tens to hundreds of picoseconds for hematite. Several

studies on fs laser ablation have been performed on aluminum with different fluence regimes.[15–18] High fluences (> 0.05 J/cm^2) have been demonstrated to provoke ultrafast isochoric heating, which leads to the collapse of the overheated material and to the generation of compression pressure of GPas in the central part of the film. Under such conditions, the film is forced to expand, forming low density regions (voids) and nanoparticles within the first tens of picoseconds from the impinging of the laser pump. The time constants τ_2 reported in **Table A.I** and the uniform increase of the transmission at longer delays are in good agreement with the mechanism of ultrafast isochoric heating just described. The absolute variation of the transmission in Al could be associated with a reduction of the number of atoms present in the volume probed by the FEL of ~8%. We did not find similar studies of fs laser ablation on hematite, but since our pump-probe traces have the very same outline for aluminum and hematite, just with different kinetic constants, we can conclude that a similar mechanism of isochoric heating is occurring in hematite as well with high laser fluences. A similar estimation on the reduction of the Fe atoms in the probed volume has been performed, resulting in a decrease of ~5%. Nevertheless, the variation of the absorption cross-section is likely to depend on other phenomena as well, *i.e*. phase transformations and change of the refractive index. The significantly higher kinetic constants in the case of hematite (a wide-band gap semiconductor) can be explained in terms of a lower heat conductivity and a higher heat capacity. As a consequence, the heating is smaller and the consequent expansion of the lattice is slower.

Understanding the dynamics of the two species that compose our bilayer sample was essential for establishing on a solid ground whether the requirements for starting the thermite redox process are met in our experiment. Studies on the thermite reaction[3,5,6] have identified the melting of aluminum as a fundamental step for triggering the redox reaction between aluminum and iron oxide. In the simulation from Tang *et al*.,[15] a 200 fs laser pulse with a fluence of ≃0.06 J/cm^2 provokes thermal melting via collapse of the crystal structure of a 100 nm thick aluminum film within the first 2 ps, raising the temperature of the lattice on the side of the sample exposed to the beam up to 3000 K. In our experiment, the laser pump fluence was set to ≃0.9 J/cm^2, therefore the temperature of the lattice on the side of the film

facing hematite has been raised at temperatures even higher than 3000 K, ensuring that the key condition for triggering the redox process, *i.e.* melting of aluminum, is satisfied. Furthermore, the collapse of the crystal structure, the expansion/disgregation of the individual layers forced by the compressive pressure and the formation of nanoparticles seems to be a condition that favors the mixing and maximizes the contact area between the two species at the interface.

In **Fig. A.3**, the pump-probe traces measured at several energies for α-Fe_2O_3 (left panel) and Al (right panel) are plotted together to provide a comprehensive picture of the results of the measurement and to help visualize the trend of the dynamic traces across the two absorption edges. The sign of the variation of absorbance reflects the broadening of the Fermi-Dirac distribution caused by the rise of the temperature of the electrons upon excitation by the laser pump. Indeed, the blue regions at lower energies are associated with an increase of absorbance while the red regions at higher energies are associated with a decrease of absorbance.

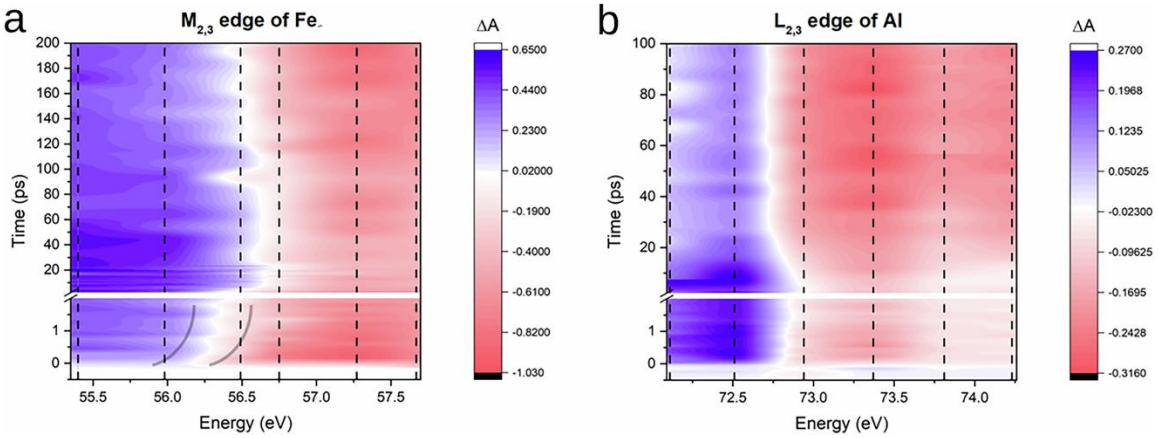

Figure A.3. Transient absorption traces of the α-Fe_2O_3/Al sample. Transient absorption (TA) traces of the α-Fe_2O_3/Al sample across the **(a)** Fe $M_{2,3}$ and **(b)** Al $L_{2,3}$ absorption edges. The dashed lines are the pump-probe dynamics measured in the experiment and interpolated over a uniform time mesh to plot them together. The 2D-maps are obtained by interpolation of the time traces over the photon energies measured in the experiment and

serve the purpose of providing an overall picture of the results of the dynamic behavior of the absorption edges.

Figure A.4 shows static spectra and transient spectra for different pump-probe delays that help in visualizing the trend of variation of the absorption. In the two TA maps, the local variation of the density of the two materials, that are forced to expand by the compressive pressure which arises from the ultrafast isochoric heating, can also be observed in the decrease of absorbance that consistently occurs after tens of picoseconds (the blue region becomes weaker, the red region becomes more intense in both the TA maps).

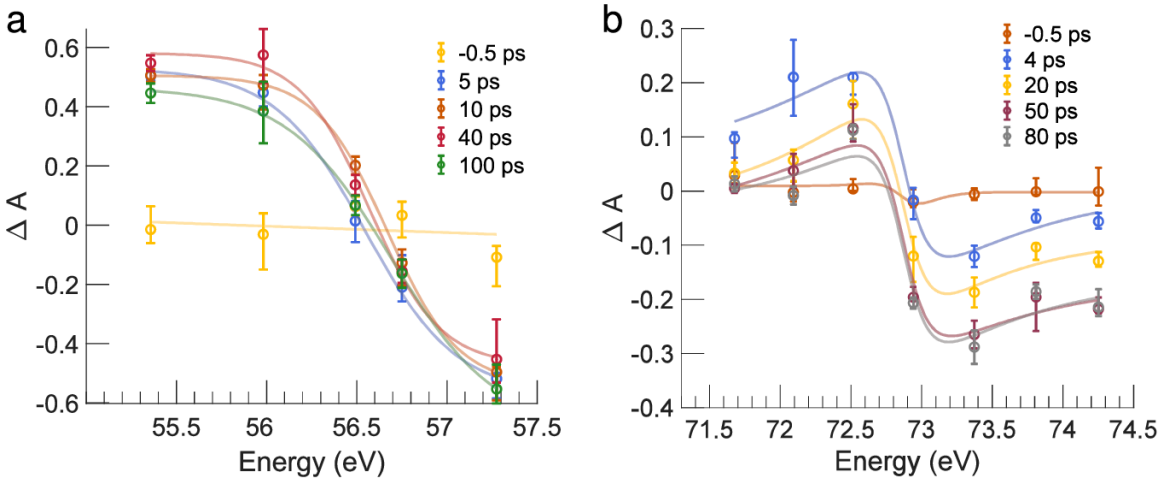

Figure A.4. Transient absorption spectra of the α-Fe_2O_3/Al sample. Transient absorption (TA) spectra at some representative delays for **(a)** Fe $M_{2,3}$-edge of hematite and **(b)** Al $L_{2,3}$-edge of aluminum. The flexible sigmoid function used for the fits is reported in **Appendix A.4**. For the Al TA, the difference between two sigmoid functions has been employed for the fitting. Error bars are calculated using Eq. (A.6).

Transient Absorption Spectra at the Fe $M_{2,3}$ Edge

In the study of Carneiro *et al.*,[10] it has been demonstrated that a specific spectroscopic feature in the TA spectrum, *i.e.* the shift of the zero-crossing in the first hundreds of fs, is the fingerprint of small polaron formation in the spectral region between 56 and 58 eV. Polaron

formation is a two-step process: (i) the first step is the optical excitation, which has a charge transfer nature, involving the displacement of an electron from the O 2*p* orbitals to the Fe 3*d* orbitals and, consequently, a variation of the oxidation state of Fe from +3 to +2; (ii) the second step is the interaction of the carriers with optical phonons provoking a local distortion of the lattice, which induces self-trapping. They propose a kinetic model where polarons are formed by bimolecular recombination of hot electrons and optical phonons. Polarons appear within 100 fs and their population continues to grow for 2-3 ps, when the hot electrons and phonons populations are consumed. Comparing our TA measurement at Fe $M_{2,3}$ edge with the study of Carneiro *et al*., we have observed the same feature, regardless the fact that we employed a 785 nm pump, which is well below the α-Fe_2O_3 bandgap ($\simeq$ 560 nm), while they were using an optical pump above the bandgap of α-Fe_2O_3. The left panel of **Fig. A.3** shows a detail of the transient absorption spectrum of hematite (on aluminum) at the Fe $M_{2,3}$ edge in the first picoseconds of the pump-probe measurement. The shift of the zero crossing point[10] is highlighted by the gray lines. Such observation poses a question on the nature of the excitation mechanism. According to the literature, two-photon absorption (TPA) is the dominant mechanism for excitation in hematite for photon energies below its bandgap. Okazaki *et al*.[19] demonstrated this by studying the excitation mechanism of a hematite photoanode in contact with a gold nanorod using transient absorption spectroscopy. Their findings showed that TPA must be considered to explain the dynamics of hematite transient absorption spectra when using an excitation wavelength of 800 nm. Additionally, good efficiencies for non-linear optical processes in the near-infrared region, such as at 1064 and 1340 nm,[20] further support the occurrence of TPA in hematite at longer wavelengths relative to its visible bandgap. Since TPA in hematite was observed using a laser pump at 800 nm with a fluence of 1.0 mJ/cm^2, in the case of our experiment TPA is most likely the dominant mechanism of excitation.

Comparison of the Shift in the Zero-Crossing Point between α-Fe_2O_3 on Al and α-Fe_2O_3 on Parylene

In **Fig. A.5**, transient soft-X-ray absorption spectra at the Fe $M_{2,3}$ edge are reported for the α-Fe_2O_3/parylene sample and for the α-Fe_2O_3/Al sample. The spectra are fitted over the

transient absorption values from the single wavelength pump probe experiments across the Fe $M_{2,3}$ edge for two selected delays. The fit is weighted on the errors of the individual experimental points and the details of the fitting procedure are described in **Appendix A.4**. The difference of the spectral behavior in time is highlighted in **Figs. A.5(a)** and **5(b)** by the dashed vertical lines, that help to visualize the shift of the zero-crossing point with the pump-probe delay. Comparing our spectra of hematite deposited on Al and on parylene, we have observed a noticeable difference in the blue shift of the zero-crossing point, that we quantified to be ~0.1 eV for α-Fe_2O_3 on Al and ~0.2 eV for α-Fe_2O_3 on parylene going from 0.3 ps to 2.2 ps. To confirm this observation, we computed the shift for several delays, taking as a reference 52.2 eV, the value of the zero-crossing at 0.1 ps. We monitored the behavior of the shift for the α-Fe_2O_3/Al sample and for the α-Fe_2O_3/parylene sample. The trend observed by comparing **Figs. A.5(a)** and **5(b)** is consistent for several delays and it is shown in **Fig. A.5(d)**. The α-Fe_2O_3/Al sample shows a smaller blue shift. The origin of the smaller blue shift observed in the case of the α-Fe_2O_3/Al sample could be attributed to the injection of charge from Al to α-Fe_2O_3. The electrons injected into α-Fe_2O_3 are likely to be localized in the form of small polarons as well, but the mechanism might be different because the charge balance of the material is overall altered. This interpretation is supported by the observation of a reduction of α-Fe_2O_3 by a metal in the aforementioned study from Okazaki *et al*.[19] Furthermore, it is reasonable to think that this phenomenon would occur in the experimental conditions of the present investigation, since we proved to satisfy the conditions to start the reaction and the reduction of hematite is reported to be the first step of the thermite reaction.[3] Additionally, to corroborate our hypothesis, a red shift of the transient signal has been predicted from the calculation performed on hematite in the work from Klein *et al*.[21] when excited carriers are included in the computation of the polaron state. Finally, a red shift of the Fe $M_{2,3}$ absorption edge is predicted for a reduction of Fe from +3 to +2 oxidation state, as it can be seen from the result of the simulation of the static absorption of FeO and α-Fe_2O_3 in **Fig. A.5(c)**. Our results support the idea that an electron transfer between aluminum and hematite is taking place upon excitation of the α-Fe_2O_3/Al sample with a high power 785 nm pulse. On longer time scales (tens to hundreds of picoseconds), we have not observed any increase in the Fe $M_{2,3}$ shift between the two samples, α-Fe_2O_3/Al

and α-Fe_2O_3/parylene. Therefore, we deduced that either (i) the redox reaction is only partially taking place (reduction of α-Fe_2O_3 by Al) in the time interval investigated or (ii) the reaction is maybe proceeding only near the interface, limited by the mass transport. According to the study from Shimojo *et al.*,[22] the breaking of Fe-O bond and consequent formation of Al-O bonds at the interface would occur within few picoseconds (< 5 ps). Hence, the latter interpretation (reaction occurring only near the interface) is reasonable and the lack of spectroscopic signatures may be attributed to an insufficient contrast to see a relevant difference in presence of the aluminum.

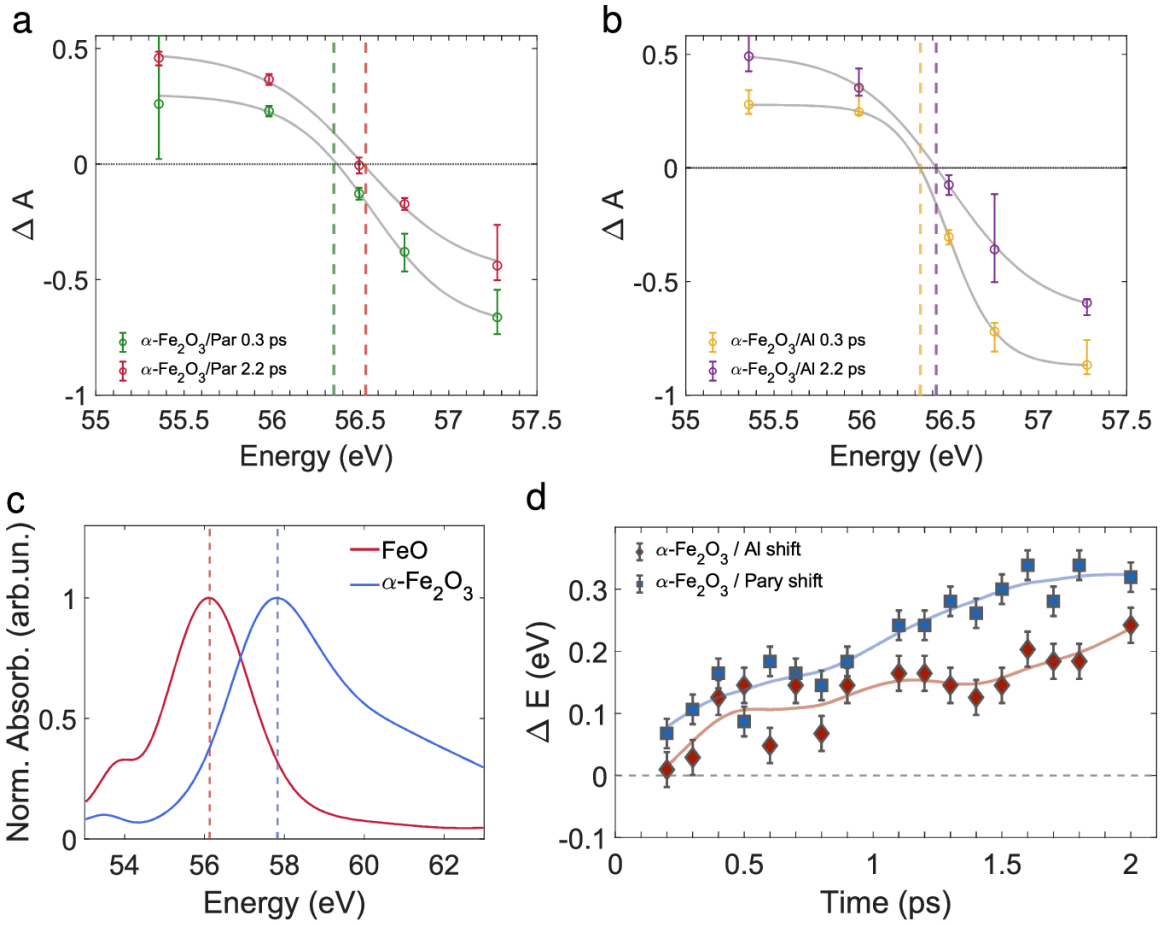

Figure A.5. Comparison of the shift in the zero-crossing point between α-Fe_2O_3 on Al and α-Fe_2O_3 on parylene. Spectra from the TA trace of **(a)** the α-Fe_2O_3/parylene sample and **(b)** the α-Fe_2O_3/Al sample at the Fe $M_{2,3}$ absorption edge. Two delays were selected (0.3 and 2.2 ps) to show the shift of the zero-crossing. **(c)** Simulation of the static absorption

spectra for the Fe $M_{2,3}$-edge for FeO and α-Fe_2O_3. **(d)** Evolution of the shift of the zero-crossing point with respect to the crossing at $t = 0.1$ ps for the α-Fe_2O_3/Al sample (red) and for the α-Fe_2O_3/parylene sample (blue). The errors are calculated as the root means square of the residuals with respect to the fit of the two distributions.

Transient Absorption Spectra at the Al $L_{2,3}$ Edge

Concerning the Al $L_{2,3}$ absorption edge, simulations of the static absorption spectra of the $L_{2,3}$ edge for Al and α-Al_2O_3 are reported in **Fig. A.6(a)**. The absorption spectrum of α-Al_2O_3 is predicted to be blue shifted by ~6 eV with respect to the spectrum of Al. In **Fig. A.6(b)**, absorption spectra are reported for five selected delays in order to span the time window covered by the pump-probe measurements. A coherent blue shift of the absorption traces with time can be observed. Comparing the simulated spectra with the experimental time-dependent traces, we have made the following considerations: (i) according to Shimojo *et al*.,[22] Al-O bonds form at the interface with α-Fe_2O_3, but the aluminum layer is 100 nm thick, so the bond formation process affects only a small fraction of the Al atoms in the overall volume probed by the FEL beam, resulting in a blue-shift which is detectable but not dramatic as the one predicted in **Fig. A.6**; (ii) the isochoric heating leads to hydrodynamic expansion and consequently to complete ablation of the sample within nanoseconds. On this time scale, the species migrate and interdiffuse between the two materials to a certain extent, due to the ultrafast raise of the temperature and the consequent strain that leads to the melting/disruption of the solids.[15] The expansion and the transition to the gas phase cause a drop of the density in the volume of sample probed by the FEL in the tens of picoseconds timescale, which, in turn, reduces the TA signal; (iii) the pressure in the experimental chamber was 10^{-6} mbar and gaseous species may have probably been withdrawn from the reaction system, preventing the further proceeding of the reaction; (iv) the time window observed with the pump-probe is a hundred or few hundreds of ps and that may be not sufficient to detect the full progress of the reaction occurring.

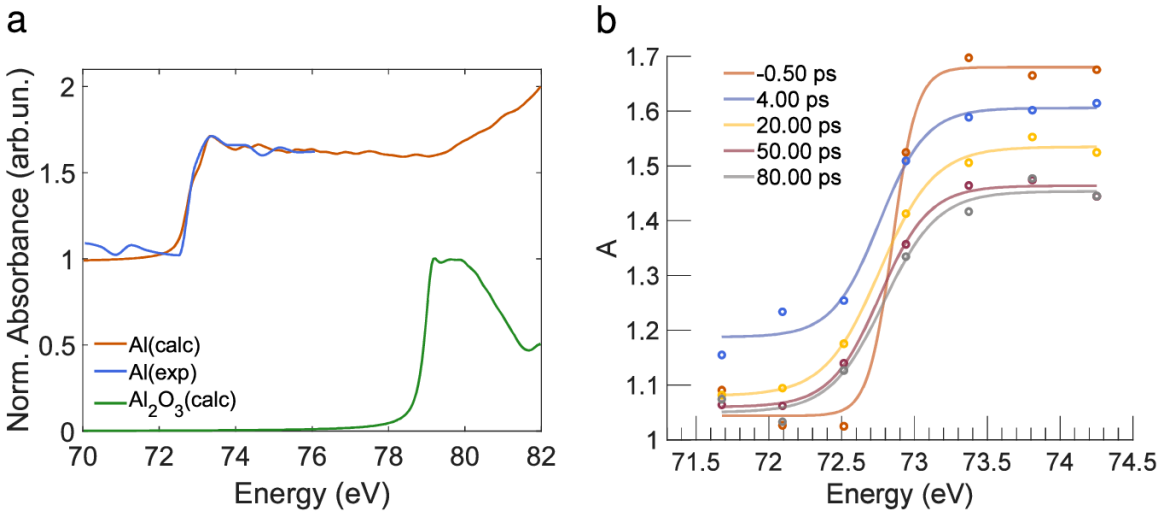

Figure A.6. Absorption spectra of Al $L_{2,3}$ edge. (a) Simulations of the static absorption spectra of the Al $L_{2,3}$ edge for Al and α-Al_2O_3 along with the measured static absorption spectrum of Al. **(b)** Absorption spectra of Al $L_{2,3}$ edge measured for the α-Fe_2O_3/Al sample at five selected pump-probe delays. The flexible sigmoid function used for the fits in (**b**) is reported in Eq. (A.12).

For future investigations, the samples could be modified to avoid the problem of withdrawal of the gaseous species. Additional layers, transparent to the laser pump, may operate as a confinement for the sample; such layers would prevent the gases produced by the laser pump and by the heat released in the first the redox processes from escaping as a result of the low pressure in the experiment chamber. Another option would be that of using hard X-rays to probe the process at deeper core levels, which, on one hand, would not require working in vacuum, and, on the other hand, would offer the benefit of achieving a significantly higher penetration depth. This would allow us to work with more complex sample structure, *e.g.* multilayers, which, in turn, would maximize the number of interfaces in the probed volume, giving more contrast to observe changes associated with the redox reaction. Further information could be gained by introducing an electric field to hinder/favor the electron transfer from aluminum to hematite and observe how such field would influence the transient absorption traces.

A.3 Methods

Samples

The samples investigated in this experiment were customized self-standing nanolayered thin filters, with a large area, approximately 20 mm diameter. The samples were provided by Luxel Corporation and include: (i) a nanometric α-Fe_2O_3 layer deposited on an Al substrate for studying the thermite process, (ii) a nanometric α-Fe_2O_3 layer (nominally 20 nm) deposited on a Parylene-C substrate (nominally 100 nm) and (iii) an Al sub-micrometric foil (100 nm) as a reference for the two independent species (Al and α-Fe_2O_3). XAS measurements at the Fe $M_{2,3}$ edge and Al $L_{2,3}$ edge were conducted in separate experimental runs using different thermite samples. The obtained absorption levels (**Figs. A.2(a)** and **2(c)**) are consistent with a double-layer foil composed of 20 nm α-Fe_2O_3 and 50 nm Al for the Al $L_{2,3}$ edge measurements, and a double-layer foil of 45 nm α-Fe_2O_3 and 100 nm Al for the Fe $M_{2,3}$ edge measurements (see **Appendix A.4**).

The samples of α-Fe_2O_3/Al employed for the investigation on Fe $M_{2,3}$ edge and Al $L_{2,3}$ edge were different ones with the same nominal thickness. However, the actual thickness of the layers of α-Fe_2O_3 and Al were different in the two samples.

Pump-Probe Setup

The experiment was performed at the EIS-TIMEX end station[23] of the FERMI FEL[11] in Trieste, Italy (**Fig. A.1**). TIMEX is an instrument devised for performing destructive pump-probe measurements to investigate systems in extreme conditions. The sample is rastered between each pump-probe measurement to always probe a fresh portion of the sample, which is crucial to study irreversible processes such as thermite reaction. FERMI is a seeded high-gain harmonic generation (HGHG) FEL.[24] The FERMI Ti:Sa femtosecond laser facility generates and shapes the seed pulses employed in the HGHG free-electron lasing process through a customized optical parametric amplifier (OPA).[25] A portion of the fundamental emission at 785 nm from the Ti:Sa laser is delivered to the experimental hall and it is the standard laser used in pump-probe experiments,[26] which was employed in this experiment. Such design provides a jitter of just few femtoseconds.[27] Hence, the aforementioned factors

offer an experimental environment which is robust and well-suited for the present investigation. The duration of the pump pulse was about 80 fs FWHM, the spot size on the sample was 34 × 34 μm^2 FWHM and the intensity of the laser was set to 25 μJ in order to reach a fluence of ~0.9J · cm^{-2} on the sample. Such pump provokes irreversible damage on the sample (ablation) at each shot. Hence, the measurement is carried out in raster scan, single-shot mode, i.e. moving on a fresh region of the sample after each pump shot. We used the radiation produced by the FERMI FEL in the range of photon energy from 54 to 58 eV for probing at the Fe $M_{2,3}$ edge and in the range 73 to 76 eV for probing at the Al $L_{2,3}$ edge. The FEL pulse duration was 60 fs FWHM, and the intensity was 3 μJ estimated by using a calibrated ionization chamber filled with N_2 and located along the beam transport. Spot size of the FEL was 16 × 16 μm^2 FWHM and the fluence at the sample was ~60μJ · cm^{-2} (no damage observed by the probe beam). The spectral broadening factor (i.e. $\Delta\lambda/\lambda$) for the emission of FERMI is of the order of 10^{-3} or 10^{-4} and no monochromators are used along the beam transport. The spectrum of the FEL along the beam transport is monitored by an EUV spectrometer, PRESTO.[28] The detector at TIMEX is a second EUV spectrometer, WEST.[29]

Static Fe $M_{2,3}$ Edge Calculations on FeO and α-Fe_2O_3

The OCEAN code was used to simulate static Fe $M_{2,3}$ edge of two iron oxides with different Fe oxidation states (Fe^{2+} for FeO and Fe^{3+} for α-Fe_2O_3).[30,31] DFT+U calculations were performed with the Quantum ESPRESSO package using pseudopotentials with the Perdew-Burke-Ernzerhof generalized gradient approximation exchange-correlation functionals.[32,33] A cutoff energy of 240 Ry was used for the plane-wave basis set truncation in the DFT calculation. The self-consistent field calculation was done on a 6 × 6 × 6 k-point grid while the screening calculation was done on a 2 × 2 × 2 k-point grid. The number of bands in the screening calculation is consistent between the different structures and the same energy range of unoccupied bands (100 eV) was used for screening calculations for both iron oxides. OCEAN does not calculate the absolute energies of core-level excitations and relative peak shifts were calculated as a sum of the pseudopotential-dependent binding energy, total Kohn-Sham potential, and one-half the screened Coulomb potential of the core-hole.[34,35]

All calculated spectra used identical energy shift and broadening. The calculated stick spectra were broadened with a Gaussian function with the linewidth in full width at half maximum (FWHM) at 0.4 eV ($E \leq 54$ eV) and 0.8 eV ($E > 54$ eV). The energy axis and intensity of the simulated α-Fe_2O_3 spectrum were first matched to the experimental spectrum and the simulated FeO spectrum was aligned using the relative energy shifts obtained from the OCEAN calculations. The Fe $M_{2,3}$ edge exhibits a characteristic peak located at 4.4 eV and 2.1 eV prior to the main peak for α-Fe_2O_3 and FeO, respectively, which is consistent with reported experimental results.[9,36]

Static Al $L_{2,3}$ Edge Calculations on Al and α-Al_2O_3

The same computational code was used to obtain static Al $L_{2,3}$ edge of Al and α-Al_2O_3. These calculations were performed with optimized norm-conserving Vanderbilt pseudopotentials generated using the ONCVPSP code modified for the OCEAN code.[37] A cutoff energy of 240 Ry was set in the DFT calculations. The self-consistent field calculation was done on a 16 × 16 × 16 k-point grid while the screening calculation was done on a 2 × 2 × 2 k-point grid. The number of bands in the screening calculation is consistent between the different structures and the same energy range of unoccupied bands (200 eV) was used for screening calculations. The aforementioned approach to calculate relative peak shifts was used.

All calculated spectra used identical energy shift and broadening. The calculated unbroadened spectra were broadened with a Lorentzian linewidth in FWHM increasing linearly from 0.01 eV at 70 eV to 0.3 eV at 82 eV and higher. And the spectra were convoluted with a Gaussian function with FWHM calculated from the resolving power of the WEST spectrometer to account for instrumental broadening. The energy axis and intensity of the simulated Al spectrum were first matched to the experimental spectrum and the simulated α-Al_2O_3 spectrum was aligned using the relative energy shift obtained from the OCEAN calculation. The Al $L_{2,3}$ edge of α-Al_2O_3 is blue-shifted compared to that of Al due to the change in the oxidation state from Al^{3+} to Al and the simulated spectra match well with the reported results using electron energy-loss spectroscopy.[38]

A.4 Supplementary Information

Data Processing and Fitting

For the raster scan pump-probe measurements the transmission of the unperturbed sample, I_{pre}, is measured five times before the pump-probe shot, I_{pp}, and then two measures of the crater generated by the pump beam, I_{post}, are performed as a sanity check of the measurement. This procedure is repeated five times for each pump-probe delay and then processed to obtain an averaged value for I_{pre}, I_{pp} and I_{post} and an error for the transmission value of each delay.

The first step of the data analysis process is the measure of the beamline transmission and a calibration of the correlation between the two spectrometers, Presto (upstream) and WEST (downstream). This is a procedure that is performed without the sample for every photon energy employed in the experiment. The signal for both the spectrometers is obtained by reading the output current of the CCD sensor in full vertical binning mode. The signal is obtained by integrating over the spectral region of interest (ROI). To account for the black noise, the integral over the extracted background baseline is subtracted from the total integral of the signal (**Fig. A.7**).

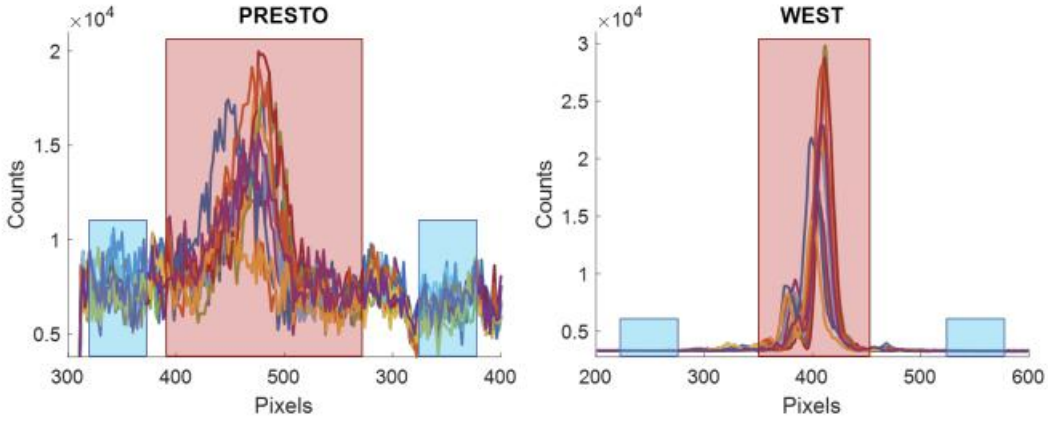

Figure A.7. Spectra of 10 shots measured with PRESTO (left panel) and with WEST (right panel). The blue rectangles highlight the regions whose area underneath were taken as the background, while the red rectangles highlight the regions whose area underneath were taken to calculate the signal by subtracting the background.

A correlation function between the counts on PRESTO and the counts on WEST is established in order to get the transmission of the beamline in the working configuration without the sample. The function is determined with a third order polynomial fit, to express the counts on WEST as a function of the counts of PRESTO. A binning is performed on the measured FEL shots, dividing the counts on PRESTO in 100 intervals and taking for each interval the average value of the counts on WEST with the associated standard deviation as error. The fit is then calculated over the binned values, taking the reciprocal of squares of the errors as weights for the individual points (**Fig. A.8**).

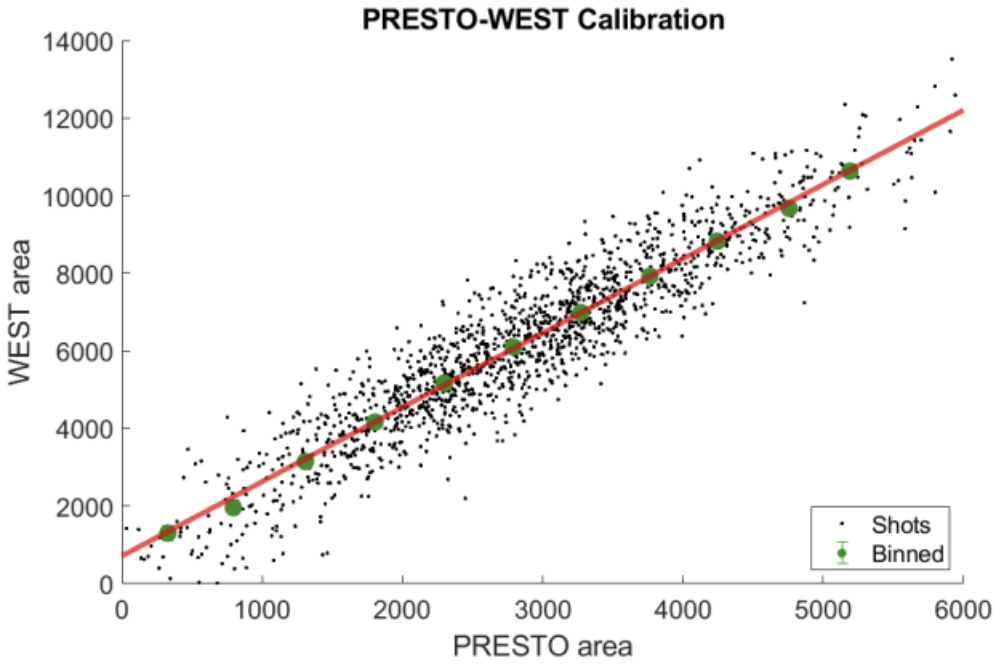

Figure A.8. Correlation function between the two spectrometers PRESTO and WEST. The black dots are the shots measured and the blue dots are the shots that are filtered out. The red dots with the error bars are the binned values, while the red line is the fit.

The pump-probe shots are filtered with the quantile approach. The set of pump-probe transmission values are used to generate a set of 10 evenly spaced values (i.e. deciles). The

values which are above the 9th quantile or below the 1st quantile are discarded. In this way, the shots whose intensity is significantly different from the median are removed. Accordingly, the preshots and the postshots associated with the removed pump-probe shots are discarded as well. For the filtered shots, the transmission values of the preshots, pump-probe and postshots are plotted against the delays to obtain a comprehensive picture of the measurement at the monitored photon energy. The overall trend could be summarized as follows:

- The preshots and the pump-probe shots have an intensity which is significantly lower than the postshots. This is reasonable since the preshots and the pump-probe shots interact with the sample, while the postshots basically pass through the experimental chamber unaffected, because the sample is completely ablated by the pump pulse, and hence their transmission is (supposed to be) always close to 1.

- The intensity of the pump-probe shots covers a wider interval with respect to the intensities of the preshots.

The intensity of the WEST spectrometer downstream (I1) has been plotted against the intensity of the PRESTO spectrometer upstream (I0) to check their correlation for the preshots, the pump-probe and the postshots (**Fig. A.9**).

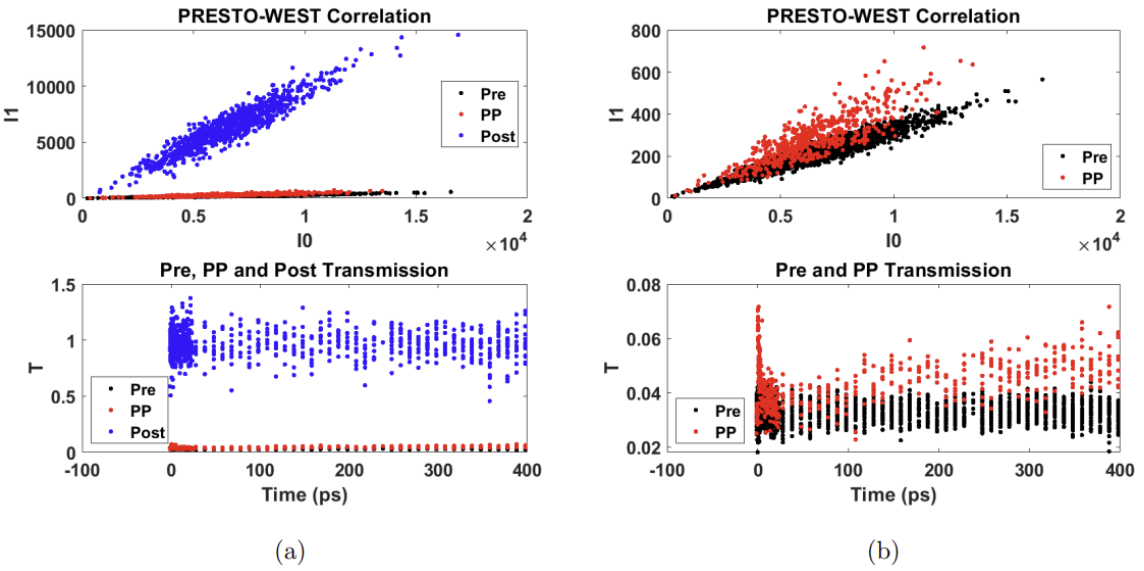

Figure A.9. Unprocessed transmission of the filtered measurements (top panels) and correlation between PRESTO (upstream) and WEST (dowstream) spectrometers (bottom panels) for (a) preshots, pump-probe, and postshots and (b) preshots and pump-probe.

After the first filtering, a binning procedure was carried out in order to obtain a single value for the transmission with an associated interval of confidence for each delay where the measurement was performed. The binning is performed individually for preshots, pump-probe, and postshots and it consists of taking the average of the transmission values and calculating the error as the standard deviation associated with this collection of values and dividing it by the square root of the number of shot minus one, as formalized in the following equation:

$$T_j^{bin} = \frac{1}{n_j}\sum_{i=1}^{n_j} T_i^j \text{ and } \sigma_{T_j} = \sqrt{\frac{1}{n_j - 1}\sum_{i=1}^{n_j}\left(T_i^j - \bar{T}^j\right)^2} \quad \text{(A. 2)}$$

where the index j represents preshots, pump-probe or postshots and n is the number of shots within these groups for a single delay.

The normalized variation of transmission of the pump-probe measurements is calculated as follows:

$$\Delta T_{norm} = \frac{\Delta T}{T_{pre}} = \frac{T_{pp} - T_{pre}}{T_{pre}} \tag{A.3}$$

and the propagation of the errors is calculated accordingly:

$$\begin{aligned}\sigma_{\Delta T} &= \sqrt{\left(\frac{1}{T_{pre}}\sigma_{T_{pp}}\right)^2 + \left(\frac{1}{T_{pre}}\sigma_{T_{pre}}\right)^2 + \frac{2}{T_{pre}}\sigma_{T_{pre}T_{pp}} + \left(\frac{T_{pp} - T_{pre}}{T_{pre}^2}\sigma_{T_{pre}}\right)^2} \\ &\approx \sqrt{\left(\frac{1}{T_{pre}}\sigma_{T_{pp}}\right)^2 + \left(\frac{1}{T_{pre}}\sigma_{T_{pre}}\right)^2 + \left(\frac{T_{pp}}{T_{pre}^2}\sigma_{T_{pre}}\right)^2 - \left(\frac{1}{T_{pre}}\sigma_{T_{pre}}\right)^2} \\ &\approx \sqrt{\left(\frac{1}{T_{pre}}\sigma_{T_{pp}}\right)^2 + \left(\frac{T_{pp}}{T_{pre}^2}\sigma_{T_{pre}}\right)^2}\end{aligned} \tag{A.4}$$

The normalized transmission and its associated errors (obtained respectively from Eqs. (A.2) and (A.3)) are plotted against the pump-probe delays to obtain the refined time-dependent trace reported in **Fig. A.10(a)**. The transmission is then manipulated in order to obtain the time-dependent trace in terms of the variation of absorbance (ΔA), calculated as follows:

$$\Delta A = A_{pp} - A_{pre} = \log\left(\frac{1}{T_{pp}}\right) - \log\left(\frac{1}{T_{pre}}\right) = \log(T_{pre}) - \log(T_{pp}) \tag{A.5}$$

The interval of confidence of the absorbance values is no longer symmetric with respect to the values themselves because of the logarithm. Hence, the interval of confidence in the absorption scale is computed by taking the logarithm of the upper and lower bounds of the interval of confidence in the transmission scale, as illustrated in the following equation:

$$A_{lower} = -\log\left(T_{pp} - 0.5\sigma_{T_{pp}}\right) \text{ and } A_{upper} = -\log\left(T_{pp} + 0.5\sigma_{T_{pp}}\right) \tag{A.6}$$

The absorbance values and their associated intervals of confidence are employed to generate the transient absorption trace reported in **Fig. A.10(b)**.

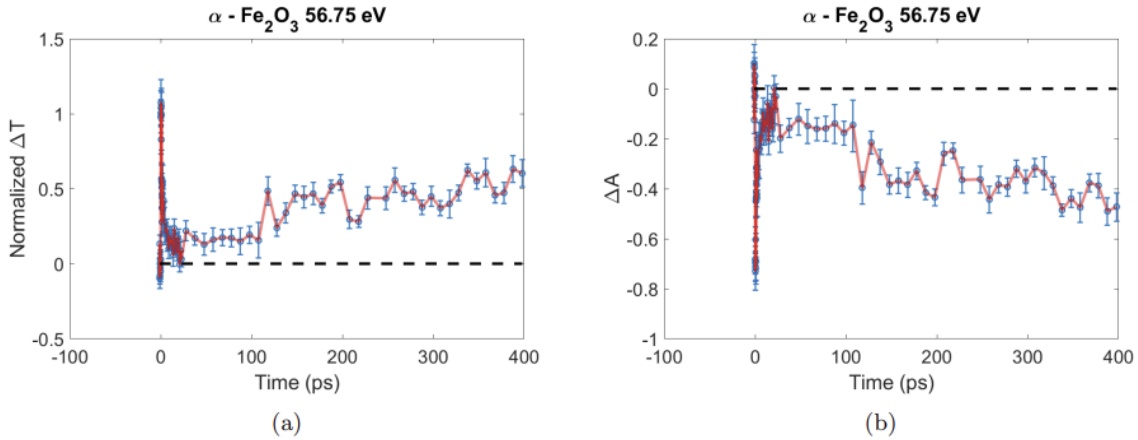

Figure A.10. (a) Processed transmission and (b) transient absorption for the pump–probe time-dependent traces.

Neglecting the jitter between the pump and the probe, which at FERMI is just few femtoseconds, the temporal resolution for the pump-probe signal around t_0 is limited by the convolution between the duration of the pump pulse ($\sigma^t_{pump} \sim 80$ fs) and the probe pulse ($\sigma^t_{probe} \sim 60$ fs):

$$\Delta t_{lim} = \sqrt{\left[\sigma^t_{pump}\right]^2 + \left[\sigma^t_{probe}\right]^2} \cong 100 \text{ fs} \qquad (A.7)$$

The rise at t_0 was fitted for the traces of aluminum and hematite reported in **Fig. A.11** using an error function:

$$f_r = a\left[1 + \text{erf}\left(\frac{t}{\sigma\sqrt{2}}\right)\right] \text{ where } \text{erf}(x) = \frac{1}{\sqrt{2\pi}}\int_{x_1}^{x_2} e^{-x^2}\, dx \qquad (A.8)$$

The raise time FWHM was estimated 65 fs for hematite and 102 fs for aluminum.

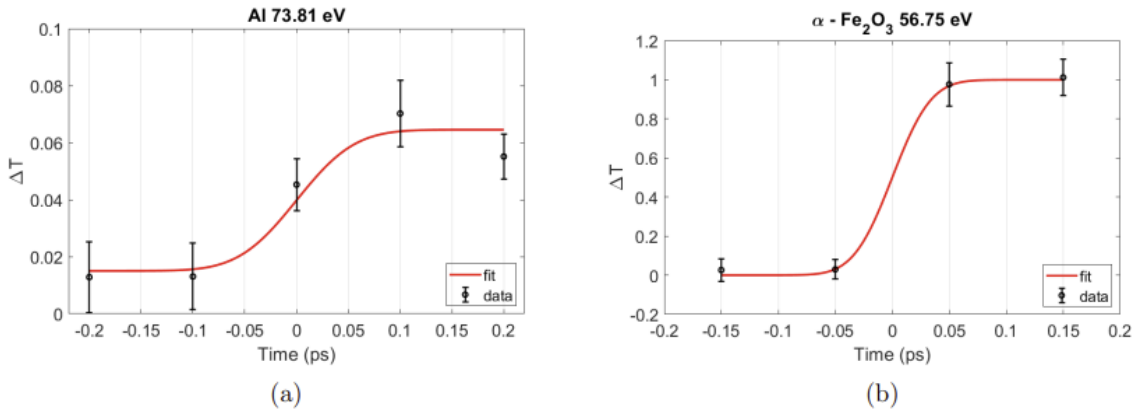

Figure A.11. Details of the rise dynamics of (a) Al and (b) α-Fe_2O_3 around delay zero between laser pump and FEL probe.

The reciprocal of the square of the error associated to the normalized transmission of each pump–probe delay was used as weights for the fit of the dynamics of all the measured photon energies. The choice for the function used to fit the overall pump probe traces was made with the goal of fitting two processes that occur with different time scales:

- Fast dynamics: the equilibration of hot electrons with the lattice via scattering off with optical phonons, which occurs in hundreds of femtoseconds to the first few picoseconds.

- Slow dynamics: the dynamics of the lattice which is stressed by the ultrafast raising of the temperature, which occurs in tens to hundreds of picoseconds.

The equation adopted for the fit of the dynamics at energies above the inflection point of the absorption edges was the following:

$$f = \theta(t) \cdot \frac{1}{2}\left[1 + \mathrm{erf}\left(\frac{t}{\sigma\sqrt{2}}\right)\right] \cdot \left[A_1 e^{-\frac{t}{\tau_1}} + \frac{A_2}{1 + e^{-\frac{1}{\tau_2}(t-z)}}\right] \qquad (A.9)$$

The equation employed to fit the dynamics at energies below the inflection point of the absorption edges was slightly different:

$$f = \theta(t) \cdot \frac{1}{2}\left[1 + \mathrm{erf}\left(\frac{t}{\sigma\sqrt{2}}\right)\right] \cdot \left[\frac{A_1}{1 + e^{-\frac{t}{\tau_1}}} + \frac{A_2}{1 + e^{-\frac{1}{\tau_2}(t-z)}}\right] \qquad (A.10)$$

In Eqs. (A.9) and (A.10), *t* is the independent variable which correspond to the delay between pump and probe beams, σ is the parameter associated to the time resolution that appeared in Eq. (A.8), A_1 and A_2 are the pre-exponential factors, τ_1 and τ_2 are the kinetic constants for the fast and slow dynamics, respectively, and *z* is a parameter that represent the time that the slow lattice dynamic takes to become the dominant contribution. The only difference between Eqs. (A.9) and (A.10) concerns the term to describe the fast dynamic. In the first case an exponential was chosen in agreement with other transient 6 absorption studies reported in the literature, but in the second case (*i.e.* energies below the absorption edge), we opted for a logistic function to perform the fit. The fact that an exponential function with a negative pre-exponential did not work for fitting the dynamics at energies below the absorption edge is probably due to the fact that the trend of the transmission is discordant between the pump-probe traces above and below the absorption edges in the case of the fast dynamic, while it is concordant in the case of the slow dynamic. The fits led to similar kinetic constant regardless of the choice of different functional form.

Interestingly, for the dynamics measured at 56.49 eV, a different function was used to fit the first decay after t_0, featuring an additional exponential decay term for the fast dynamic (indicated in the following equation with the apex $*$):

$$f = \theta(t) \cdot \frac{1}{2}\left[1 + \mathrm{erf}\left(\frac{t}{\sigma\sqrt{2}}\right)\right] \cdot \left[A_1 e^{-t/\tau_1} + A_1^* e^{-t/\tau_1^*} + \frac{A_2}{1 + e^{-\frac{1}{\tau_2}(t-z)}}\right] \qquad (A.11)$$

The fitting of the transient absorption spectra was performed using a parametrized sigmoid function (s(x)), which provided the flexibility to adapt to the different shapes of the spectra over the delays investigated. The function adopted is the following:

$$s(x; a_0, b_0. x_0, y_0) = \frac{a_0}{1 + e^{-b_0(x-x_0)}} + y_0 \qquad (A.12)$$

where a_0, b_0, x_0, y_0 are the parameters. This function has been employed in a non-linear least square fitting procedure to fit the transient spectra of the individual delays by finding the optimal set of the parameters of the sigmoid function. The weight of each experimental point in the fit has been set as the reciprocal of the associated error on the absorbance. Being the confidence interval of the absorption asymmetric, the error has been considered as the total uncertainty.

Details of the Spectrometers

The PRESTO spectrometer is located along the beam transport upstream with respect to the experimental chamber. It is composed of a diffraction grating, a YAG screen and CCD camera (Hamamatsu). The diffraction grating separates the different spectral components onto the YAG screen, whose fluorescence is captured by the CCD camera, so to avoid damaging of the sensor. The WEST spectrometer, located downstream with respect to the experimental chamber, features a diffraction grating that disperses different wavelengths directly onto the sensor of the CCD camera (Andor iKon-M). WEST is equipped with a filter wheel before the CCD to attenuate the incoming FEL radiation when needed to avoid saturation or damaging of the camera. WEST and PRESTO spectrometers have a resolving power respectively of ~7000–25000, which is adequate for monitoring the FEL peaks profile. The combination of two spectrometers, one upstream (I_{up}) and one downstream (I_{down}), allows for drawing a calibration curve for I_{down} as a function of I_{up} without the sample, providing a measure of the transmission efficiency of the beamline for each photon energy employed in the experiment, which is then used during the data processing to isolate the variation of intensity caused by the sample.

Sample Thickness

The thickness assessment of the double-layer thermite foils used in our XAS measurements in transmission geometry was performed using the CXRO calculator (https: //henke.lbl.gov/optical constants/filter2.html). In the calculations, densities of 5.26g/cm^3 and

2.70g/cm^3 were considered for α-Fe_2O_3 and Al, respectively. Oxidation of the free surfaces of the double foil due to atmospheric oxygen was neglected. **Figure A.12** shows the theoretical absorption of α-Fe_2O_3 and Al thin foils across the Fe $M_{2,3}$ edge and the Al $L_{2,3}$ edge for two different thickness combinations corresponding to the samples used in our experiments:

- Absorption of a double-layer consisting of 45 nm α-Fe_2O_3 and 100 nm Al
- Absorption of a double-layer consisting of 20 nm α-Fe_2O_3 and 50 nm Al

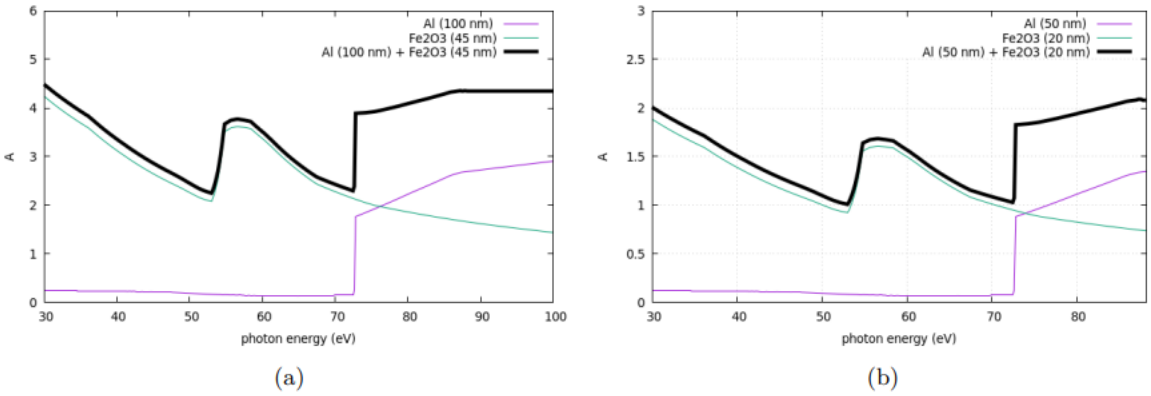

Figure A.12. Theoretical absorption calculation across the Fe $M_{2,3}$ edge and the Al $L_{2,3}$ edge for selected α-Fe_2O_3 and Al nanometric foils.

A.5 References

(1) Granier, J. J.; Pantoya, M. L. Laser Ignition of Nanocomposite Thermites. *Combust. Flame* **2004**, *138* (4), 373–383.

(2) Pantoya, M. L.; Granier, J. J. Combustion Behavior of Highly Energetic Thermites: Nano versus Micron Composites. *Propellants Explos. Pyrotech.* **2005**, *30* (1), 53–62.

(3) Durães, L.; Costa, B. F. O.; Santos, R.; Correia, A.; Campos, J.; Portugal, A. Fe_2O_3/Aluminum Thermite Reaction Intermediate and Final Products Characterization. *Mater. Sci. Eng. A* **2007**, *465* (1), 199–210.

(4) Wang, Y.; Song, X.; Jiang, W.; Deng, G.; Guo, X.; Liu, H.; Li, F. Mechanism for Thermite Reactions of Aluminum/Iron-Oxide Nanocomposites Based on Residue Analysis. *Trans. Nonferrous Met. Soc. China* **2014**, *24* (1), 263–270.

(5) Mileham, M. L.; Kramer, M. P.; Stiegman, A. E. Laser Initiation Processes in Thermite Energetic Materials Using Laser Desorption Ionization Time-of-Flight Mass Spectrometry. *J. Phys. Chem. C* **2007**, *111* (45), 16883–16888.

(6) Stiegman, A. E.; Park, C.-D.; Mileham, M.; van de Burgt, L. J.; Kramer, M. P. Dynamics of Al/Fe_2O_3 MIC Combustion from Short Single-Pulse Photothermal Initiation and Time-Resolved Spectroscopy. *Propellants Explos. Pyrotech.* **2009**, *34* (4), 293–296. https://doi.org/10.1002/prep.200800021.

(7) Pathak, S.; Ibele, L. M.; Boll, R.; Callegari, C.; Demidovich, A.; Erk, B.; Feifel, R.; Forbes, R.; Di Fraia, M.; Giannessi, L.; Hansen, C. S.; Holland, D. M. P.; Ingle, R. A.; Mason, R.; Plekan, O.; Prince, K. C.; Rouzée, A.; Squibb, R. J.; Tross, J.; Ashfold, M. N. R.; Curchod, B. F. E.; Rolles, D. Tracking the Ultraviolet-Induced Photochemistry of Thiophenone during and after Ultrafast Ring Opening. *Nat. Chem.* **2020**, *12* (9), 795–800.

(8) Attar, A. R.; Bhattacherjee, A.; Pemmaraju, C. D.; Schnorr, K.; Closser, K. D.; Prendergast, D.; Leone, S. R. Femtosecond X-Ray Spectroscopy of an Electrocyclic Ring-Opening Reaction. *Science* **2017**, *356* (6333), 54–59.

(9) Vura-Weis, J.; Jiang, C.-M.; Liu, C.; Gao, H.; Lucas, J. M.; de Groot, F. M. F.; Yang, P.; Alivisatos, A. P.; Leone, S. R. Femtosecond $M_{2,3}$-Edge Spectroscopy of Transition-Metal Oxides: Photoinduced Oxidation State Change in α-Fe_2O_3. *J. Phys. Chem. Lett.* **2013**, *4* (21), 3667–3671.

(10) Carneiro, L. M.; Cushing, S. K.; Liu, C.; Su, Y.; Yang, P.; Alivisatos, A. P.; Leone, S. R. Excitation-Wavelength-Dependent Small Polaron Trapping of Photoexcited Carriers in α-Fe_2O_3. *Nat. Mater.* **2017**, *16* (8), 819–825.

(11) Allaria, E.; Badano, L.; Bassanese, S.; Capotondi, F.; Castronovo, D.; Cinquegrana, P.; Danailov, M. B.; D'Auria, G.; Demidovich, A.; De Monte, R.; De Ninno, G.; Di Mitri, S.; Diviacco, B.; Fawley, W. M.; Ferianis, M.; Ferrari, E.; Gaio, G.; Gauthier, D.; Giannessi, L.; Iazzourene, F.; Kurdi, G.; Mahne, N.; Nikolov, I.; Parmigiani, F.; Penco, G.; Raimondi, L.; Rebernik, P.; Rossi, F.; Roussel, E.; Scafuri, C.; Serpico, C.; Sigalotti, P.; Spezzani, C.; Svandrlik, M.; Svetina, C.; M, T.; Veronese, M.; Zangrando, D.; Zangrando, M. The FERMI Free-Electron Lasers. *J. Synchrotron Radiat.* **2015**, *22* (3), 485–491.

(12) Mueller, B. Y.; Rethfeld, B. Relaxation Dynamics in Laser-Excited Metals under Nonequilibrium Conditions. *Phys. Rev. B* **2013**, *87* (3), 035139.

(13) Rethfeld, B.; Kaiser, A.; Vicanek, M.; Simon, G. Ultrafast Dynamics of Nonequilibrium Electrons in Metals under Femtosecond Laser Irradiation. *Phys. Rev. B* **2002**, *65* (21), 214303.

(14) Rettie, A. J. E.; Chemelewski, W. D.; Emin, D.; Mullins, C. B. Unravelling Small-Polaron Transport in Metal Oxide Photoelectrodes. *J. Phys. Chem. Lett.* **2016**, *7* (3), 471–479.

(15) Tang, H.; Bai, M.; Dou, Y.; Ran, Q.; Lo, G. V. Computer Simulations of Laser-Induced Melting of Aluminum. *Nucl. Instrum. Methods Phys. Res. Sect. B Beam Interact. Mater. At.* **2013**, *301*, 36–40.

(16) Sonntag, S.; Roth, J.; Gaehler, F.; Trebin, H.-R. Femtosecond Laser Ablation of Aluminium. *Appl. Surf. Sci.* **2009**, *255* (24), 9742–9744.

(17) Winter, J.; Rapp, S.; Spellauge, M.; Eulenkamp, C.; Schmidt, M.; Huber, H. P. Ultrafast Pump-Probe Ellipsometry and Microscopy Reveal the Surface Dynamics of Femtosecond Laser Ablation of Aluminium and Stainless Steel. *Appl. Surf. Sci.* **2020**, *511*, 145514.

(18) Roth, J.; Sonntag, S.; Karlin, J.; Paredes, C. T.; Sartison, M.; Krauß, A.; Trebin, H.-R. Molecular Dynamics Simulations Studies of Laser Ablation in Metals. *AIP Conf. Proc.* **2012**, *1464* (1), 504–523.

(19) Okazaki, M.; Furube, A.; Chen, L.-Y. Charge Generation Dynamics in Hematite Photoanodes Decorated with Gold Nanostructures under Near Infrared Excitation. *J. Chem. Phys.* **2020**, *152* (4), 041106.

(20) Dong, L.; Chu, H.; Li, Y.; Zhao, S.; Li, G.; Li, D. Nonlinear Optical Responses of α-Fe_2O_3 Nanosheets and Application as a Saturable Absorber in the Wide Near-Infrared Region. *Opt. Laser Technol.* **2021**, *136*, 106812.

(21) Klein, I. M.; Liu, H.; Nimlos, D.; Krotz, A.; Cushing, S. K. *Ab Initio* Prediction of Excited-State and Polaron Effects in Transient XUV Measurements of α-Fe_2O_3. *J. Am. Chem. Soc.* **2022**, *144* (28), 12834–12841.

(22) Shimojo, F.; Nakano, A.; Kalia, R. K.; Vashishta, P. Electronic Processes in Fast Thermite Chemical Reactions: A First-Principles Molecular Dynamics Study. *Phys. Rev. E* **2008**, *77* (6), 066103.

(23) Masciovecchio, C.; Battistoni, A.; Giangrisostomi, E.; Bencivenga, F.; Principi, E.; Mincigrucci, R.; Cucini, R.; Gessini, A.; D'Amico, F.; Borghes, R.; Prica, M.; Chenda, V.; Scarcia, M.; Gaio, G.; Kurdi, G.; Demidovich, A.; Danailov, M. B.; Di Cicco, A.; Filipponi, A.; Gunnella, R.; Hatada, K.; Mahne, N.; Raimondi, L.; Svetina, C.; Godnig, R.; Abrami, A.; Zangrando, M. EIS: The Scattering Beamline at FERMI. *J. Synchrotron Radiat.* **2015**, *22* (3), 553–564.

(24) Yu, L.-H.; Babzien, M.; Ben-Zvi, I.; DiMauro, L. F.; Doyuran, A.; Graves, W.; Johnson, E.; Krinsky, S.; Malone, R.; Pogorelsky, I.; Skaritka, J.; Rakowsky, G.; Solomon, L.; Wang, X. J.; Woodle, M.; Yakimenko, V.; Biedron, S. G.; Galayda, J. N.; Gluskin, E.; Jagger, J.; Sajaev, V.; Vasserman, I. High-Gain Harmonic-Generation Free-Electron Laser. *Science* **2000**, *289* (5481), 932–934.

(25) Cinquegrana, P.; Demidovich, A.; Kurdi, G.; Nikolov, I.; Sigalotti, P.; Susnjar, P.; Danailov, M. B. The Seed Laser System of the FERMI Free-Electron Laser: Design, Performance and near Future Upgrades. *High Power Laser Sci. Eng.* **2021**, *9*, e61.

(26) Cinquegrana, P.; Cleva, S.; Demidovich, A.; Gaio, G.; Ivanov, R.; Kurdi, G.; Nikolov, I.; Sigalotti, P.; Danailov, M. B. Optical Beam Transport to a Remote Location for Low Jitter Pump-Probe Experiments with a Free Electron Laser. *Phys. Rev. ST Accel. Beams* **2014**, *17* (4), 040702.

(27) Danailov, M. B.; Bencivenga, F.; Capotondi, F.; Casolari, F.; Cinquegrana, P.; Demidovich, A.; Giangrisostomi, E.; Kiskinova, M. P.; Kurdi, G.; Manfredda, M.; Masciovecchio, C.; Mincigrucci, R.; Nikolov, I. P.; Pedersoli, E.; Principi, E.; Sigalotti, P. Towards Jitter-Free Pump-Probe Measurements at Seeded Free Electron Laser Facilities. *Opt. Express* **2014**, *22* (11), 12869–12879.

(28) Svetina, C.; Cocco, D.; Mahne, N.; Raimondi, L.; Ferrari, E.; Zangrando, M. PRESTO, the on-Line Photon Energy Spectrometer at FERMI: Design, Features and Commissioning Results. *J. Synchrotron Radiat.* **2016**, *23* (1), 35–42.

(29) Principi, E.; Svetina, C.; De Angelis, D.; Fava, C.; Mincigrucci, R.; Foglia, L.; Simoncig, A.; Manfredda, M.; Mahne, N.; Gobessi, R.; Scarcia, M.; Gessini, A.; Bencivenga, F.; Capotondi, F.; Zangrando, M.; Masciovecchio, C. A Versatile Wide Energy Range Spectrometer for Soft X-Ray FELs. *Nucl. Instrum. Methods Phys. Res. Sect. A Accel. Spect. Detectors Assoc. Equip.* **2024**, *1058*, 168856.

(30) Vinson, J. Advances in the OCEAN-3 Spectroscopy Package. *Phys. Chem. Chem. Phys.* **2022**, *24* (21), 12787–12803.

(31) Vinson, J.; Rehr, J. J.; Kas, J. J.; Shirley, E. L. Bethe-Salpeter Equation Calculations of Core Excitation Spectra. *Phys. Rev. B* **2011**, *83* (11), 115106.

(32) Giannozzi, P.; Baroni, S.; Bonini, N.; Calandra, M.; Car, R.; Cavazzoni, C.; Ceresoli, D.; Chiarotti, G. L.; Cococcioni, M.; Dabo, I.; Corso, A. D.; Gironcoli, S. de; Fabris, S.; Fratesi, G.; Gebauer, R.; Gerstmann, U.; Gougoussis, C.; Kokalj, A.; Lazzeri, M.; Martin-Samos, L.; Marzari, N.; Mauri, F.; Mazzarello, R.; Paolini, S.; Pasquarello, A.; Paulatto, L.; Sbraccia, C.; Scandolo, S.; Sclauzero, G.; Seitsonen, A. P.; Smogunov, A.; Umari, P.; Wentzcovitch, R. M. QUANTUM ESPRESSO: A Modular and Open-Source Software Project for Quantum Simulations of Materials. *J. Phys.: Condens. Matter* **2009**, *21* (39), 395502.

(33) Perdew, J. P.; Burke, K.; Ernzerhof, M. Generalized Gradient Approximation Made Simple. *Phys. Rev. Lett.* **1996**, *77* (18), 3865–3868.

(34) Vinson, J.; Kas, J. J.; Vila, F. D.; Rehr, J. J.; Shirley, E. L. Theoretical Optical and X-ray Spectra of Liquid and Solid H_2O. *Phys. Rev. B* **2012**, *85* (4), 045101.

(35) Vinson, J.; Jach, T.; Müller, M.; Unterumsberger, R.; Beckhoff, B. Quasiparticle Lifetime Broadening in Resonant X-ray Scattering of NH_4NO_3. *Phys. Rev. B* **2016**, *94* (3), 035163.

(36) van Aken, P. A.; Styrsa, V. J.; Liebscher, B.; Woodland, A. B.; Redhammer, G. J. Microanalysis of $Fe^{3+}/\Sigma Fe$ in Oxide and Silicate Minerals by Investigation of Electron Energy-Loss near-Edge Structures (ELNES) at the Fe $M_{2,3}$ Edge. *Phys. Chem. Miner.* **1999**, *26* (7), 584–590.

(37) Hamann, D. R. Optimized Norm-Conserving Vanderbilt Pseudopotentials. *Phys. Rev. B* **2013**, *88* (8), 085117.

(38) Feldhoff, A.; Pippel, E.; Wolterdorf, J. Interface Engineering of Carbon-Fiber Reinforced Mg–Al Alloys. *Adv. Eng. Mater.* **2000**, *2* (8), 471–480.

Appendix B

SUPPLEMENTARY INFORMATION FOR NONEQUILIBRIUM RESHAPING OF THE SILICON BULK PLASMON UNDER DENSE PHOTOEXCITATION

B.1 Electronic Structure of Silicon

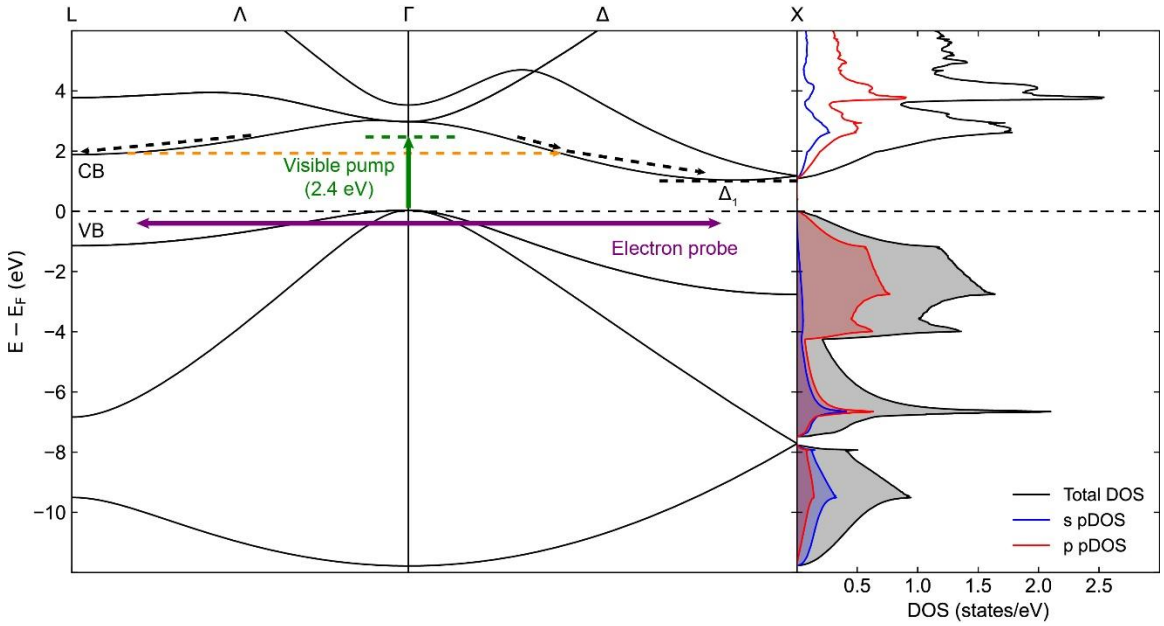

Figure B.1. Band structure (left) and projected density of states (right) for Si calculated by density functional theory calculations. The visible pump pulse (green arrows) excites electrons into the conduction band leaving holes in the valence band. Before becoming a quasi-equilibrium hot electron distribution, the photoexcited electrons undergo L-to-X intervalley scattering (yellow dashed arrow) and relaxation towards the conduction band minimum (black dashed arrows). The electron probe (purple arrows) measures bulk plasmon excitations.

B.2 Electron-Beam Induced Carrier Generation

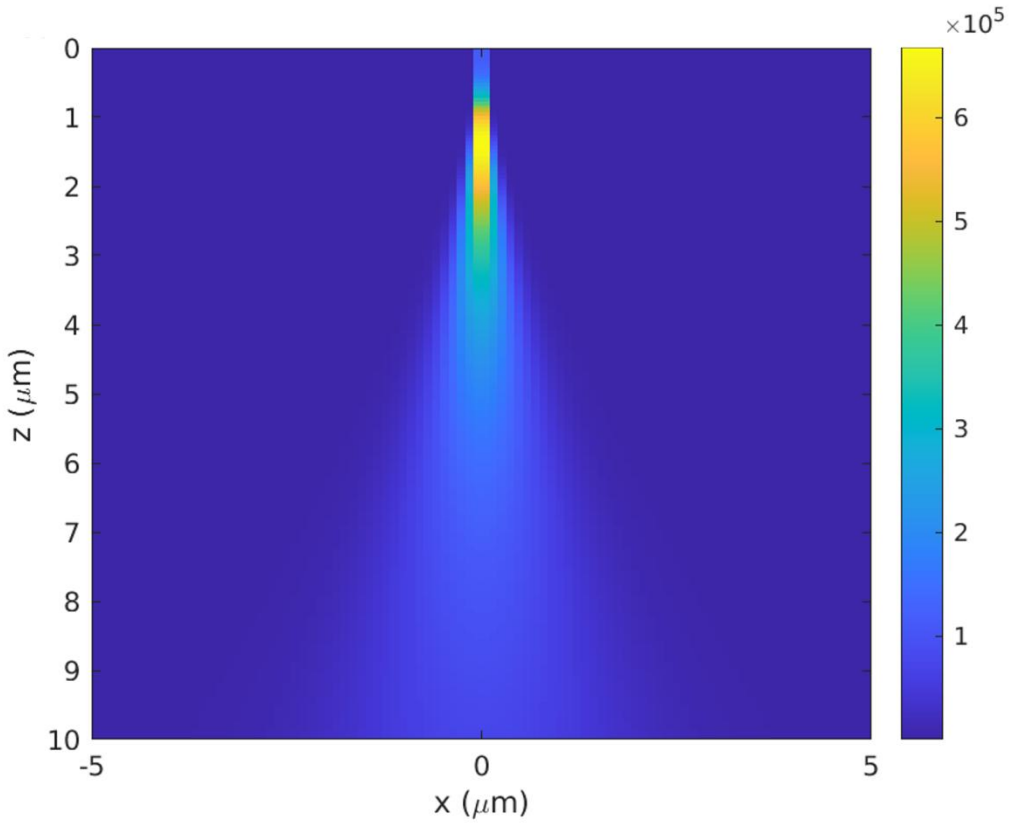

Figure B.2. Spatial distribution of electron–hole pair generation in silicon as a function of x-z position for a 50 nm diameter electron beam operated at an acceleration voltage of 200 kV and beam current of 4.8 fA.

B.3 Photoexcited Carrier Density

The density of photoexcited carriers was estimated using

$$\Delta n = \frac{F}{\hbar\omega}\frac{1-R}{L}(1-e^{-\alpha L})(1+Re^{-\alpha L}) = 9.2\times 10^{20}\ \text{cm}^{-3} \qquad (B.1)$$

where F is the pump fluence (50 mJ/cm^2), $\hbar\omega$ is the pump energy (2.4 eV), R and α are reflectivity and absorption coefficient of silicon at 515 nm, respectively, with values of 0.38 and 9.3 × 10^3 cm^{-1}. The values were obtained by interpolating data reported in Ref. 1.

B.4 Peak Fitting Analysis

Peak positions were determined by fitting the spectra using Gaussian, Lorentzian, and Voigt line-shape functions, depending on the spectral feature interest.

For zero-loss peak (ZLP) fitting, the reduced chi-square values obtained from Voigt, Lorentzian, and Gaussian were 20.164, 48.610, and 63.673, respectively, indicating that the Voigt profile provided the best agreement with the experimental data. Similarly, plasmon peak fitting yielded reduced chi-square values of 0.69606 for the Voigt fit, 0.62316 for the Lorentzian fit, and 7.7913 for the Gaussian fit. These results indicate that Lorentzian and Voigt profiles describe the plasmon resonance significantly better than a purely Gaussian function, consistent with the intrinsic lifetime broadening of the plasmon excitation. Therefore, the Voigt and Lorentzian functions were used to fit the ZLP and bulk plasmon peaks, respectively, for accurate determination of the peak positions and linewidths.

B.5 References

(1) Green, M. A.; Keevers, M. J. Optical Properties of Intrinsic Silicon at 300 K. *Prog. Photovolt.: Res. Appl.* **1995**, *3* (3), 189–192. https://doi.org/10.1002/pip.4670030303.

Appendix C

SUPPLEMENTARY INFORMATION FOR ELECTRONIC TOPOLOGICAL TRANSITIONS IN CADMIUM UNDER PRESSURE STUDIED VIA THEORETICAL AND EXPERIMENTAL X-RAY ABSORPTION SPECTROSCOPY

C.1 X-ray Diffraction Setup

This beam profile corresponds to one of the x-ray diffraction (XRD)/x-ray absorption spectroscopy (XAS) experiments. A similar procedure was applied to a second set of XRD/XAS experiments. The combined XAS/XRD experiments were conducted at Sector 16-BMD using the following energies: 21.04 keV (Technetium (Tc) K-edge), 25.0 keV (XRD), and 26.7 keV (Cadmium (Cd) K-edge). The beam profile was optimized at 23 keV and confirmed to maintain its shape consistently across this energy range. The incident beam was focused using a pair of vertical and horizontal Kirkpatrick-Baez (KB) mirrors that are coated with platinum (Pt) film and set at 1.8 mrad incident and reflection angles. The condition corresponds to about 45 keV cut-off energy for higher-harmonics rejection. As the 3rd higher harmonics of Si(111) monochromator for Cd K-edge energy (26.711 keV) would be about 80 keV, which is far above the 45 keV cut-off energy, practically there would be no effect of this higher harmonics on the current measurement. Data were collected in two separate runs using different detectors: the October 2021 dataset employed a Mar165 CCD detector, while the April 2022 dataset used a Pilatus3 X CdTe 1M detector.

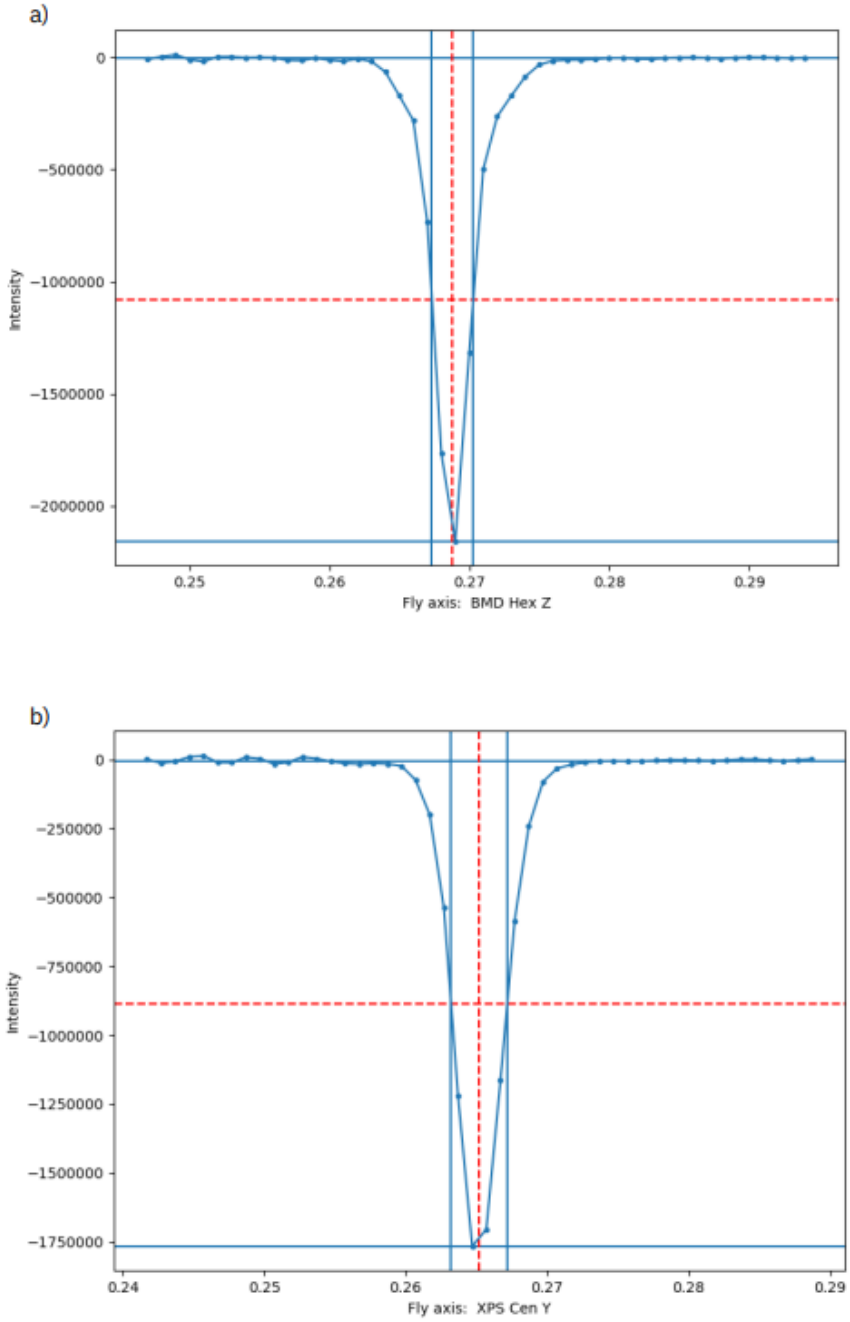

Figure C.1. Characterization of beam profile. (a) Vertical beam profile (no pinhole): Full width at half maximum (FWHM) = 3 μm; Full width at <1% max. = 19 μm. **(b)** Horizontal beam profile: FWHM = 4 μm; Full width at <1% max. = 20 μm.

a)

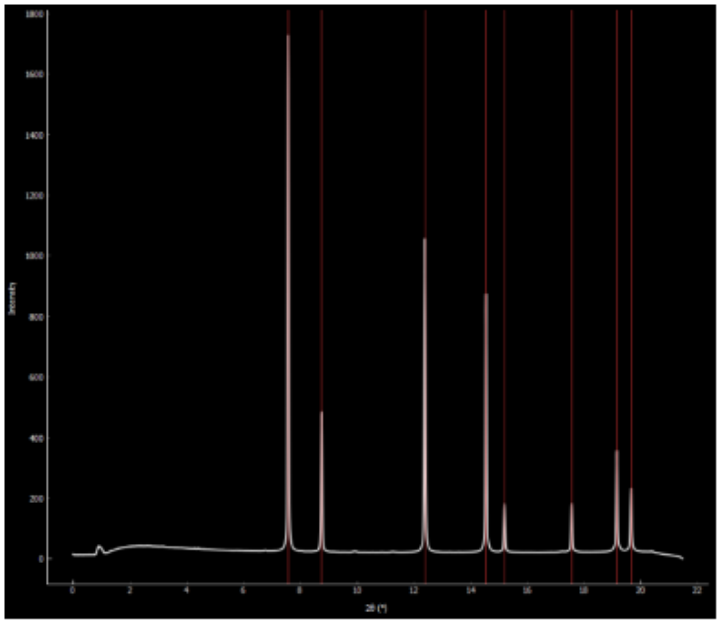

b)

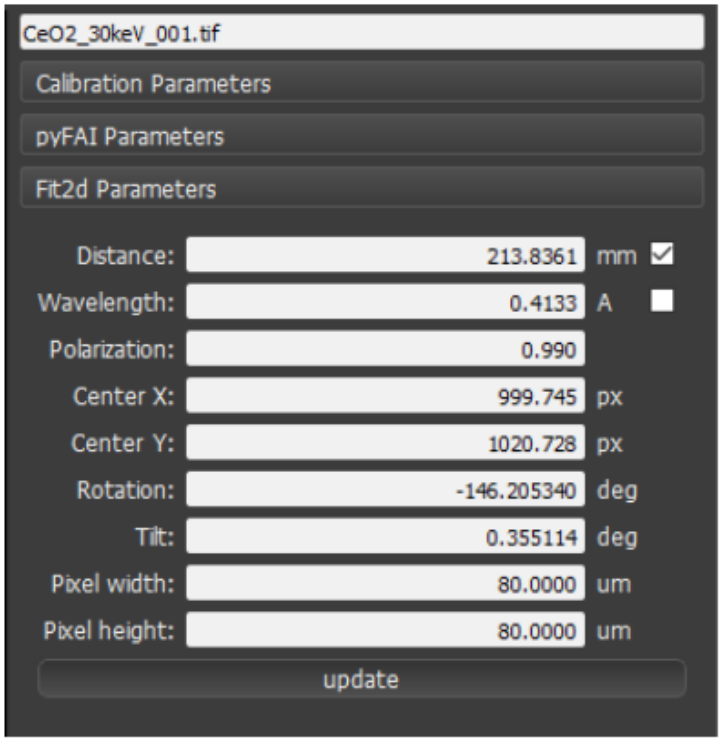

Figure C.2. Calibration setup for the Mar165 CCD detector at E = 30 keV. (a) Calibration curve and **(b)** associated numerical parameters.

C.2 Lattice Parameter and Volume Data from XRD

Table C.I. Table of lattice parameters and volumes extracted via Le Bail refinement on XRD patterns of Cd.

Name	Pressure (GPa)	a (Å)	c (Å)	V (Å^3/unit cell)
Energy Standard 2*	0	2.9798(3)	5.635(1)	43.332(7)
Energy Standard 2*	0	2.9805(3)	5.622(1)	43.248(7)
Energy Standard 1*	0	2.9809(1)	5.609(2)	43.16(2)
Sample 3 P0*	0.2(1)	2.9778(2)	5.58069()	42.858(5)
Sample 2 P0*	0.8(1)	2.9714(2)	5.5369(9)	42.335(5)
Sample 2 P1*	1.0(3)	2.9697(3)	5.520(1)	42.163(8)
Sample 2 P2*	1.3(1)	2.9669(3)	5.490(1)	41.858(7)
Sample 2 P3*	2.1(1)	2.9596(4)	5.443(1)	41.289(6)
Sample 2 P4*	3.0(1)	2.9546(2)	5.4003(4)	40.826(3)
Sample 2 P5*	3.8(1)	2.9501(6)	5.3488(4)	40.316(9)
Sample 2 P6*	4.5(1)	2.946(1)	5.3096(5)	39.91(2)
Sample 1 P0*	4.6(1)	2.9480(1)	5.3264(3)	40.089(2)
Sample 1 P1*	5.1(2)	2.9391(2)	5.2727(8)	39.444(3)
Sample 1 P2*	6.4(2)	2.93366(6)	5.2320(2)	38.997(1)
Sample 1 P3*	8.0(1)	2.9232(5)	5.1606(2)	38.191(1)
Sample 1 P4	8.4(1)	2.92081(6)	5.1513(2)	38.059(1)
Sample 1 P5	9.3(1)	2.91615(9)	5.1224(2)	37.724(1)
Sample 1 P6*	9.9(3)	2.91473(6)	5.1085(1)	37.586(1)
Sample 1 P7*	10.9(1)	2.90899(5)	5.0830(1)	37.251(1)
Sample 1 P8	12.1(1)	2.9027(1)	5.0363(5)	36.749(2)
Sample 1 P9*	13.3(3)	2.8969(1)	5.0176(3)	36.467(1)
Sample 1 P10	13.6(2)	2.89465(5)	5.0068(2)	36.331(1)
Sample 1 P11	14.3(1)	2.89002(6)	4.9955(3)	36.133(1)
Sample 1 P12*	16.0(3)	2.88344(5)	4.9615(2)	35.725(1)
Sample 1 P13	17.1(1)	2.87778(5)	4.9293(2)	35.353(1)
Sample 1 P14	18.2(1)	2.87279(6)	4.9089(2)	35.085(1)
Sample 1 P15	19.3(1)	2.86765(6)	4.8834(2)	34.778(1)
Sample 1 P16*	20.8(4)	2.86326(6)	4.8616(3)	34.517(2)
Sample 1 P17	21.2(1)	2.86080(5)	4.8558(2)	34.417(1)
Sample 1 P18	22.0(1)	2.85753(6)	4.8413(2)	34.236(1)
Sample 1 P19	22.9(1)	2.85411(5)	4.8244(2)	34.034(1)
Sample 1 P20*	24.3(2)	2.85007(5)	4.8084(2)	33.825(1)
Sample 1 P21	25.3(1)	2.84533(5)	4.7898(2)	33.582(1)

Points marked with * indicate that XAS data were also taken at that pressure point. Some XAS points do not have corresponding XRD.

C.3 Sample Photos and Measurements

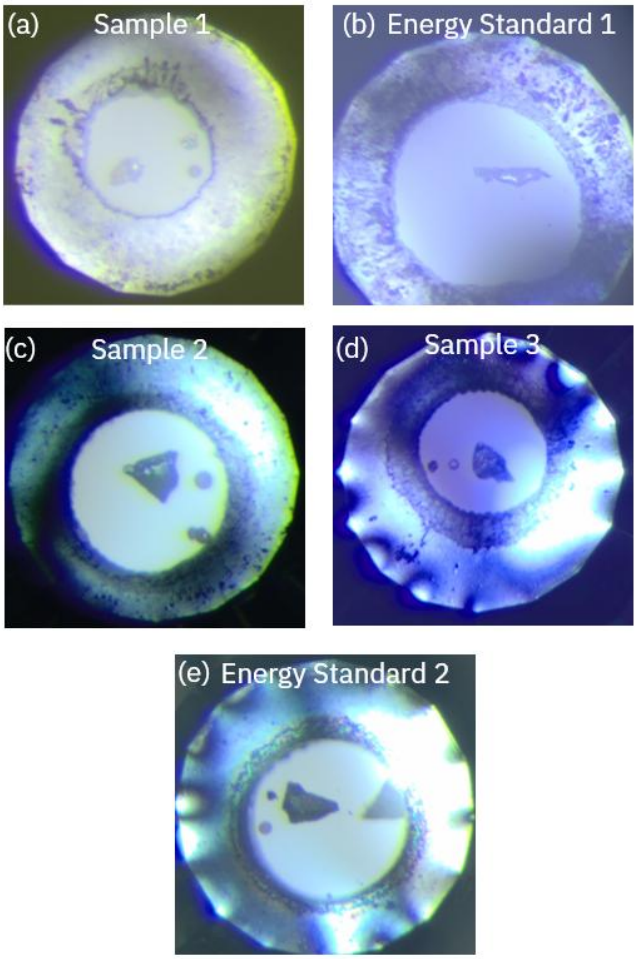

Figure C.3. Photos of samples used in XRD and XAS experiments at 16-BMD at HPCAT;[1] Cd in helium (He) with beryllium (Be) gasket, ruby and gold (Au). All samples have a path that matches the absorption length of Cd. Each caption consists of the internal naming convention of diamond anvil cells (DACs) followed by the sample dimensions. **(a)**: Sample 1, Cd on left-hand side (21–23 μm thick in north to south orientation), Au (12 μm) and ruby (15 μm) on right-hand side. 250 μm culets. **(b)**: Energy Standard 1, Cd only (20–30 μm thick through center). 500 μm culets. **(c)**: Sample 2, (300 μm culets), Cd piece is 62 μm in length through the middle, and the width (north to south) is 55 μm. Ruby is to the right and is about 20 μm while Au is below that at about 19 μm. **(d)**: Sample 3 (400 μm culets), Cd piece (65 μm in length and 49 μm in height on left-hand

side), ruby is to the left of Cd and is about 18 μm, Au is on the farthest left and is about 19 μm. **(e)**: Energy Standard 2, (500 μm culets), two pieces of Cd (left-hand side piece used in experiments is 95 μm in length and 70 μm wide), one piece of Au (19 μm) and a ruby (21 μm).

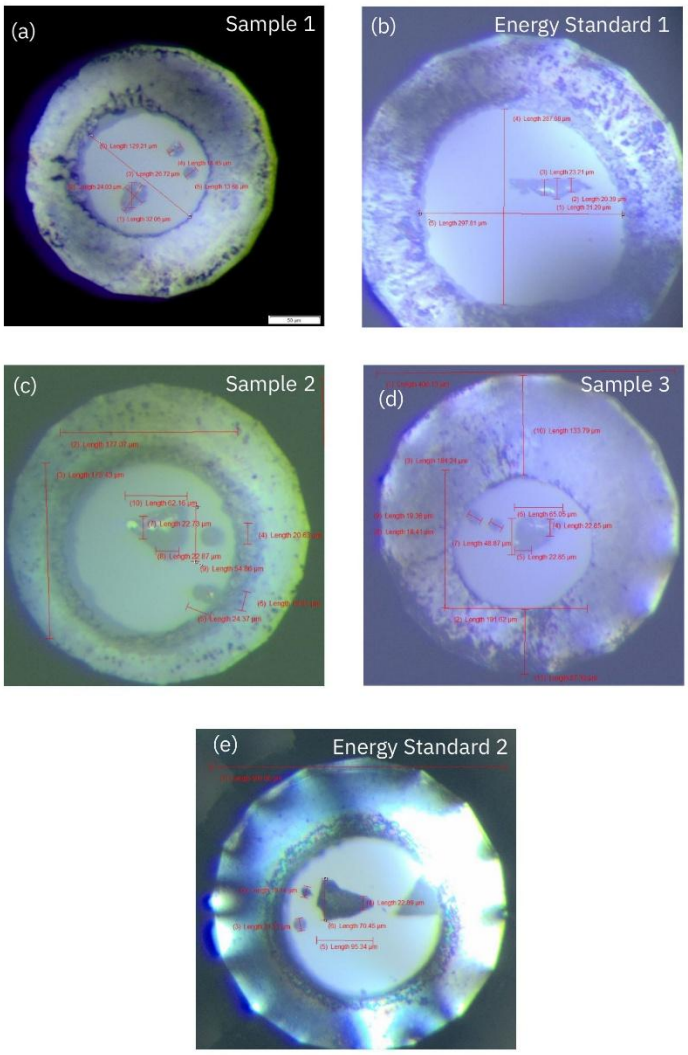

Figure C.4. Same information as the previous figure, now with measurement data included.

C.4 Cross-Sectional X-ray Absorption Maps of DAC Samples

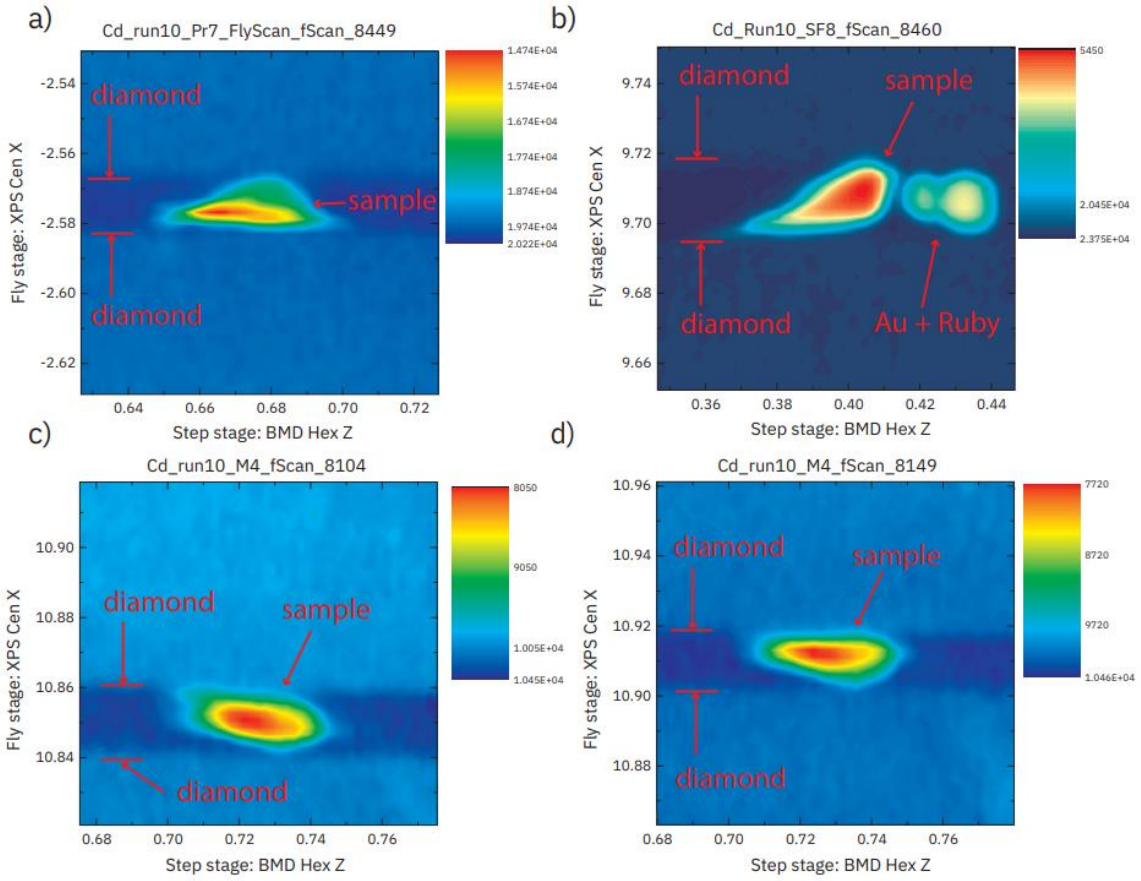

Figure C.5. Cross-sectional x-ray absorption maps of the sample acquired during XRD/XAS experiments at 16-BMD (HPCAT).[1] Panel **(a)** corresponds to Energy Standard 2, **(b)** to Sample 2, and **(c)**–**(d)** to Sample 3. Panel **(c)** was collected early in the experiment, while **(d)** was obtained later at the highest pressures. These maps were used to assess potential sample bridging; no evidence of bridging was observed.

C.5 Raw XRD Patterns, Azimuthal View, and Refinements

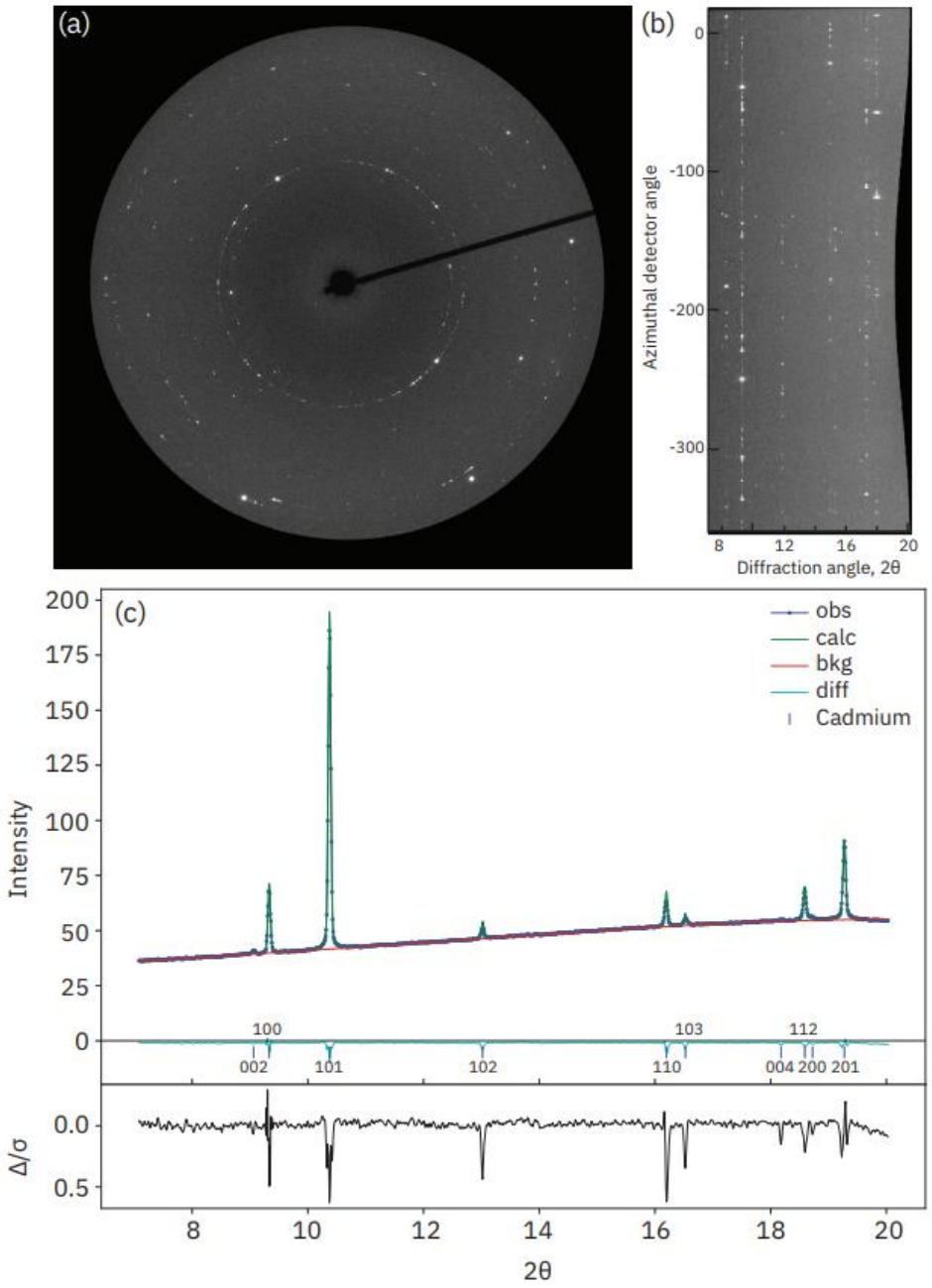

Figure C.6. Raw XRD data and refinement for Sample 1 at 6.4(2) GPa. (a) Raw diffraction pattern, **(b)** cake plot with azimuthal binning, and **(c)** refinement performed using GSASII.

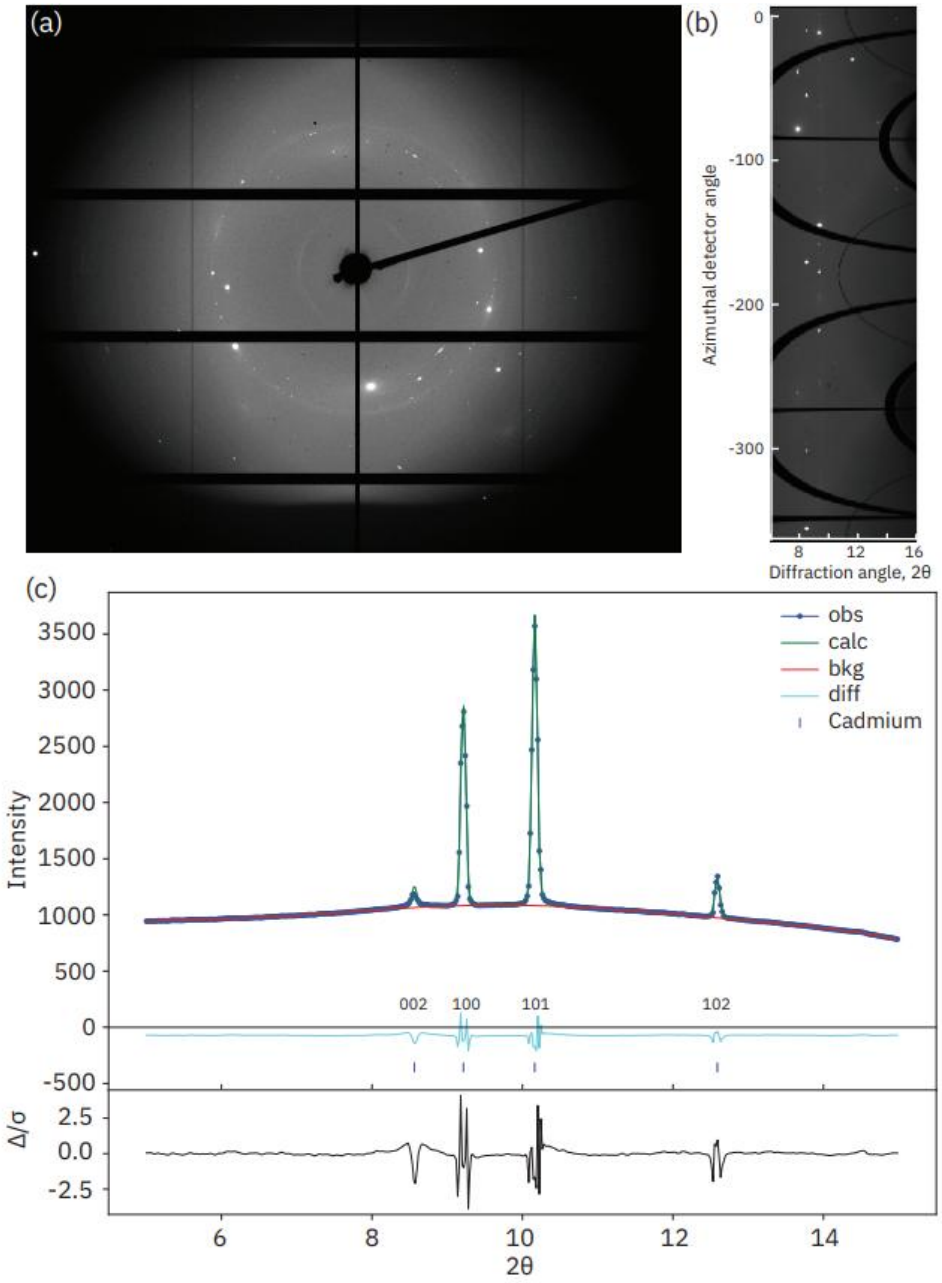

Figure C.7. Raw XRD data and refinement for Sample 2 at 0.8(1) GPa. (a) Raw diffraction pattern, **(b)** cake plot with azimuthal binning, and **(c)** refinement performed using GSASII.

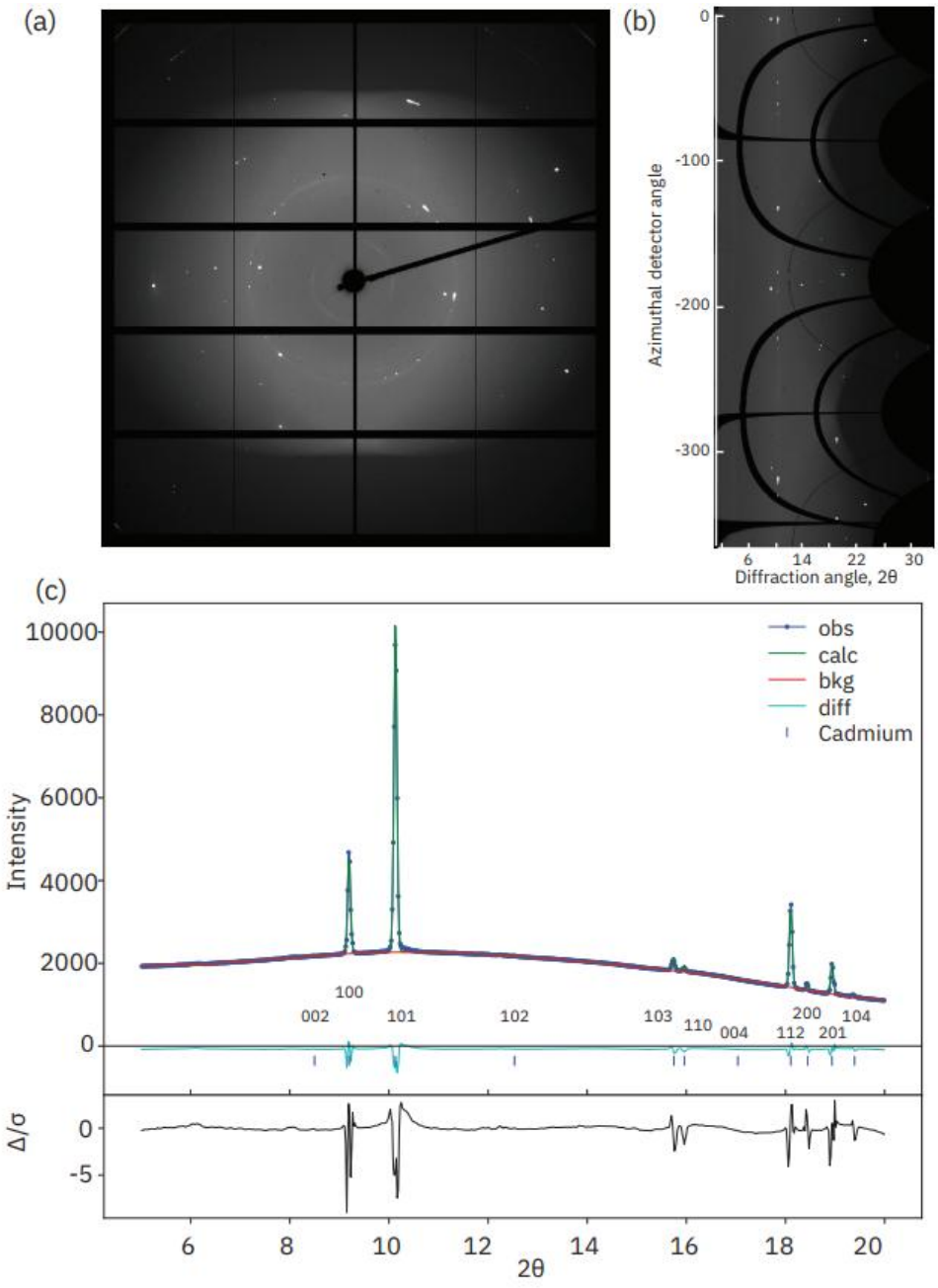

Figure C.8. Raw XRD data and refinement for Sample 3 at 0.2(1) GPa. (a) Raw diffraction pattern, **(b)** cake plot with azimuthal binning, and **(c)** refinement performed using GASAII. While the XRD data quality for this sample was initially reasonable, subsequent measurements were limited by a sample mounting configuration that made reliable diffraction collection challenging. As a result, Sample 3 was primarily relied on

XAS where axial access remained available and measurements were more reliable. Additionally, Sample 3 underwent pressure cycling prior to the experiment, including gas loading at ~0.3 GPa, compression above 1.8 GPa, and decompression back to ~0.3 GPa, followed by additional cycling during the experiment. Further details on the XAS measurements for Sample are provided in **Figs. C.16** and **C.17**.

C.6 Structural Data Graphs (P-V Plot and P vs *a* and *c*)

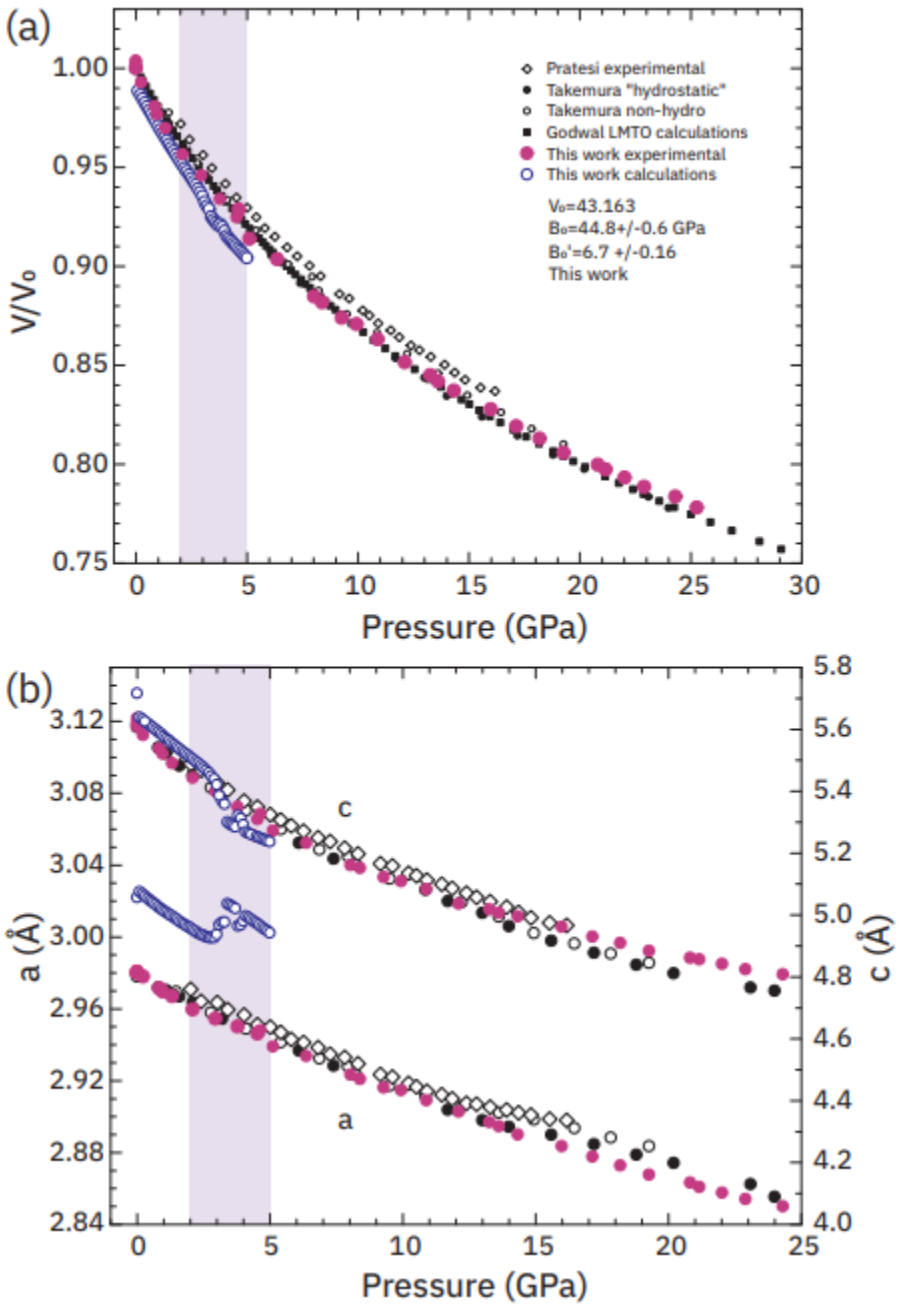

Figure C.9. Additional representation of structural data for Cd collected via XRD. The highlighted region corresponds to the same pressure range shown in **Chapter 3** (approximately 3–5 GPa). **(a)** Pressure dependence of normalized volume (V/V_0). **(b)** Pressure dependence of lattice parameters *a* (left axis) and *c* (right axis).

C.7 Discussion of the XAS Setup and Verification of Monochromator Energy Calibration

Due to the confined geometry of the combined XRD–XAS setup, there is no space to accommodate an additional downstream reference ion chamber after the sample. The photographs in **Fig. C.10** were taken in 2015, when the diffraction detector in use was a MAR345 image plate, which has since been replaced by a Pilatus3 X CdTe 1M detector. X-ray absorption measurements are performed using two ion chambers filled with flowing argon (Ar) gas at slightly above atmospheric pressure. Owing to spatial constraints, the upstream ion chamber has an active thickness of only 10 mm, which necessitates repeated measurements to improve counting statistics.

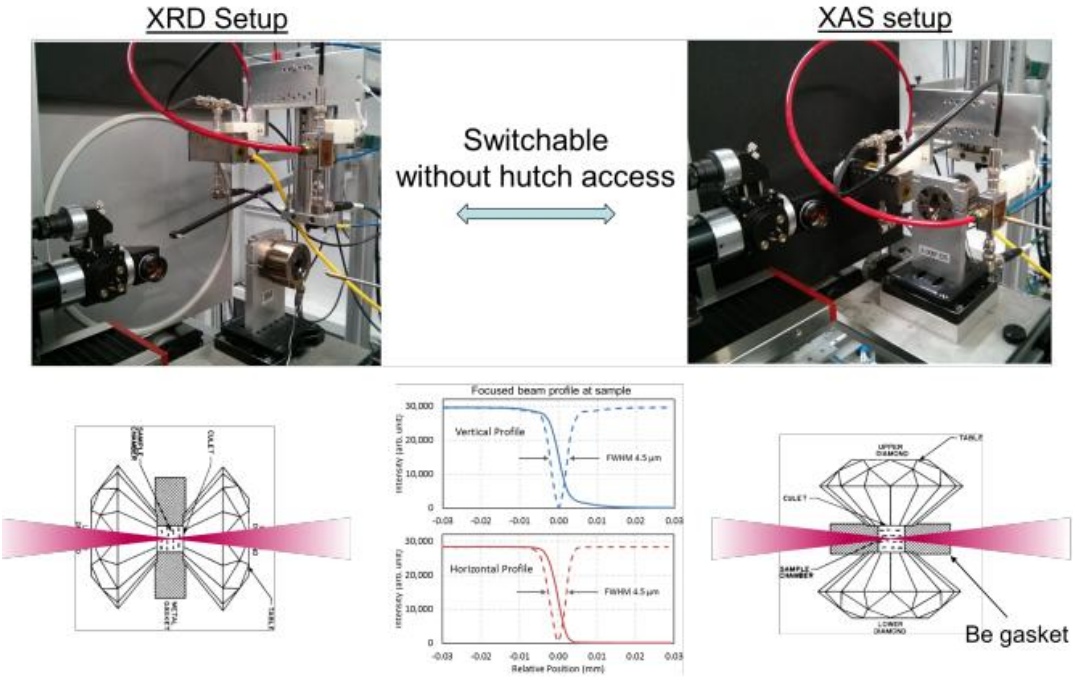

Figure C.10. XRD and XAS experimental setup, showing the axial and radial measurement geometries, respectively.

Although simultaneous energy calibration is not performed during measurements, the monochromator is equipped with a positional encoder that enables energy calibration based

on absolute position information. A more detailed description of the beamline energy calibration procedure can be found in Park *et al*.[1] The encoder-based calibration has been demonstrated to be reproducible over several years of operation at the beamline.

As the sample is a pure metal, it can be used as an internal reference to verify the consistency of the energy calibration across measurements. **Figure C.11** presents normalized x-ray absorption spectra of the Cd sample in a DAC, measured repeatedly to improve counting statistics, along with their corresponding first derivatives. The spectra were collected at the same pressure condition, both before compression and after decompression. After 60 hours from the initial dataset and following a full compression–decompression cycle, the two spectra show identical E_0 positions. Small fluctuations in energy calibration (on the order of 0.1–0.5 eV, not shown) are attributed to potential heat accumulation in the monochromator motor during repeated scans; however, these variations are negligible compared to the observed energy shifts and spectral changes reported in this work.

Since the data were merged and averaged, some smearing of the spectral resolution may occur; however, this is an accepted trade-off for improved counting statistics. A discrepancy in the E_0 position relative to the theoretical value was also observed, as Cd was not independently included in the initial energy calibration procedure described in Park *et al*.[1] This offset was subsequently corrected during post-experiment data analysis. The caption of **Fig. C.11** further includes a brief description of the beam size and notes potential diamond-related glitches arising from the reduced gap between the two diamond anvils following compression.

Despite these limitations, the comparison presented in **Fig. C.11** confirms the reproducibility of the energy calibration over the experimental timescale, the stability of the monochromator for XAS measurements, and the ability of the sample to yield consistent, reproducible spectral features. Additional sample comparisons leading to the same conclusions are omitted for brevity.

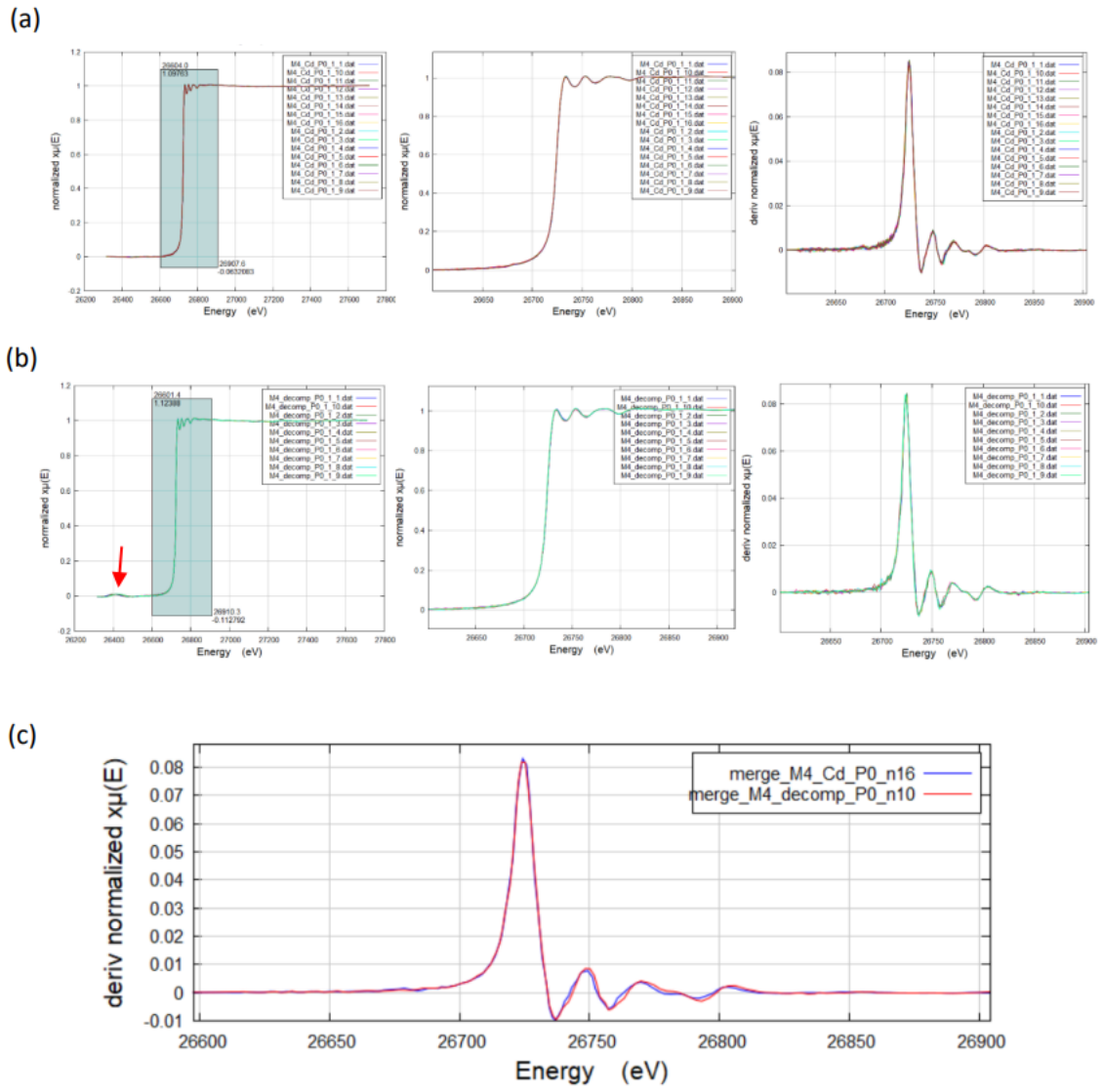

Figure C.11. Reproducibility of Cd x-ray absorption spectra and energy calibration stability across compression–decompression cycles. (a) Normalized x-ray absorption spectra of Cd Sample 3 (M4) at ambient pressure (P_0 = 0.2 GPa), measured 16 times and their corresponding derivatives. The full energy range spans E_0 − 400 eV to E_0 + 980 eV to ensure reliable pre-edge and post-edge normalization. All 16 spectra were merged to improve counting statistics. The apparent absorption edge position (E_0 = 26.724 keV) is shifted by +13 eV relative to the theoretical value (E_0 = 26.711 keV), which was corrected during post-experiment data analysis. **(b)** Normalized absorption spectra of Cd Sample 3 (M4) at P_0 = 0.2 GPa during the decompression sequence, measured 10 times. The red

arrow highlights a hump caused by diamond glitches. This artifact indicates a change in the DAC condition relative to the initial state, likely due to a reduced anvil gap following compression. Given the ~5 μm FWHM beam size in radial transmission geometry,[1] the post-compression anvil separation is sufficiently reduced that the beam may interact with the edges of the diamond anvils, introducing the observed artifacts. These diamond glitches were not present in the initial uncompressed measurements shown in **(a)**. **(c)** Comparison of the merged normalized absorption spectra of Cd in their derivatives between P_0 and P_0 decompression conditions. The two measurements were separated by more than 60 hours of time. The consistent E_0 position from these two measurements confirms the mechanical stability of monochromator over typical experimental time frames and reproducibility of measurements. The subtle differences above the absorption edge indicate the history of the sample over the compression and decompression process, which should be subject to detailed study.

C.8 EXAFS Analysis and Discussion

Extended x-ray absorption fine structure (EXAFS) data were fit using the Artemis software package. E_0 was defined as the zero of the second derivative of the white line and was allowed to be fit as a single variable across all pressures. S_0^2 was treated as a singularly as global parameter for the fits, and backgrounds were also fit. The initial guess parameters used were $\Delta E = 0$, $\Delta r = 0.01$, and mean squared relative displacement (MSRD) = 0.001 for each data point. Δr is taken relative to the ambient condition coordination length and ΔE is relative to the second derivative of the white line defined during data reduction. For each pressure, the half-path length and MSRD were fit to the first scattering shell (**Fig. C.12(a)**). Bond distance is also extracted and shown in **Fig. C.12(b)**. Sample 3 and Sample 1 points follow expected trend of reporting coordination lengths greater than observed from XRD (black) while points from Sample 2 are less than the crystallographic coordination lengths. This is an unexpected behavior, due to the way the half path length in EXAFS is defined as the crystallographic equilibrium distance between scatters plus the instantaneous displacement of the atoms, a value that is always positive.

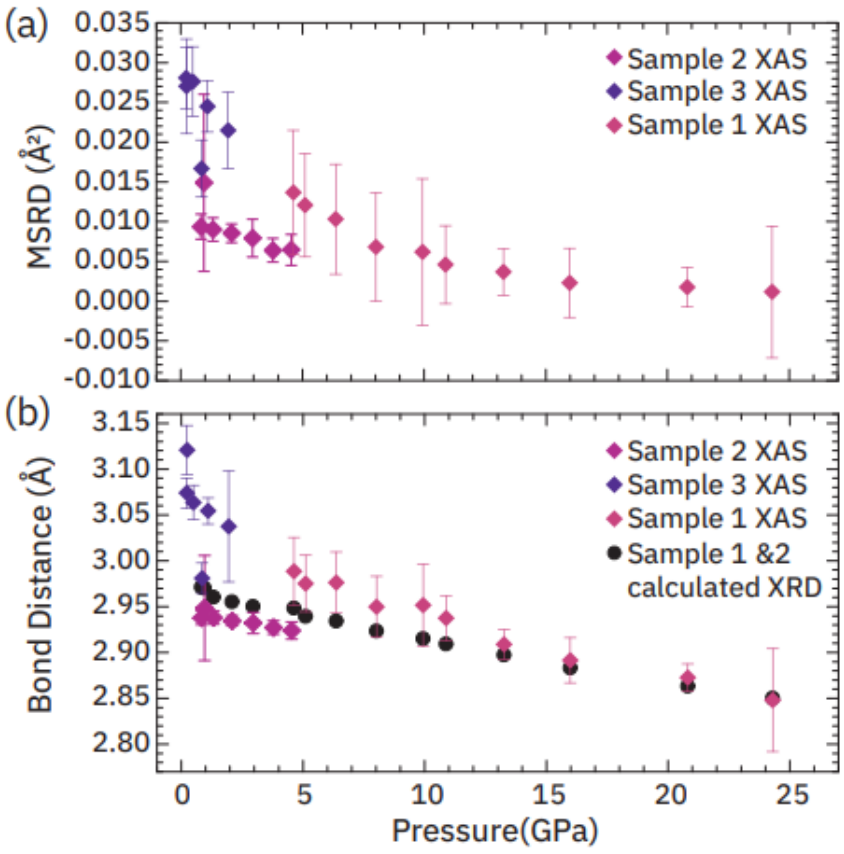

Figure C.12. EXAFS-derived structural parameters for Cd. (a) MSRD and **(b)** bond distance as a function of pressure.

The quality of data in the EXAFS region was non-uniform from sample to sample. Some samples had clear oscillations in k-space up to 9 $Å^{-1}$ while some only clear oscillations to about 6.75 $Å^{-1}$. The fitting window for EXAFS analysis was determined by the sample with the most limited k-space window, which was then applied to the full data set for uniform consistency. For the analysis of this work, spectra were Fourier transformed from a k-space window of 2.8 to 8 $Å^{-1}$ and then fit in R-space using a window from 2 to 3.5 Å for consistency throughout runs and best fit. This results in very coarse resolution in real space as the real space step size is about equal to $\pi/2k$, in this case, 0.302 Å. Using a smaller k-space window to accommodate for the variation in quality of EXAFS data from sample to sample results in lower resolution for the whole data set than if points were fit with individually maximized

windows; however, it allows for a more direct comparison of data points at multiple pressures, as the fits were performed using identical windows across all samples in the data set. It is not uncommon to treat each XAS scan as an independent point; however, in this work, we prioritized analytical consistency across multiple samples for comparison of data points over improved individual data point resolution.

Table C.II. EXAFS analysis results (reproduced from Fig. C.12). Points marked with * indicate if XRD data were taken for that pressure.

Name	Pressure (GPa)	MSRD (Å)	Bond distance (Å)
Sample 3 P0*	0.2(1)	0.028(4)	3.07(2)
Sample 3 P1*	0.2(1)	0.027(6)	3.12(3)
Sample 3 P2	0.5(1)	0.028(4)	3.06(2)
Sample 3 P3	0.9(1)	0.016(4)	2.98(2)
Sample 3 P4	1.1(1)	0.024(3)	3.05(1)
Sample 3 P5	1.8(1)	0.021(5)	3.04(6)
Sample 2 P0*	0.8(1)	0.009(1)	2.937(7)
Sample 2 P1*	1.0(3)	0.010(1)	2.95(6)
Sample 2 P2*	1.3(1)	0.009(1)	2.938(7)
Sample 2 P3*	2.1(1)	0.009(1)	2.934(6)
Sample 2 P4*	3.0(1)	0.008(2)	2.93(1)
Sample 2 P5*	3.8(1)	0.006(1)	2.927(7)
Sample 2 P6*	4.5(1)	0.006(2)	2.92(1)
Sample 1 P0*	4.6(1)	0.014(8)	2.99(4)
Sample 1 P1*	5.1(2)	0.012(6)	2.97(3)
Sample 1 P2*	6.4(2)	0.010(7)	2.98(3)
Sample 1 P3*	8.0(1)	0.007(7)	2.95(3)
Sample 1 P6*	9.9(3)	0.006(9)	2.95(4)
Sample 1 P7*	10.9(1)	0.005(5)	2.94(2)
Sample 1 P9*	13.3(3)	0.004(3)	2.91(2)
Sample 1 P12*	16.0(3)	0.002(4)	2.89(2)
Sample 1 P16*	20.8(4)	0.002(2)	2.87(1)
Sample 1 P20*	24.3(1)	0.001(8)	2.85(6)

C.9 XANES Analysis and Discussion

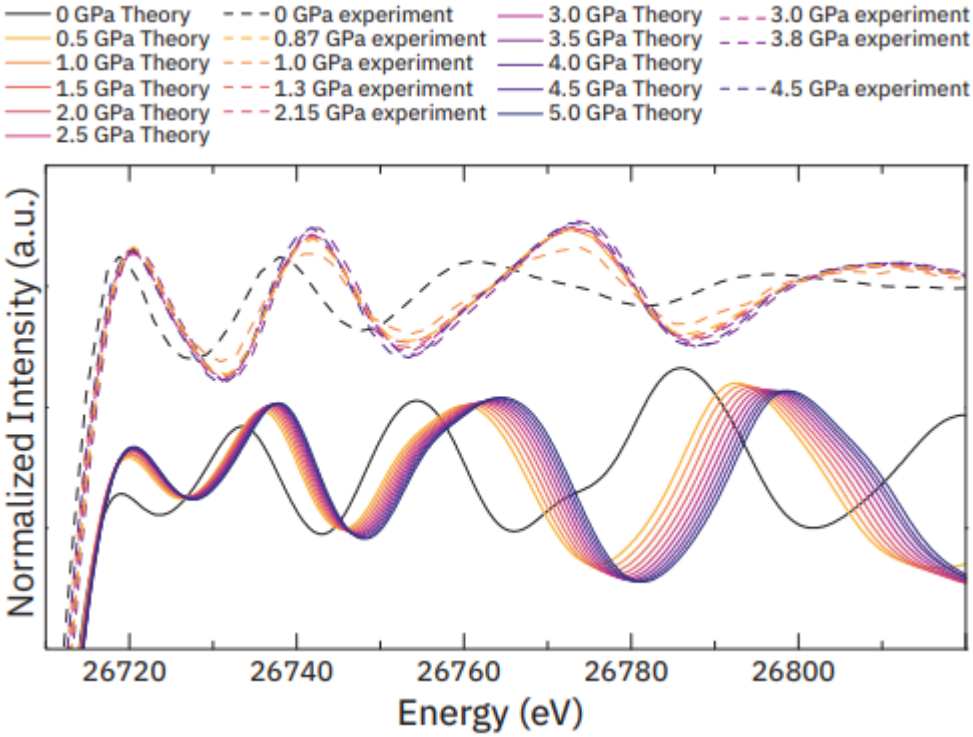

Figure C.13. Calculated and experimental XANES spectra collected for Cd between 0 and 5 GPa. Dashed lines represent experimental data, while solid lines show theoretical results. The OCEAN-simulated spectra are background-subtracted and normalized using the same procedure as the experimental data but are not additionally scaled.

OCEAN-simulated spectra shown in **Fig. C.14** are presented without background subtraction or additional scaling. The OCEAN code calculates only core-level transitions and does not explicitly include a decaying background. As a result, the computational spectra naturally exhibit a gradual decrease in intensity with increasing energy due to the intrinsic energy dependence of the transition cross section. This downward trend is physically meaningful and should not be removed, as it reflects real features of the core excitation process.

In contrast, experimental XANES spectra include contributions from both core and valence excitations. The valence-related background leads to an additional energy-dependent decay

that is typically removed during normalization to isolate structural information, particularly for EXAFS analysis. This subtraction is necessary to properly extract oscillatory features at higher energies, where structural sensitivity is encoded.

While background removal is appropriate for experimental data in the context of EXAFS, applying the same procedure to OCEAN calculations would be inappropriate, as it would remove a physically meaningful contribution already accounted for by the theory. For ease of visual comparison in **Chapter 3**, the OCEAN spectra are shown with an applied scaling and adjusted baseline; however, the unmodified form is retained in **Fig. C.14** to reflect the raw theoretical output.

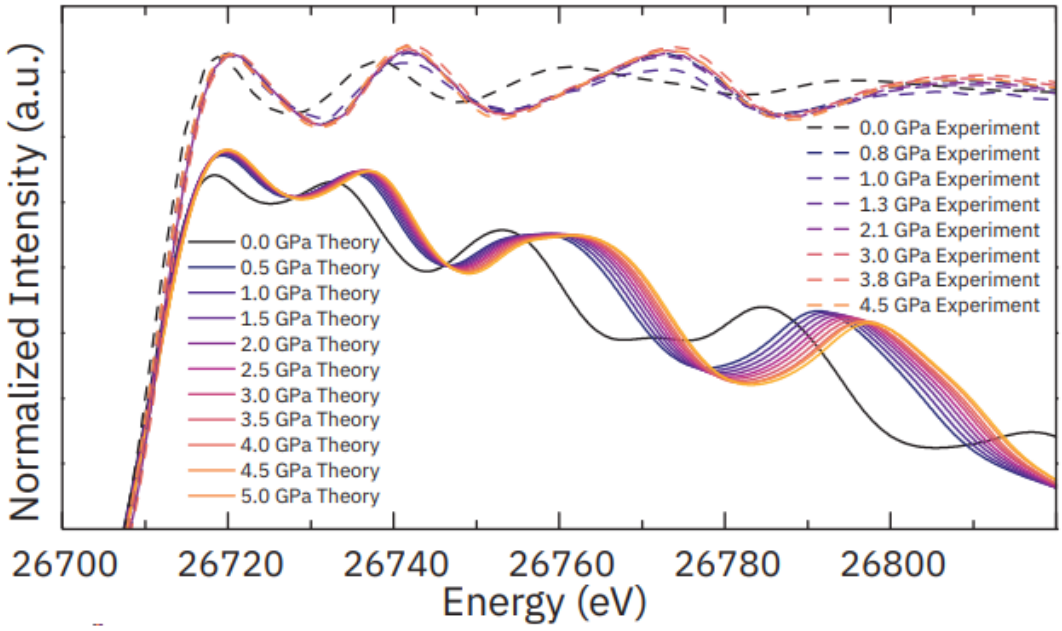

Figure C.14. Calculated (without background subtraction) and experimental XANES spectra collected for Cd between 0 and 5 GPa. Dashed lines represent experimental data, while solid lines show theoretical results.

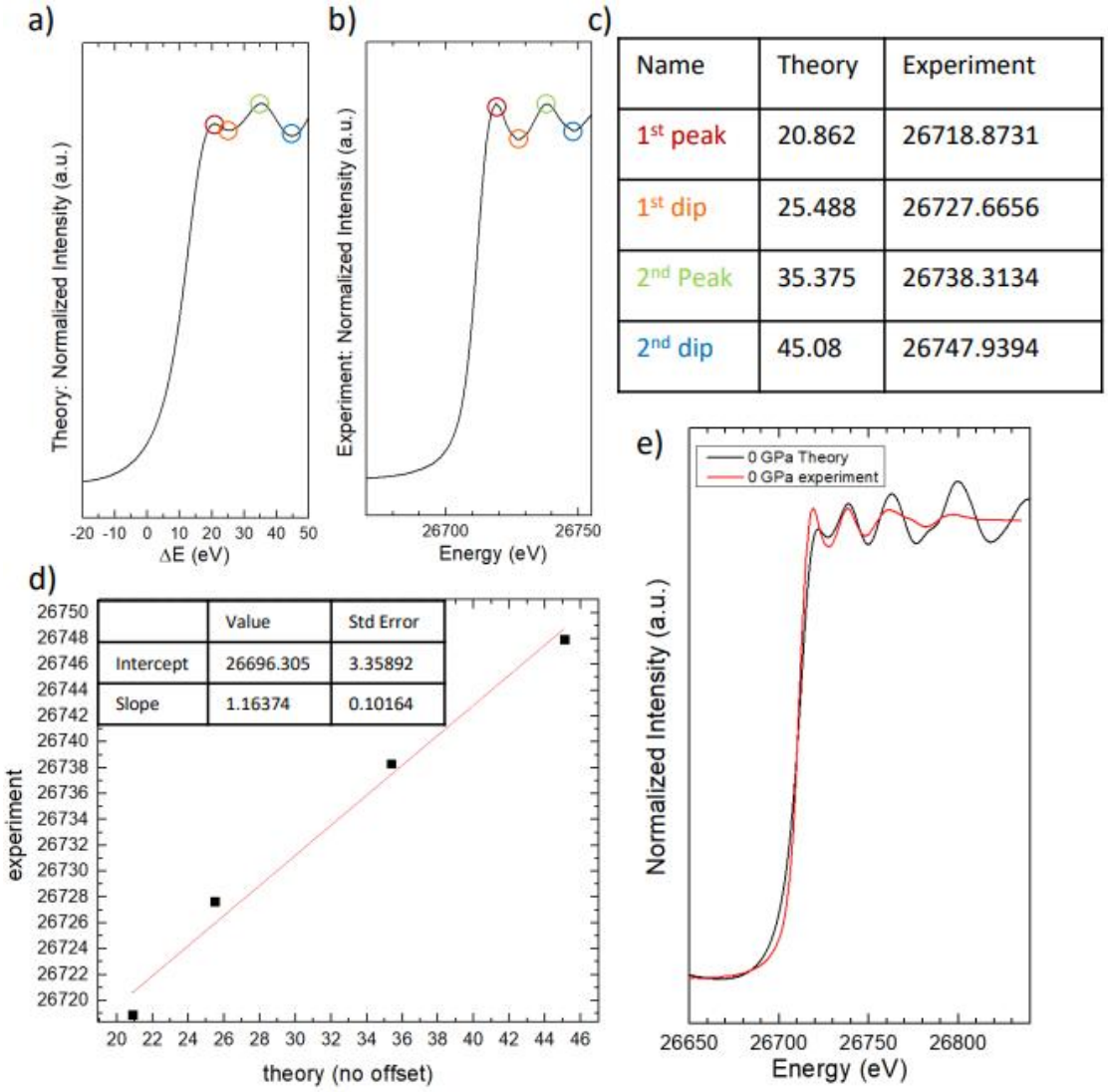

Figure C.15. Scaling procedure applied to theoretical XAS spectra. (a) OCEAN-calculated spectra of Cd at 0 GPa. **(b)** Experimental spectra of Cd at 0 GPa. **(c)** Tabulated values used to determine the scaling factor. **(d)** Linear fit of the data in (c) where the slope is used as the scaling factor applied to the theoretical spectra. **(e)** Comparison of scaled theoretical and experimental XAS spectra. The energy offset was adjusted to align the white-line positions, with a final offset value of 26697.5 eV.

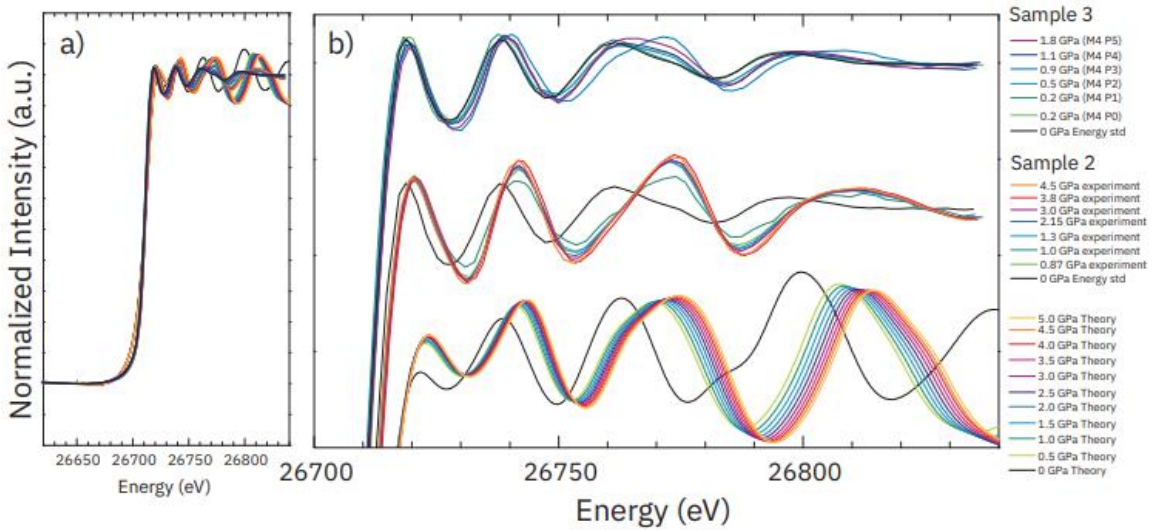

Figure C.16. Experimental XAS spectra for Samples 2 and 3 compared with theoretical results, shown with normalized intensity. In both panels, the black trace corresponds to the energy standard spectrum included for ease of comparison across datasets. **(a)** Full energy range showing the absorption edge region. **(b)** Spectra offset by sample for improved visual separation. While Sample 2 and the theoretical spectra exhibit more readily distinguishable differences between 0 GPa and higher-pressure conditions, the corresponding shifts in Sample 3 are less apparent. See **Fig. C.17** for an increased individual offset.

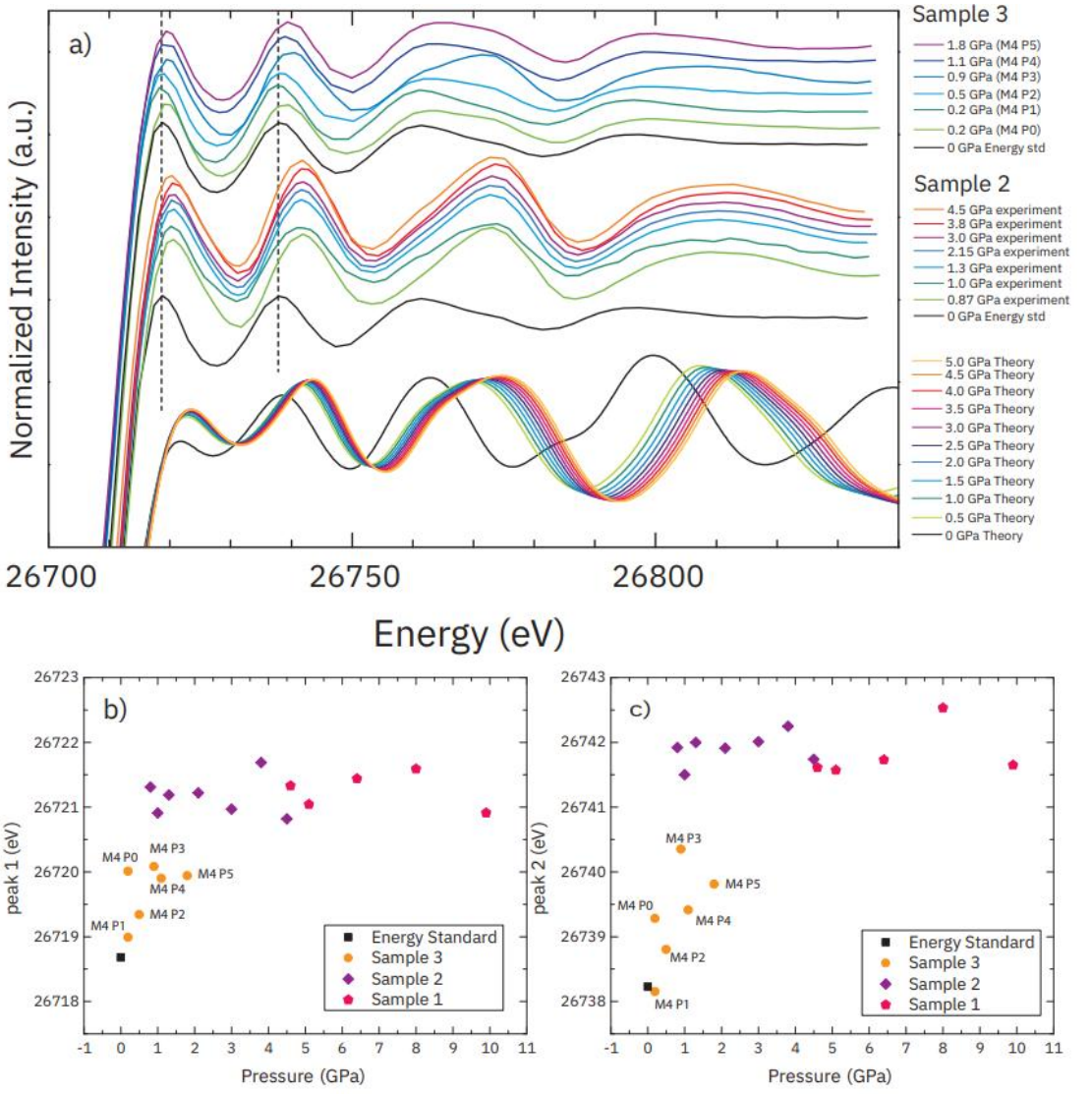

Figure C.17. XAS peak evolution with pressure for Samples 2 and 3 including comparison with theory. (a) Experimental XAS spectra for Samples 2 and 3 plotted alongside theoretical results. The black trace corresponds to the energy standard sample used for reference. Spectra are vertically offset to enhance visibility of pressure-dependent changes. For Sample 2, the pressure series begins at 0.87 GPa. This sample was gas loaded at ~0.3 GPa, compressed to just above 0.5 GPa, and then measured at the beamline, where the initial recorded condition corresponds to Sample 2 P0 (~0.8 GPa). Thus, Sample 2 underwent monotonic compression only. Sample 3 was gas loaded at ~0.3 GPa, compressed to 1.8 GPa, and subsequently decompressed close to its initial loading pressure

prior to measurement. As a result, Sample 3 experienced pressure cycling prior to arriving at the experiment. Measurements of Sample 3 (M4) at P0 (0.2 GPa) were performed after completing the Sample 2 dataset and returning to Sample 3 later. The lower apparent energy position of M4 P1 relative to M4 P0, despite similar nominal pressure, is attributed to relaxation effects over the elapsed time between measurements. As pressure increases, Sample 3 (M4) exhibits a systematic increase in energy shift for both the first and second spectral features. This trend is further illustrated in panels **(b)** and **(c)**, which track the pressure-dependent evolution of the first and second XAS peak positions, respectively.

C.10 Alternate-View Diagram of the Fermi Surface

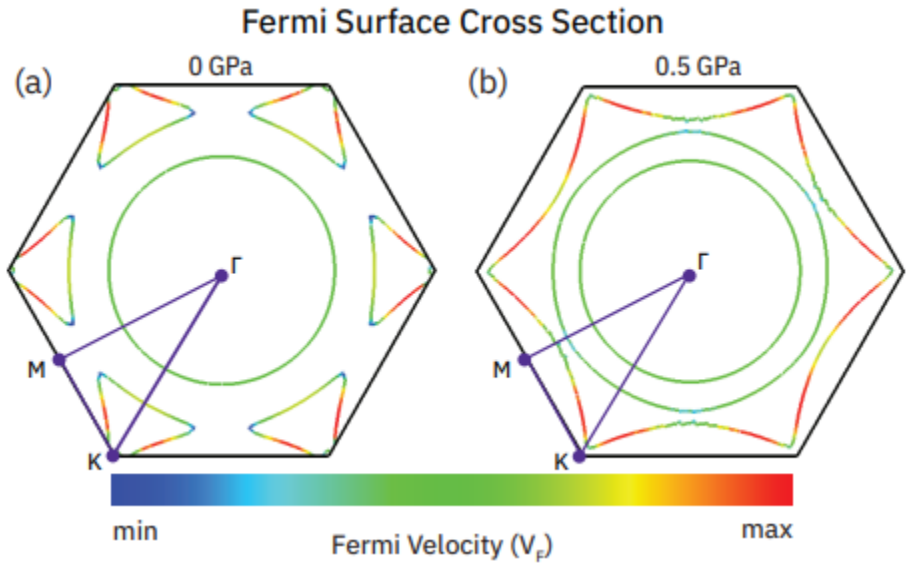

Figure C.18. Cross-sectional view of the Cd Fermi surface at (a) 0 GPa and (b) 0.5 GPa. High-symmetry points Γ, M, and K are indicated. The comparison highlights the pressure-induced changes in the Fermi surface topology between the two conditions.

C.11 Partial Density of States

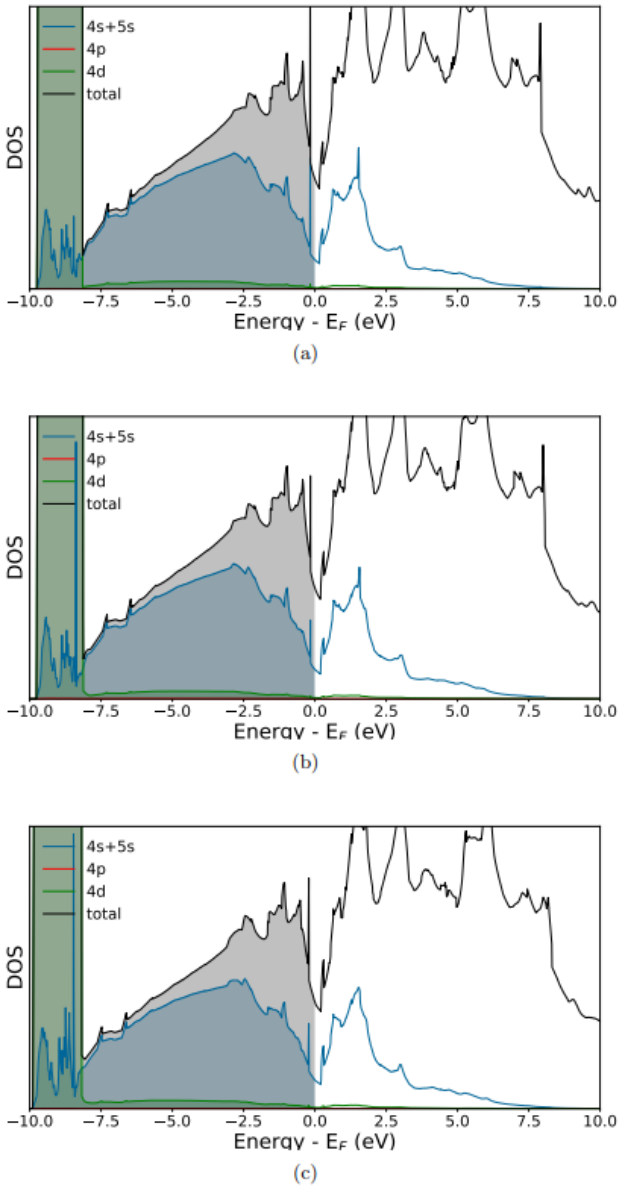

Figure C.19. Total and projected density of states for Cd resolved onto the atomic wavefunctions included in the pseudopotential (4*s*, 4*p*, 5*s*, 4*d*), at three pressures: (a) 0 GPa, (b) 0.5 GPa, and (c) 2 GPa. The projections show reduced density near the Fermi level, likely due to contributions from Cd 5*p* states that are not included in the pseudopotential.

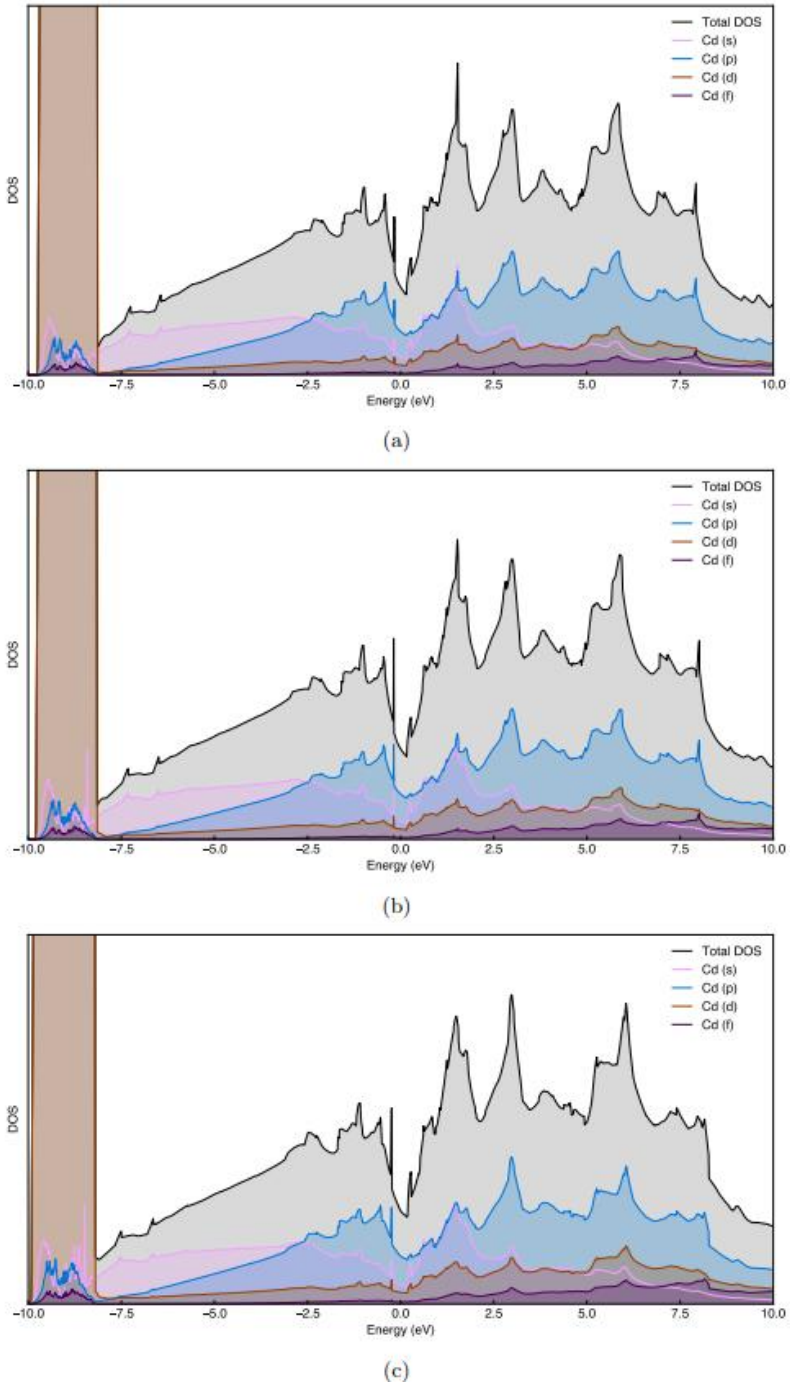

Figure C.20. Total and projected density of states calculated using VASP 5.4.4 at three pressures: (a) 0 GPa, (b) 0.5 GPa, and (c) 2 GPa. The calculations employ the same crystal structures, k-point meshes, and computational settings as those used in **Fig. C.19**; however, here the projections are performed in VASP 5.4.4 using a spherical-harmonics–

based scheme rather than the atomic-orbital projections defined in the pseudopotential. This projection method reveals that Cd *p* states contribute significantly to the previously unaccounted density near the Fermi level observed in **Fig. C.19**. In addition, the pressure-dependent changes in the conduction states associated with the electronic topological transition (ETT) are primarily derived from Cd *p* character. The Cd_sv_GW pseudopotential was used throughout. The Wigner–Seitz radius was set to 1.730 Å, corresponding to coverage of 99.4% of the volume of the 2.0 GPa structure. All density-of-states plots were generated using the sumo package.[2]

C.12 Additional Views of the Band Projection

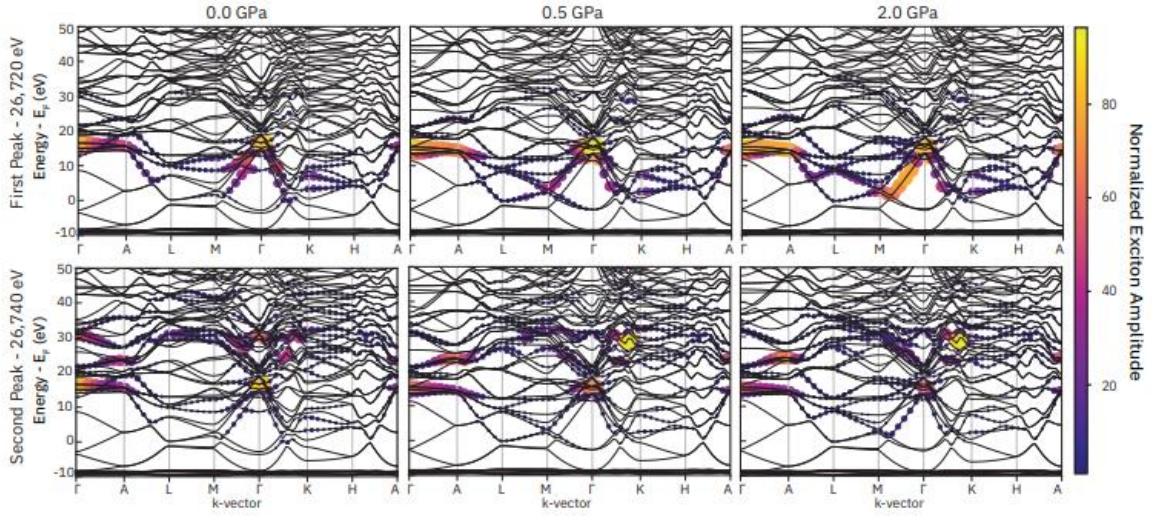

Figure C.21. First and second peak projections onto the Cd band structure at 0, 0.5, 2.0 GPa in the same view as in Chapter 3 but shown in landscape.

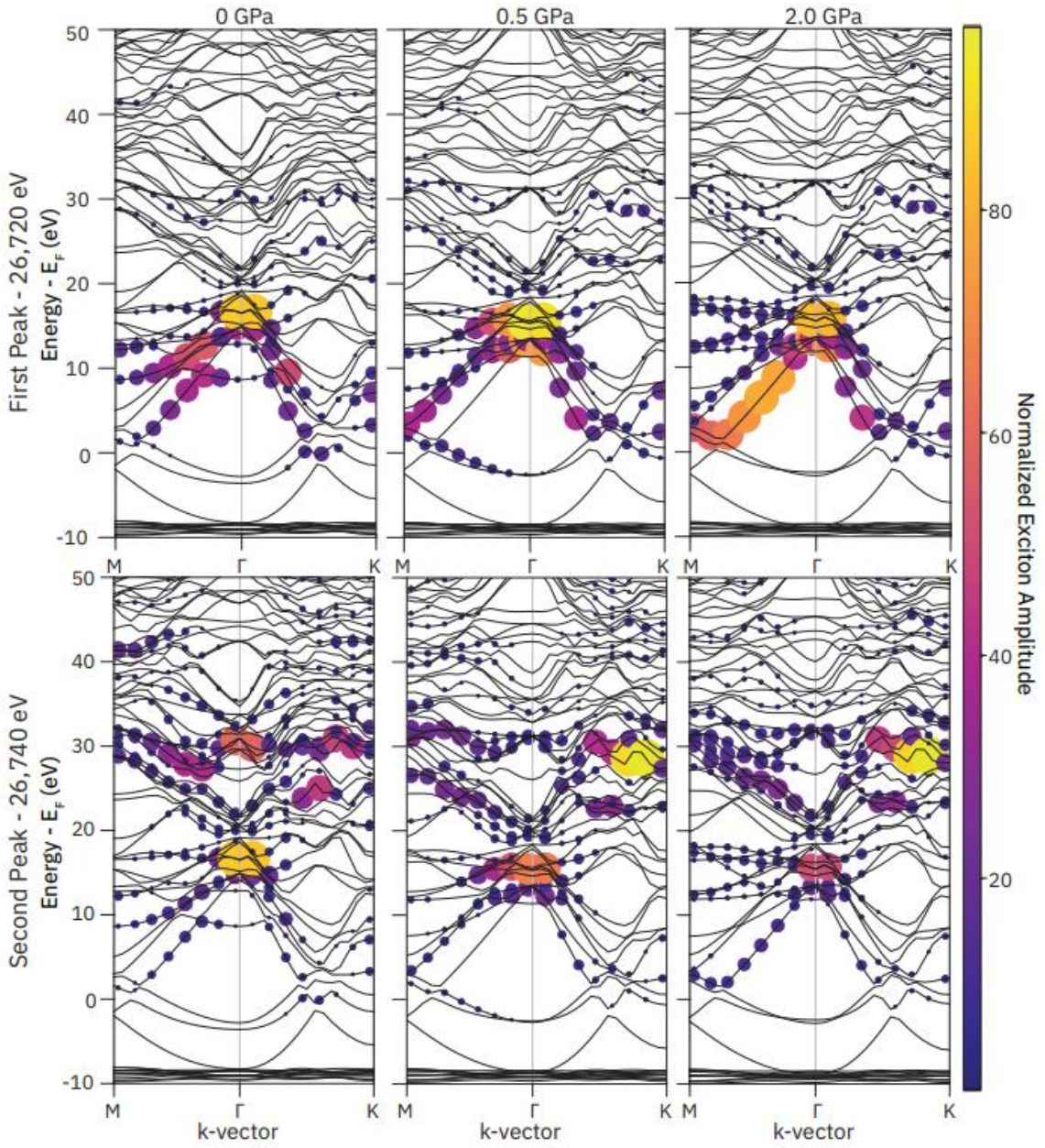

Figure C.22. First and second peak projection onto the Cd band structure at 0, 0.5, and 2.0 GPa between M, Γ, and K points.

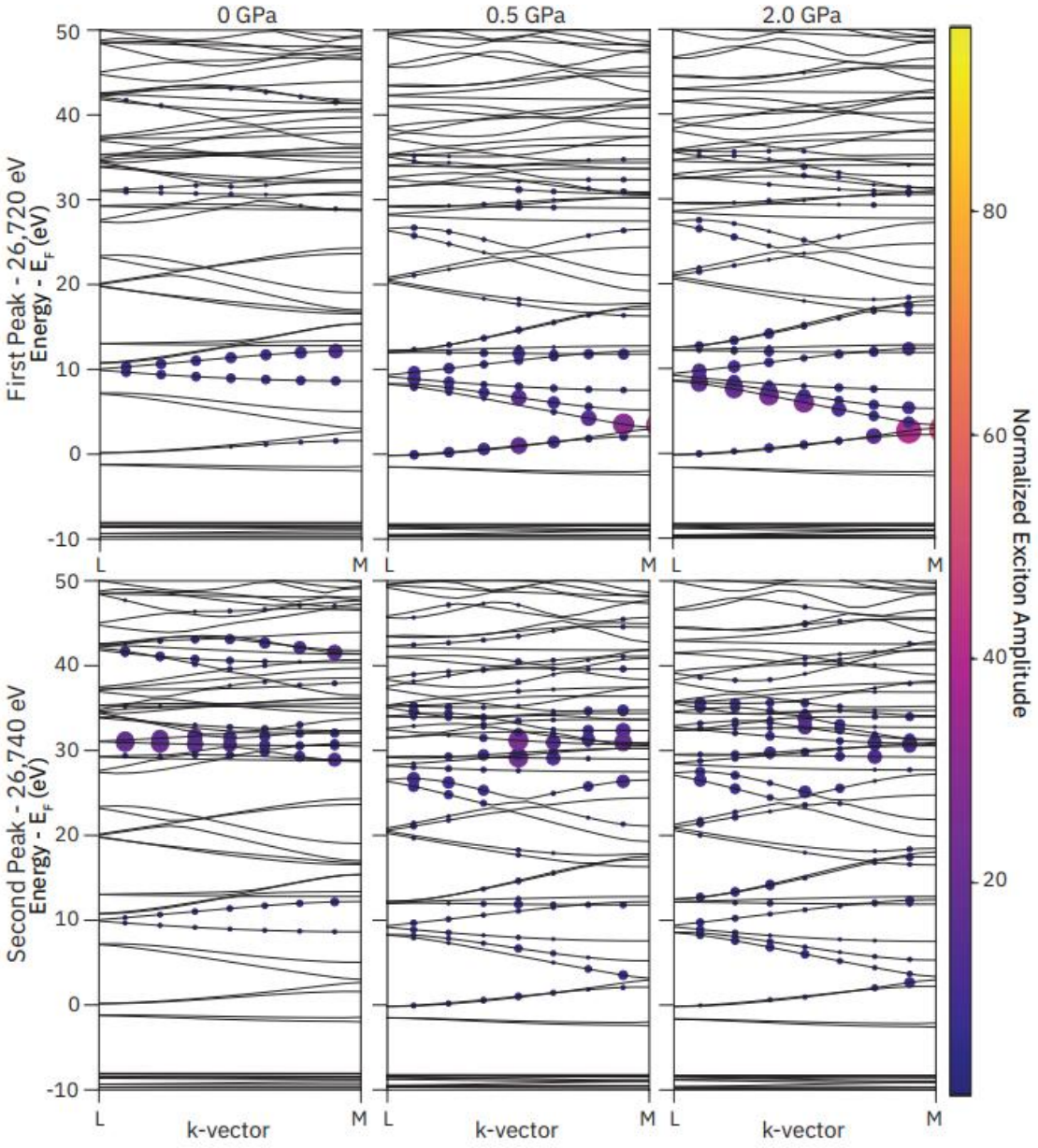

Figure C.23. First and second peak projection onto the Cd band structure at 0, 0.5, and 2.0 GPa between L and M points.

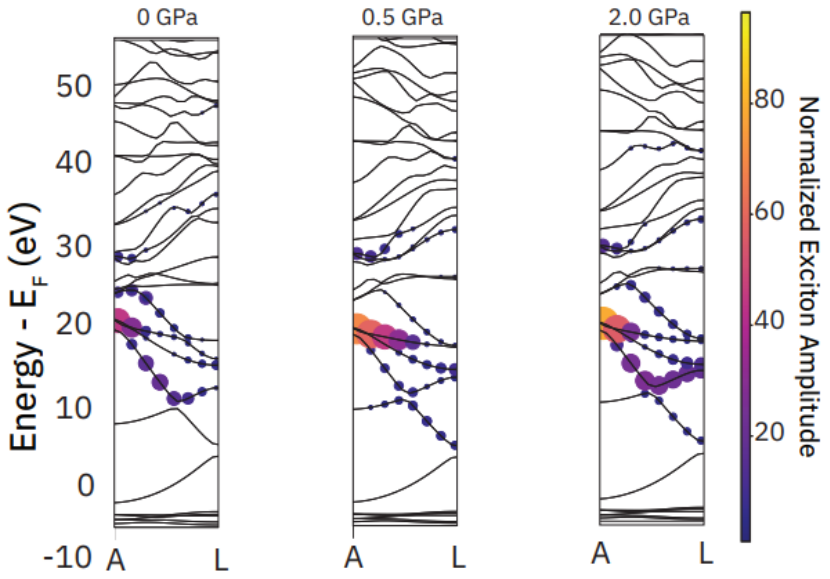

Figure C.24. First peak projection onto the Cd band structure at 0, 0.5, and 2.0 GPa between A and L points.

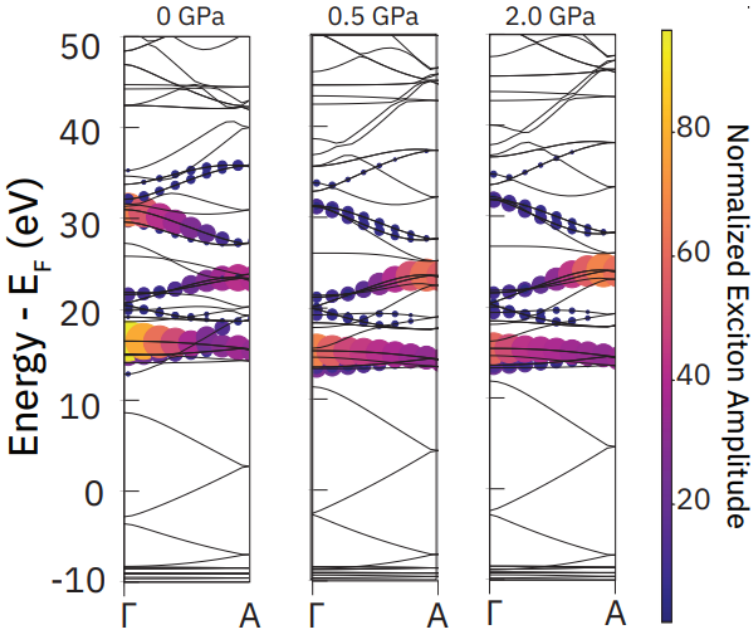

Figure C.25. Second peak projection onto the Cd band structure at 0, 0.5, and 2.0 GPa between Γ and A points.

C.13 Experimental and Computational Raman Results

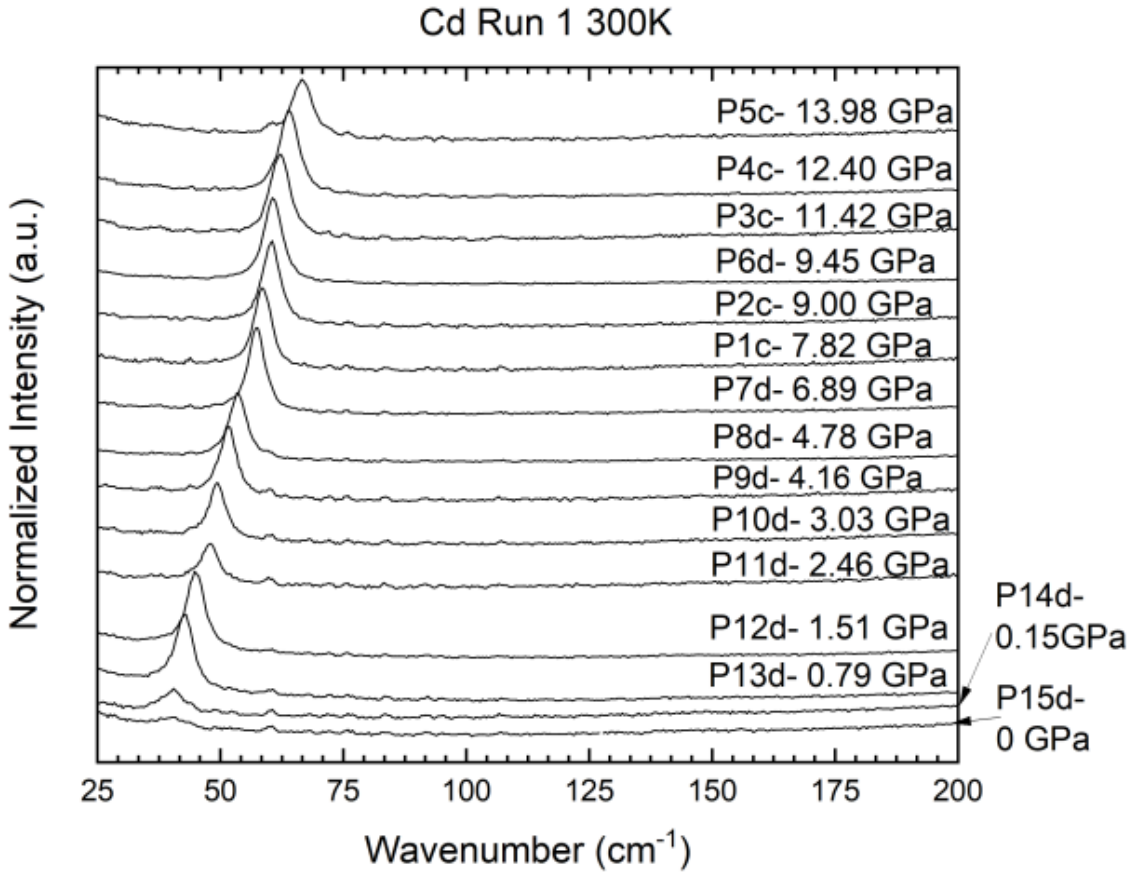

Figure C.26. Raman stack plot of Cd at ambient temperature from Run 1. Intensities are normalized to the range [0,1]. The sample was not externally heated; however, it was pressure cycled from high initial pressure (P1) down to low and ambient pressures. Labels "c" and "d" denote compression and decompression points, respectively, while the accompanying number indicates the chronological order in which the points were taken. Run 1 P3c, P4c, and P5c data are included for numerical consistency, although these values are not tabulated in **Table C.III**.

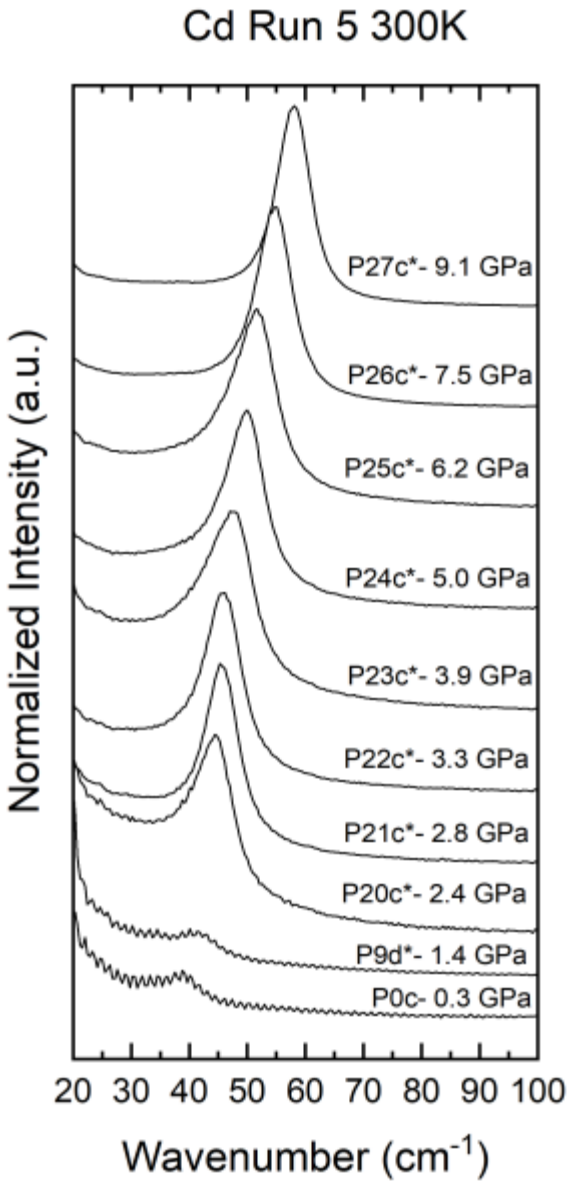

Figure C.27. Raman stack plot of Cd at ambient temperature from Run 5. Intensities are normalized to the range [0,1]. Points with stars (*) indicate that the sample was heated to above melting temperature. Heating happened between P0 and P9 as well as between P9 and P20. As in **Fig. C.26**, "c" and "d" denote compression and decompression, respectively and the number indicates the chronological order in which data were logged.

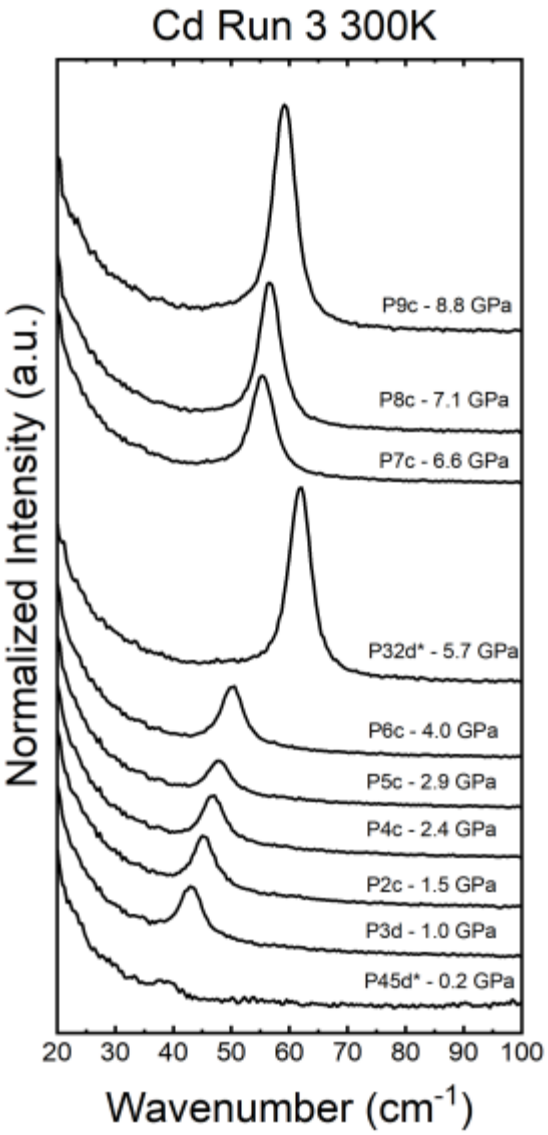

Figure C.28. Raman stack plot of Cd at ambient temperature from Run 3. Intensities are normalized to the range [0,1]. Points with stars (*) indicate that the sample was heated previously. As in **Fig. C.26**, "c" and "d" denote compression and decompression, respectively and the number indicates the chronological order in which data were logged.

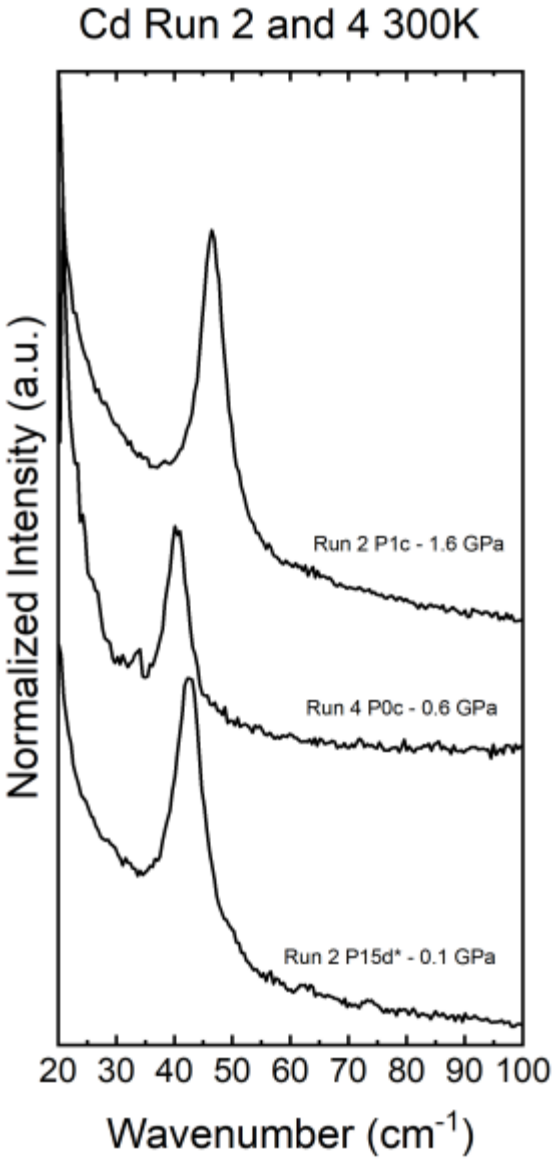

Figure C.29. Raman stack plot of Cd at ambient temperature from Runs 2 and 4. Intensities are normalized to the range [0,1]. Points with stars (*) indicate that the sample was heated previously. As in Fig. C.26, "c" and "d" denote compression and decompression, respectively and the number indicates the chronological order in which data were logged. Runs 2 and 4 contain the fewest measurements at 300 K; these datasets are included here for completeness and ease of viewing.

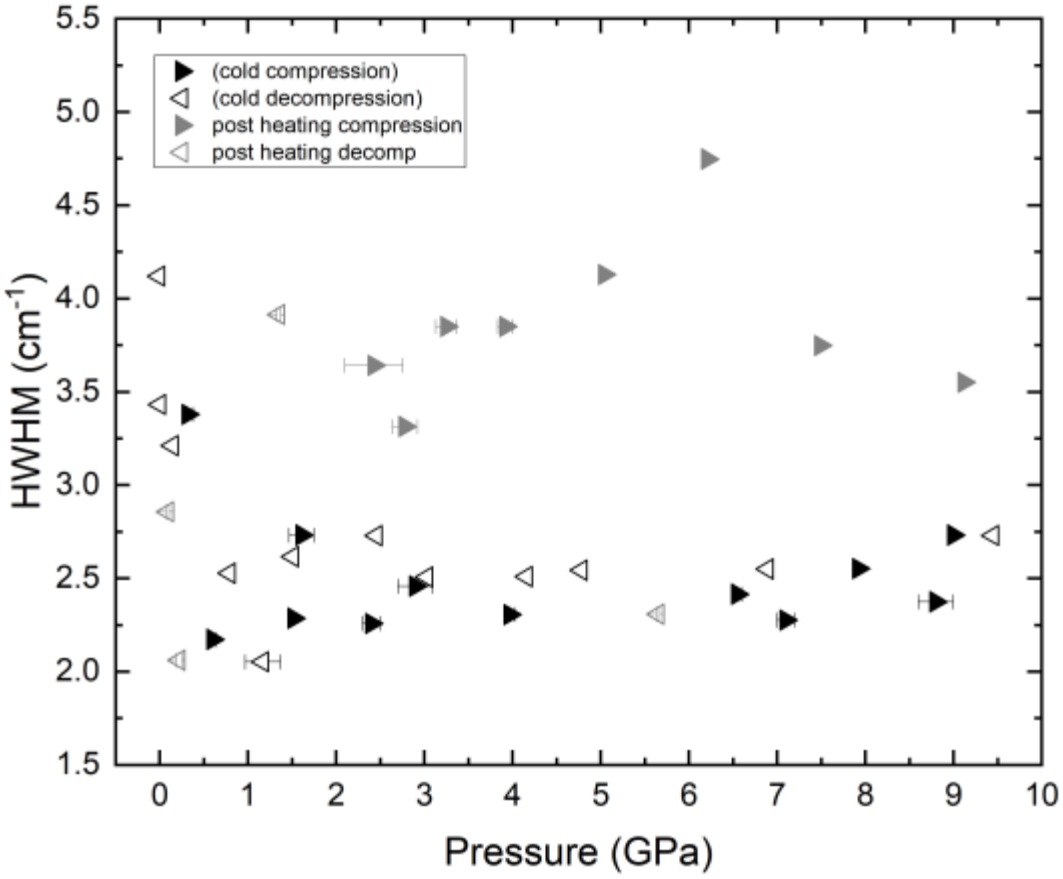

Figure C.30. Pressure dependence of the half-width at half-maximum (HWHM) of the Cd T_{2g} Raman mode, obtained from peak fits performed in Fityk. The data include both cold compression and decompression (no prior heating) as well as post-heating compression and decompression where the sample was heated along an isotherm before returning to ambient temperatures.

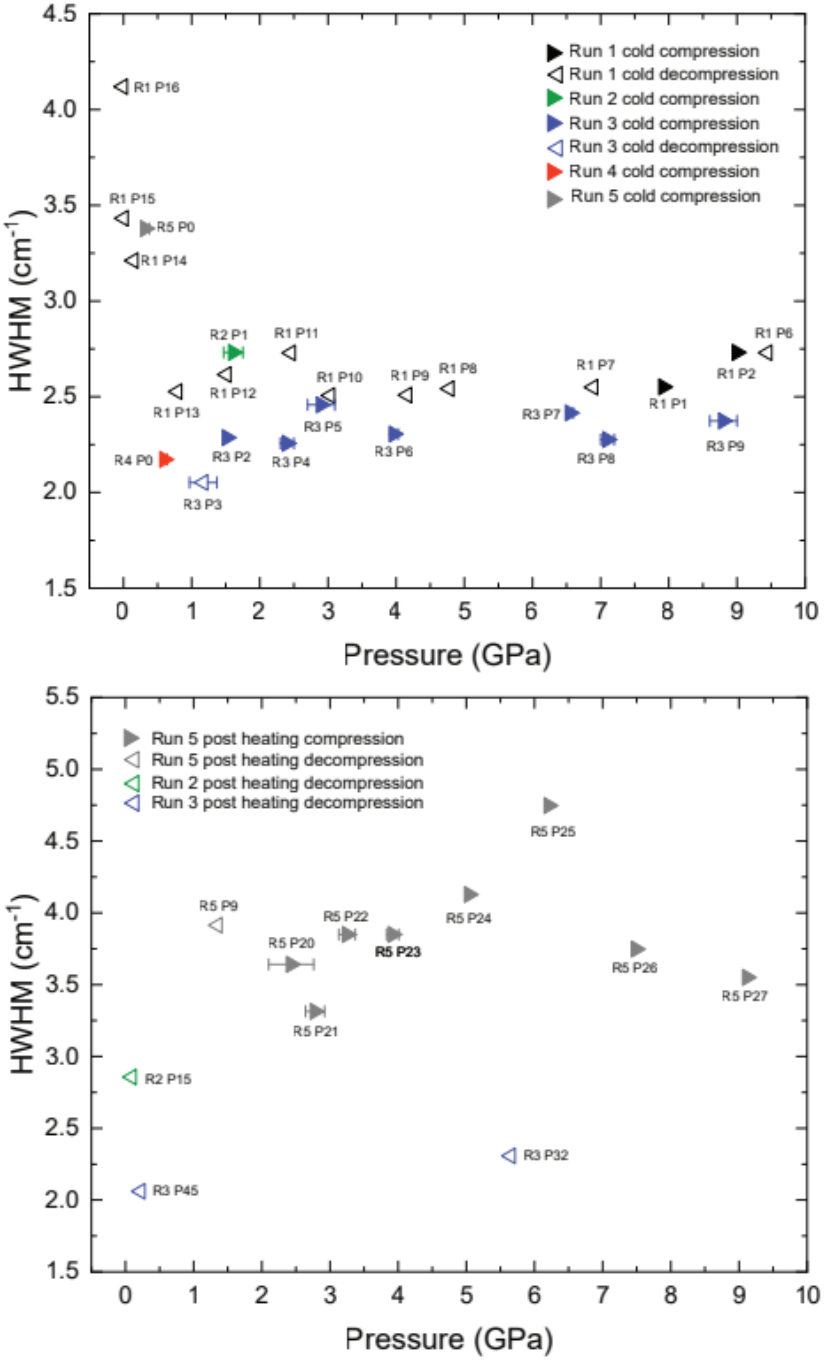

Figure C.31. Same dataset as in Fig. C.30 with color and labels added to specify which run (and thus loading) and experimental points the data came from.

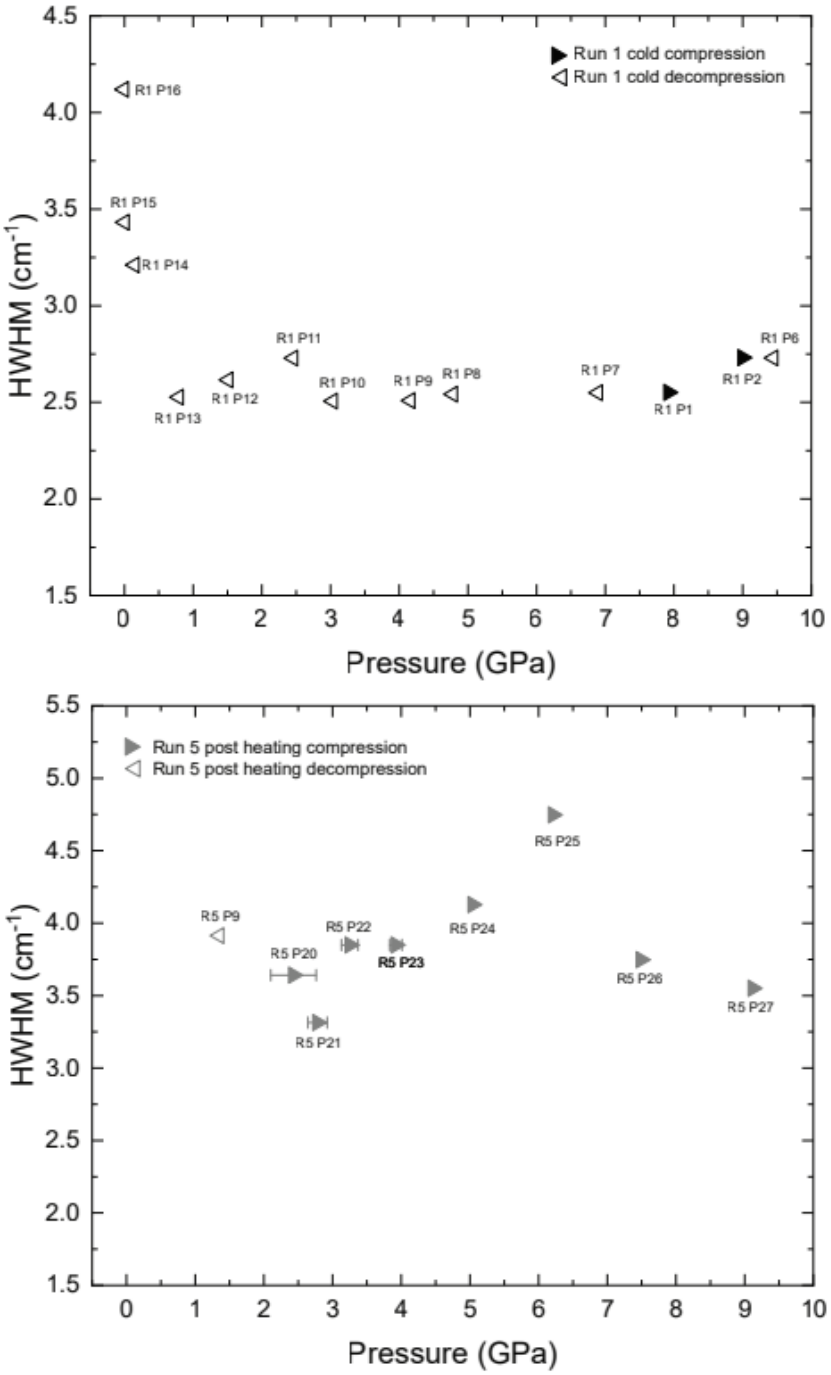

Figure C.32. Subset of the dataset shown in Fig. C.31, including only Runs 1 and 5 since these were majority contributors to the plot.

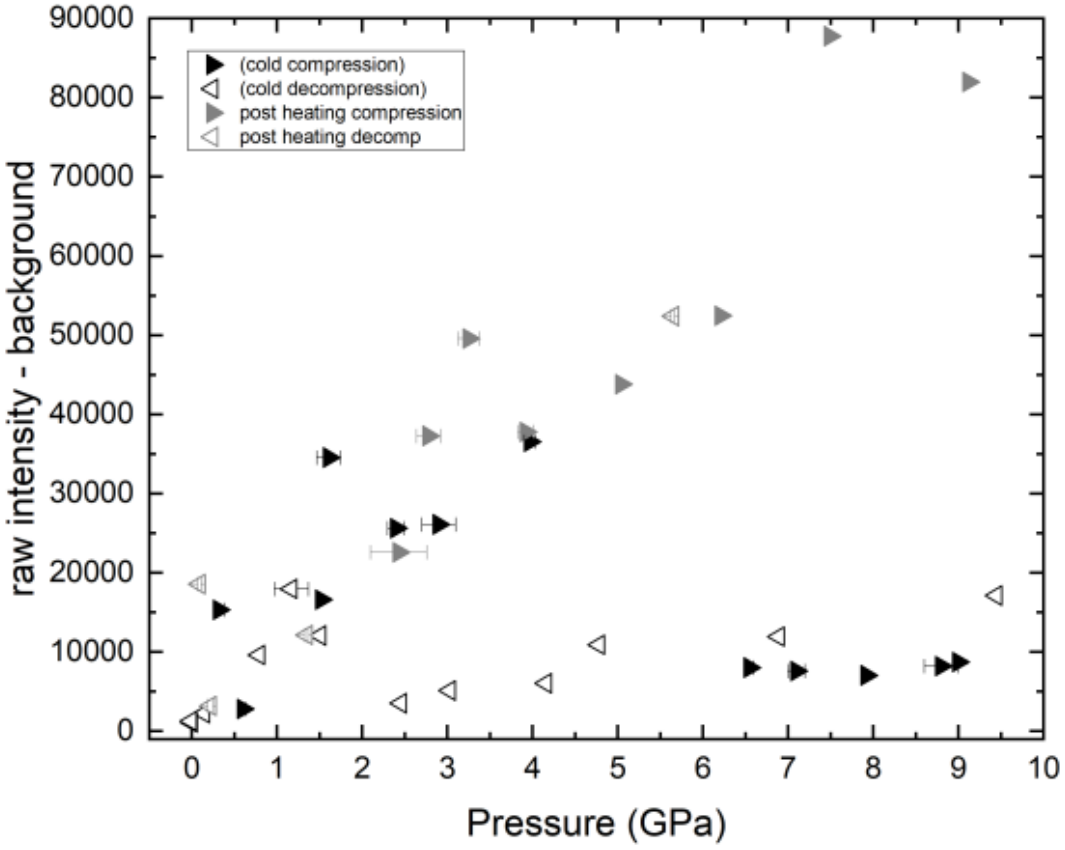

Figure C.33. Pressure dependence of the intensity of Cd's T_{2g} Raman mode, obtained from peak fitting performed in Fityk and plotted as a function of pressure.

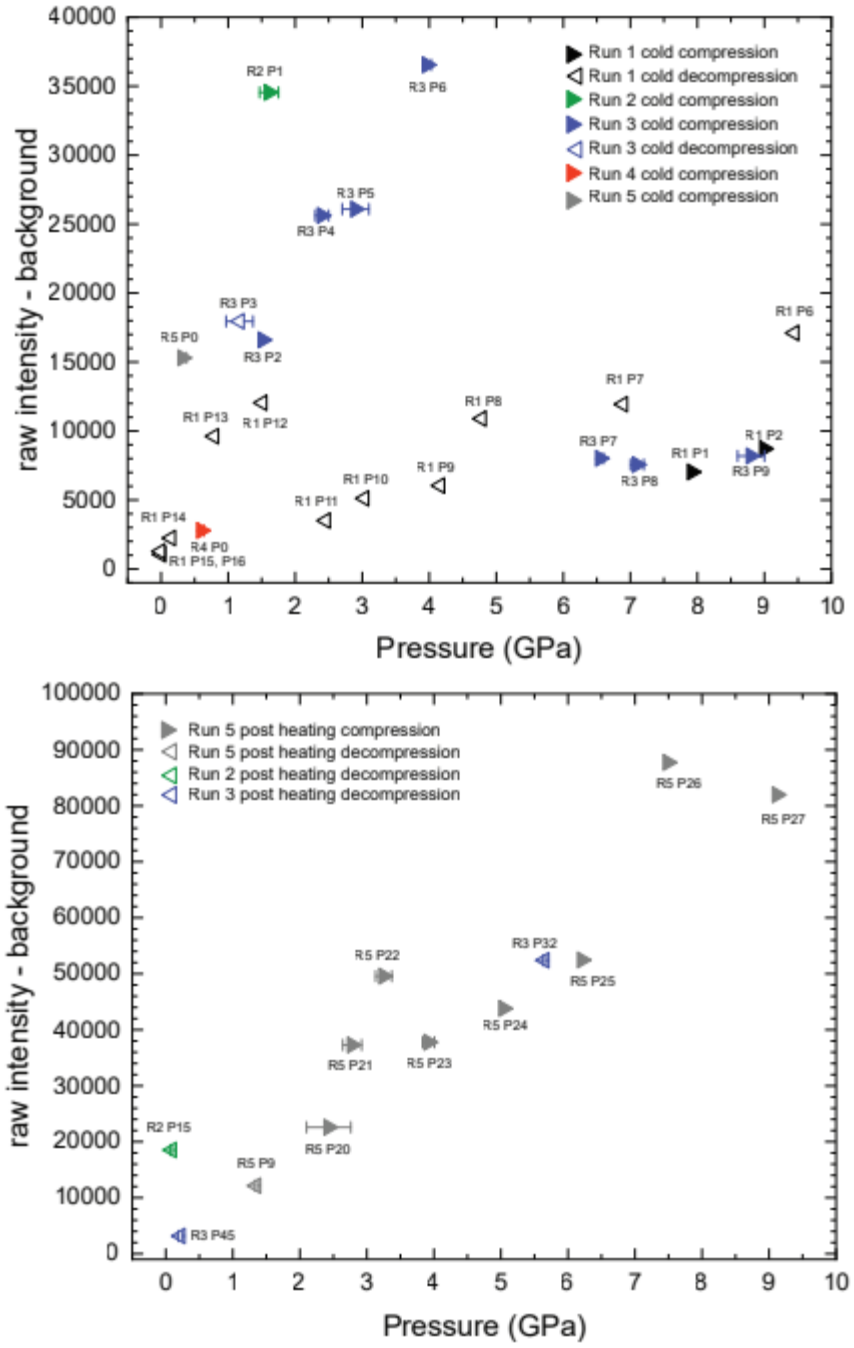

Figure C.34. Same dataset as in Fig. C.33 with color and labels added to specify which run (and thus loading) and experimental points the data came from.

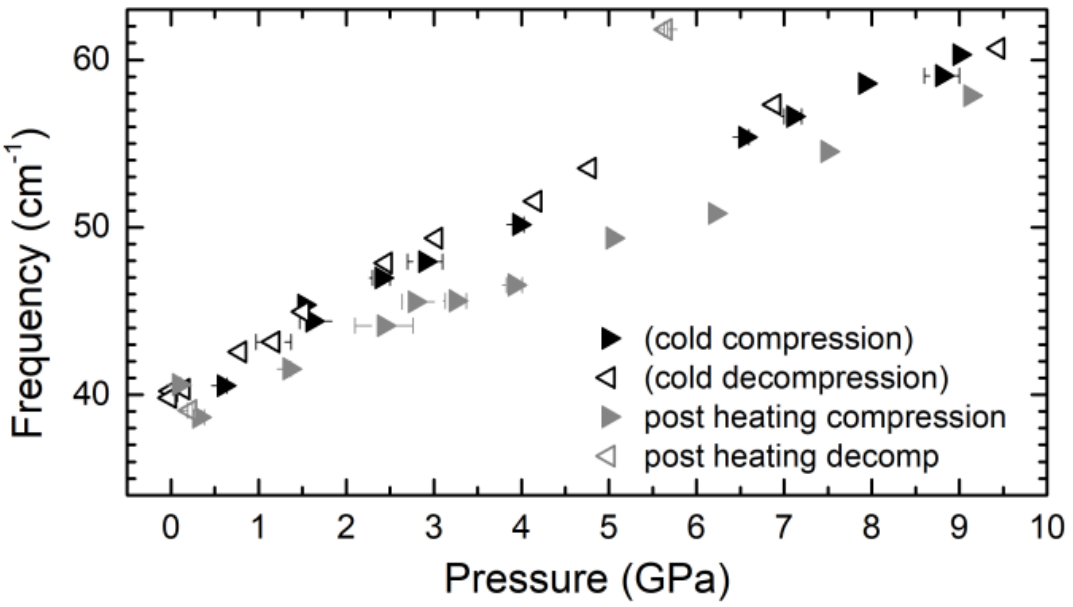

Figure C.35. Pressure dependence of the Cd E_{2g} Raman mode frequency at room temperature. Data points are compiled from multiple samples and include both cold compression/decompression cycles and compression/decompression measurements following resistive heating. The pressure transmitting medium (PTM) for all measurements is lithium fluoride (LiF), which is much less hydrostatic than a He PTM.

Table C.III. Experimental Raman frequencies as a function of pressure, with corresponding temperature information. The HWHM, intensity, and collection time (where available) are also reported.

Name	Pressure (GPa)	Temperature (K)	Frequency (cm^{-1})	HWHM (cm^{-1})	I (raw) – I(bknd) (counts)	Time (s) Number Acc (#)
R1 P16 d	0.0(1)	298(2)	40.15	4.12	1272.243	60s5x
R1 P15 d	0.0(1)	298(2)	40.42	3.43	1058.97	60s5x
R2 P15 d*	0.1(1)	298(2)	40.6	2.86	18537.28	10s6x
R1 P14 d	0.2(1)	298(2)	40.3	3.21	2240.452	60s5x
R3 P45 d*	0.2(1)	297(2)	39.06	2.06	3172.883	20s3x
R5 P0 c	0.3(1)	298(2)	38.66	3.38	15307.33	
R4 P0 c	0.6(4)	297(2)	40.53	2.17	2786.773	
R1 P13 d	0.7(1)	298(2)	42.56	2.53	9614.152	60s5x
R3 P3 d	1.0(3)	298(2)	43.14	2.05	17952.37	10s6x

R5 P9 d*	1.4(1)	294(2)	41.54	3.91	12136.89	10s6x
R1 P12 d	1.5(1)	298(2)	44.94	2.62	12047.18	60s5x
R3 P2 c	1.5(1)	298(2)	45.35	2.29	16599.89	10s6x
R2 P1 c	1.6(1)	298(2)	44.39	2.48	34549.73	10s6x
R3 P4 c	2.4(1)	298(2)	46.97	2.26	25615.95	10s6x
R5 P20 c*	2.4(3)	298(2)	44.12	3.64	22576.35	
R1 P11 d	2.5(1)	298(2)	47.78	2.73	3497.808	60s5x
R5 P21 c*	2.8(1)	298(2)	45.54	3.31	37271.34	
R3 P5 c	2.9(2)	298(2)	47.94	2.46	26091.27	10s6x
R1 P10 d	3.0(1)	298(2)	49.32	2.51	5115.516	60s5x
R5 P22 c*	3.3(1)	298(2)	45.6	3.85	49558.55	
R5 P23 c*	3.9(1)	298(2)	46.56	5.01	37753.93	
R3 P6 c	4.0(1)	298(2)	50.16	2.31	36542.41	10s6x
R1 P9 d	4.2(1)	298(2)	51.51	2.51	6038.844	60s5x
R1 P8 d	4.8(1)	298(2)	53.53	2.54	10897.11	60s5x
R5 P24 c*	5.0(1)	298(2)	49.36	4.13	43794.25	
R3 P32 d*	5.7(1)	298(2)	61.81	2.31	52404.18	20s3x
R5 P25 c*	6.2(1)	298(2)	50.82	4.75	52444.96	
R3 P7 c	6.6(1)	298(2)	55.37	2.42	8015.149	10s6x
R1 P7 d	6.9(1)	298(2)	57.33	2.55	11938.62	60s5x
R3 P8 c	7.1(1)	298(2)	56.62	2.28	7570.172	10s6x
R5 P26 c*	7.5(1)	298(2)	54.53	3.75	87748.07	
R1 P1 c	7.9(1)	298(2)	58.54	2.55	7035.625	60s5x
R3 P9 c	8.8(2)	298(2)	59.06	2.37	8194.168	10s6x
R1 P2 c	9.0(1)	298(2)	60.3	2.73	8717.558	60s5x
R5 P27 c*	9.1(1)	298(2)	57.85	3.55	81960.82	
R1 P6 d	9.5(1)	298(2)	60.67	2.73	17106.15	60s5x

The naming convention is as follows: “R” indicates which run (in other words what loading) the data came from, “P” is the point name and indicates when the pressure was changed, “c” or “d” indicates compression or decompression, and the * indicates points that were heated previously. These experiments were done in a LiF PTM with Sm:SrB_4O_7 as the pressure marker. Loading methods and heating setup have been previously described and can be found in Ref. 3.

Table C.IV. Calculated zone-center (q = Γ) phonon mode frequency ($\omega_{q\nu}$), electron–phonon coupling constant ($\lambda_{q\nu}$), and phonon linewidth ($\gamma_{q\nu}$) as functions of pressure for the experimentally observed E_{2g} mode of Cd. Only one of the two degenerate modes (ν = 4) is shown. No anomalies or discontinuities are predicted across the electronic topological transition at 0.5 GPa.

Pressure (GPa)	$\omega_{q\nu}$ (cm^{-1})	$\lambda_{q\nu}$	$\gamma_{q\nu}$ (GHz)
0	21.37904	0.2295	0.43
0.1	21.82046	0.2255	0.43
0.2	22.24821	0.2223	0.44
0.3	22.67105	0.2182	0.44
0.4	23.08946	0.215	0.44
0.5	23.49362	0.2118	0.45
0.6	23.9022	0.2087	0.45
0.7	24.3102	0.2057	0.46
0.8	24.69096	0.2034	0.46
0.9	25.07644	0.2005	0.46
1	25.47357	0.1976	0.47

The structures were optimized following the same procedure described in **Chapter 3**. The phonon linewidths and electron-phonon couplings were calculated using the double-δ smearing technique implemented in Quantum Espresso with a smearing parameter of 0.040 Ry.[4,5] As this double-δ smearing implementation requires that the q-grid be a subset of the k-grid, the scf was calculated on a 12×12×6 k-grid, the dense scf was calculated on a 24×24×12 k-grid, and the phonons were calculated on a 6×6×3 q-grid. The acoustic sum rule was applied to the calculated phonon frequencies using the 'simple' setting.

C.14 References

(1) Park, C.; Popov, D.; Ikuta, D.; Lin, C.; Kenney-Benson, C.; Rod, E.; Bommannavar, A.; Shen, G. New Developments in Micro-X-ray Diffraction and X-ray Absorption Spectroscopy for High-Pressure Research at 16-BM-D at the Advanced Photon Source. *Rev. Sci. Instrum.* **2015**, *86* (7), 072205.

(2) Ganose, A. M.; Jackson, A. J.; Scanlon, D. O. sumo: Command-Line Tools for Plotting and Analysis of Periodic *Ab Initio* Calculations. *J. Open Source Softw.* **2018**, *3* (28), 717.

(3) Hinton, J. K.; Childs, C.; Smith, D.; Ellison, P. B.; Lawler, K. V.; Salamat, A. Response of the Mode Gruneisen Parameters with Anisotropic Compression: A Pressure and Temperature Dependent Raman Study of *β*-Sn. *Phys. Rev. B* **2020**, *102* (18), 184112.

(4) Wierzbowska, M.; de Gironcoli, S.; Giannozzi, P. Origins of Low- and High-Pressure Discontinuities of *Tc* in Niobium. arXiv:cond-mat/0504077v2.

(5) Shipley, A. M.; Hutcheon, M. J.; Johnson, M. S.; Needs, R. J.; Pickard, C. J. Stability and Superconductivity of Lanthanum and Yttrium Decahydrides. *Phys. Rev. B* **2020**, *101* (22), 224511.

Appendix D

SUPPLEMENTARY INFORMATION FOR SELF-DIFFRACTION OF FEMTOSECOND EXTREME ULTRAVIOLET PULSES IN COBALT

D.1 Electronic Structure Calculations for hcp Cobalt

The electronic density of states (DOS) of cobalt (Co) is calculated within density functional theory (DFT) using Quantum ESPRESSO version 7.0.[1,2] Co adopts a hcp structure at ambient conditions with lattice constants of a = 4.736 Bohr and c = 7.693 Bohr.[3] A kinetic energy cutoff of 100 Ry is applied for the plane-wave expansion of the Kohn-Sham wavefunctions. The calculations use a norm-conserving Troullier-Martins pseudopotential[4] with the Perdew-Burke-Ernzerhof generalized gradient approximation exchange-correlation functional.[5] The integration of the Brillouin zone is performed using a 12 × 12 × 6 Monkhorst-Pack (MP) k-point grid,[6] and Gaussian smearing is employed to accelerate self-consistent field convergence. The electronic DOS is computed with a 0.1 eV energy grid step. As shown in **Fig. D.1**, the spin-up DOS is below the Fermi level E_F, with the d-band electrons being occupied, while the spin-down DOS cuts through E_F. These results are consistent with previous computational studies on hcp Co.[7,8]

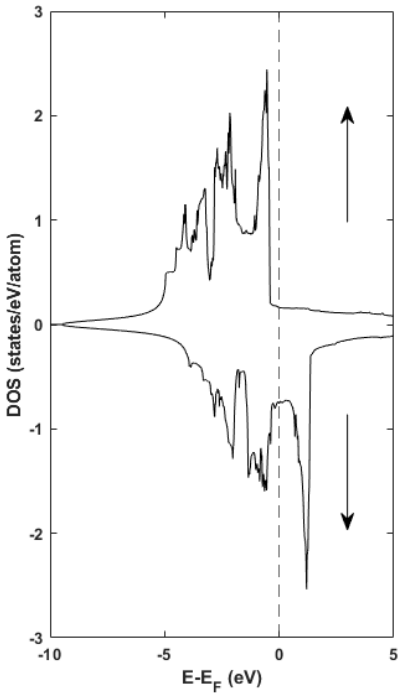

Figure D.1. Spin-polarized electronic DOS of hcp Co.

D.2 Chemical Potential Calculations

Given that the total number of valence electrons N is conserved at any electronic temperature T_e, the chemical potential $\mu(T_e)$ is determined by integrating the product of the Fermi-Dirac distribution function, $f(E, \mu(T_e), T_e) = \{\exp[(E - \mu(T_e))/(k_B T_e)] + 1\}^{-1}$ with Boltzmann constant k_B, and the total electronic DOS of Co, $g(E)$, over all energies:[9,10]

$$N = \int_{-\infty}^{\infty} f(E, E_F, T_e = 0\ \mathrm{K}) g(E) dE = \int_{-\infty}^{\infty} f(E, \mu(T_e), T_e) g(E) dE\,. \qquad (\mathrm{D.1})$$

Co has $3d^7\,4s^2$ valence electrons and exhibits a high electronic DOS near the Fermi level, as illustrated in **Fig. D.1**. This high DOS allows the excitation of *d*-band electrons at the energy levels around the Fermi energy, which results in an increase in the chemical potential as T_e increases, as shown in **Fig. D.2**.

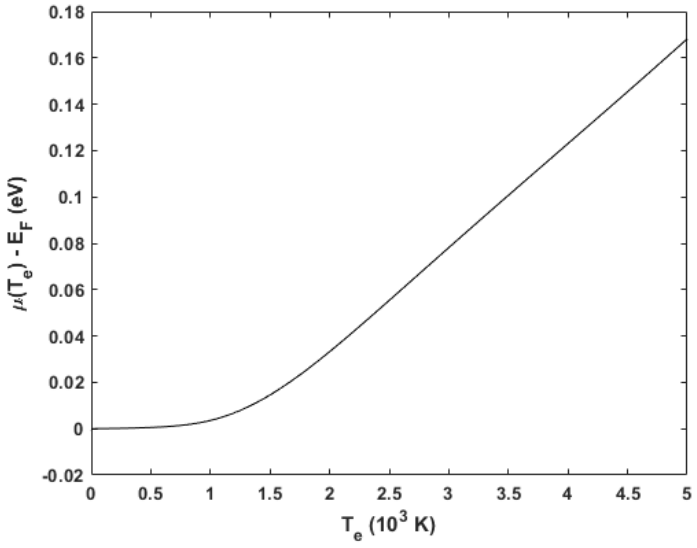

Figure D.2. Chemical potential of Co as a function of the electronic temperature.

D.3 Complex Refractive Index at Varying T_e

Calculations of the complex refractive indices near the Co $M_{2,3}$ edge at varying T_e are performed using the Obtaining Core Excitations from the *Ab initio* electronic structure and the NIST Bethe-Salpeter equation (BSE) solver (OCEAN) version 3.0.3.[11,12] The code first calculates the ground-state electronic structure of Co within plane-wave DFT framework using Quantum ESPRESSO and subsequently computes the complex dielectric function within the BSE approach to account for excitonic effects. For consistency, the same pseudopotential, kinetic energy cutoff, and lattice constants are used in both the DFT and BSE calculations. The MP *k*-point grids employed are 10 × 10 × 10 for the ground state, 16 × 16 × 16 for the final state, and 4 × 4 × 4 for screening calculations. The number of bands for the final-state and screening wavefunctions is set to 100, and a scaling factor of 0.8 is used for the Slater integrals, which is typical for 3*d* transition metals.[13] The electron-hole occupation number differences in the BSE Hamiltonian are determined by the Fermi-Dirac distribution function, with chemical potentials dependent on T_e. The resulting dielectric functions are broadened using a convolution of a Lorentzian function with a FWHM of 0.3 eV. Finally, the complex dielectric function $\epsilon = \epsilon_1 + \mathrm{i}\epsilon_2$ is converted into the complex

refractive index $\tilde{n} = 1 - \delta + i\beta$ by using $1 - \delta = \left\{\left[(\epsilon_1^2 + \epsilon_2^2)^{1/2} + \epsilon_1\right]/2\right\}^{1/2}$ and $\beta = \left\{\left[(\epsilon_1^2 + \epsilon_2^2)^{1/2} - \epsilon_1\right]/2\right\}^{1/2}$. **Figure D.3** illustrates the experimental and calculated complex refractive indices of Co. While the calculations do not as accurately reproduce the experimental complex refractive index, the spectral differences due to photoexcitation is accurately reproduced as proven in previous studies.[14,15] **Figure D.4** demonstrates that the differences in δ and β resulting from a 100 K increase in T_e are most pronounced near the Co $M_{2,3}$ edge, where they contribute to the most intense signal in the self-diffraction spectrum.

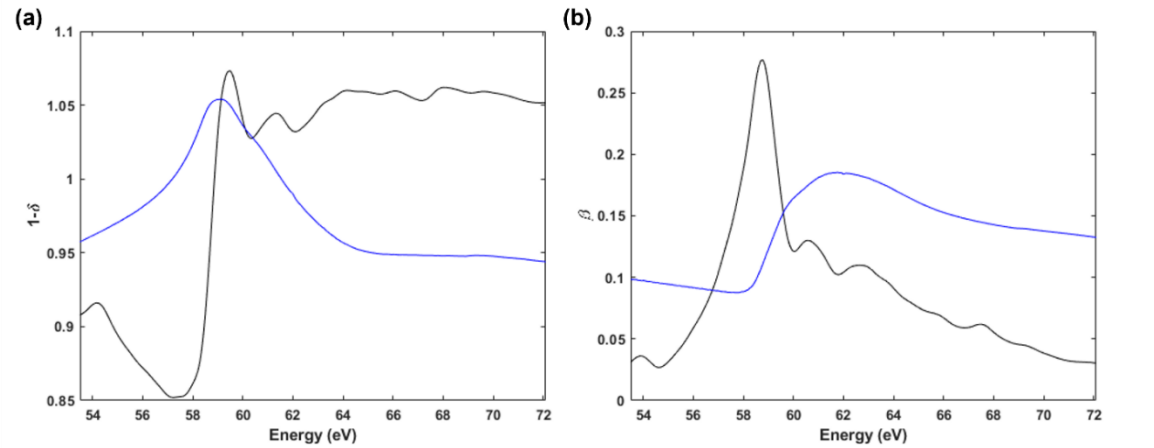

Figure D.3. Comparison of experimental and calculated complex refractive index of Co. (a) Real and **(b)** imaginary parts as obtained from Ref. 16 (blue) and from calculations (black).

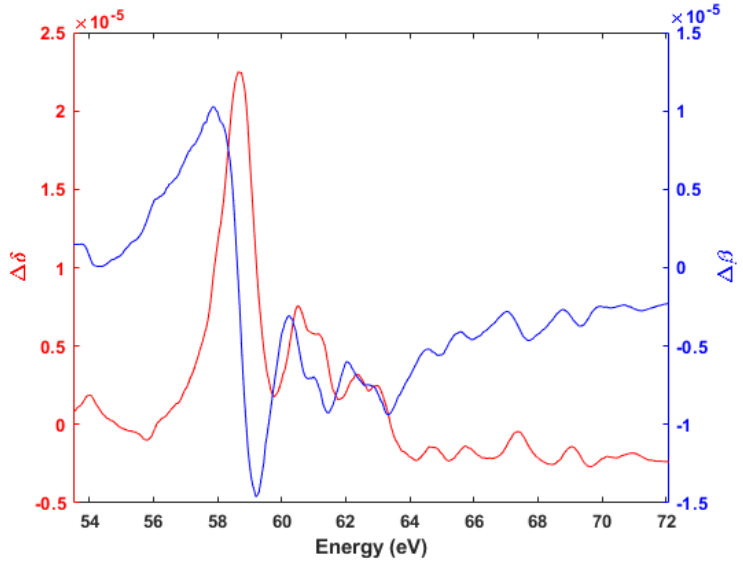

Figure D.4. Δδ (red) and Δβ (blue) at an electronic temperature rise of 100 K from 300 K to 400 K.

D.4 References

(1) Giannozzi, P.; Andreussi, O.; Brumme, T.; Bunau, O.; Nardelli, M. B.; Calandra, M.; Car, R.; Cavazzoni, C.; Ceresoli, D.; Cococcioni, M.; Colonna, N.; Carnimeo, I.; Corso, A. D.; Gironcoli, S. de; Delugas, P.; DiStasio, R. A.; Ferretti, A.; Floris, A.; Fratesi, G.; Fugallo, G.; Gebauer, R.; Gerstmann, U.; Giustino, F.; Gorni, T.; Jia, J.; Kawamura, M.; Ko, H.-Y.; Kokalj, A.; Küçükbenli, E.; Lazzeri, M.; Marsili, M.; Marzari, N.; Mauri, F.; Nguyen, N. L.; Nguyen, H.-V.; Otero-de-la-Roza, A.; Paulatto, L.; Poncé, S.; Rocca, D.; Sabatini, R.; Santra, B.; Schlipf, M.; Seitsonen, A. P.; Smogunov, A.; Timrov, I.; Thonhauser, T.; Umari, P.; Vast, N.; Wu, X.; Baroni, S. Advanced Capabilities for Materials Modelling with Quantum ESPRESSO. *J. Phys.: Condens. Matter* **2017**, *29* (46), 465901.

(2) Giannozzi, P.; Baroni, S.; Bonini, N.; Calandra, M.; Car, R.; Cavazzoni, C.; Ceresoli, D.; Chiarotti, G. L.; Cococcioni, M.; Dabo, I.; Corso, A. D.; Gironcoli, S. de; Fabris, S.; Fratesi, G.; Gebauer, R.; Gerstmann, U.; Gougoussis, C.; Kokalj, A.; Lazzeri, M.;

Martin-Samos, L.; Marzari, N.; Mauri, F.; Mazzarello, R.; Paolini, S.; Pasquarello, A.; Paulatto, L.; Sbraccia, C.; Scandolo, S.; Sclauzero, G.; Seitsonen, A. P.; Smogunov, A.; Umari, P.; Wentzcovitch, R. M. QUANTUM ESPRESSO: A Modular and Open-Source Software Project for Quantum Simulations of Materials. *J. Phys.: Condens. Matter* **2009**, *21* (39), 395502.

(3) Hofer, L. J. E.; Peebles, W. C. Preparation and X-ray Diffraction Studies of a New Cobalt Carbide1. *J. Am. Chem. Soc.* **1947**, *69* (4), 893–899.

(4) Troullier, N.; Martins, J. L. Efficient Pseudopotentials for Plane-Wave Calculations. *Phys. Rev. B* **1991**, *43* (3), 1993–2006.

(5) Perdew, J. P.; Burke, K.; Ernzerhof, M. Generalized Gradient Approximation Made Simple. *Phys. Rev. Lett.* **1996**, *77* (18), 3865–3868.

(6) Monkhorst, H. J.; Pack, J. D. Special Points for Brillouin-Zone Integrations. *Phys. Rev. B* **1976**, *13* (12), 5188–5192.

(7) Matar, S. F.; Houari, A.; Belkhir, M. A. *Ab Initio* Studies of Magnetic Properties of Cobalt and Tetracobalt Nitride Co_4N. *Phys. Rev. B* **2007**, *75* (24), 245109.

(8) Rueff, J. P.; Galéra, R. M.; Giorgetti, Ch.; Dartyge, E.; Brouder, Ch.; Alouani, M. Rare-Earth Contributions to the X-ray Magnetic Circular Dichroism at the Co K Edge in Rare-Earth--Cobalt Compounds Investigated by Multiple-Scattering Calculations. *Phys. Rev. B* **1998**, *58* (18), 12271–12281.

(9) Ashcroft, N.W.; Mermin, N.D. *Solid State Physics*; Holt, Rinehart & Winston: 1976.

(10) Lin, Z.; Zhigilei, L. V.; Celli, V. Electron-Phonon Coupling and Electron Heat Capacity of Metals under Conditions of Strong Electron-Phonon Nonequilibrium. *Phys. Rev. B* **2008**, *77* (7), 075133.

(11) Vinson, J. Advances in the OCEAN-3 Spectroscopy Package. *Phys. Chem. Chem. Phys.* **2022**, *24* (21), 12787–12803.

(12) Vinson, J.; Rehr, J. J.; Kas, J. J.; Shirley, E. L. Bethe-Salpeter Equation Calculations of Core Excitation Spectra. *Phys. Rev. B* **2011**, *83* (11), 115106.

(13) Groot, F. de; Kotani, A. *Core Level Spectroscopy of Solids*; Advances in condensed matter science; CRC Press: Boca Raton, 2008.

(14) Klein, I. M.; Krotz, A.; Lee, W.; Michelsen, J. M.; Cushing, S. K. *Ab Initio* Calculations of XUV Ground and Excited States for First-Row Transition Metal Oxides. *J. Phys. Chem. C* **2023**, *127* (2), 1077–1086.

(15) Liu, H.; Michelsen, J. M.; Mendes, J. L.; Klein, I. M.; Bauers, S. R.; Evans, J. M.; Zakutayev, A.; Cushing, S. K. Measuring Photoexcited Electron and Hole Dynamics in ZnTe and Modeling Excited State Core-Valence Effects in Transient Extreme Ultraviolet Reflection Spectroscopy. *J. Phys. Chem. Lett.* **2023**, *14* (8), 2106–2111.

(16) Saadeh, Q.; Naujok, P.; Thakare, D.; Wu, M.; Philipsen, V.; Scholze, F.; Buchholz, C.; Salami, Z.; Abdulhadi, Y.; García, D. O.; Mentzel, H.; Babuschkin, A.; Laubis, C.; Soltwisch, V. On the Optical Constants of Cobalt in the M-Absorption Edge Region. *Optik* **2023**, *273*, 170455.